THE INFLUENCE OF PARTICLE SIZE AND CRYSTALLINE LEVEL ON THE COMBUSTION CHARACTERISTICS OF PARTICULATED SOLIDS

A Dissertation

by

DIANA YAZMIN CASTELLANOS DUARTE

Submitted to the Office of Graduate Studies of
Texas A&M University
in partial fulfillment of the requirements for the degree of

DOCTOR OF PHILOSOPHY

Chair of Committee,	M. Sam Mannan
Committee Members,	Zhengdong Cheng
	Miladin Radovic
	Eric L. Petersen
Intercollegiate Faculty Chair,	Ibrahim Karaman

August 2013

Major Subject: Materials Science and Engineering

ABSTRACT

Over the past years, catastrophic dust explosion incidents have caused numerous injuries, fatalities and economical losses. Dust explosions are rapid exothermic reactions that take place when a combustible dust is mixed with air in the presence of an ignition source within a confined space. A variety of strategies are currently available to prevent dust explosion accidents. However, the recurrence of these tragic events confirms flaws in process safety for dust handling industries. This dissertation reports advances in different approaches that can be followed to prevent and mitigate dust explosions. For this research, a 36 L dust explosion vessel was designed, assembled and automated to perform controlled dust explosion experiments.

First, we explored the effect of size polydispersity on the evolution of aluminum dust explosions. By modifying systematically the span of the particle size distribution we demonstrated the dramatic effect of polydispersity on the initiation and propagation of aluminum dust explosions. A semi-empirical combustion model was used to quantify the laminar burning velocity at varying particle size. Moreover, correlations between ignition sensitivity and rate of pressure rise with polydispersity were developed. Second, we analyzed the effect of particle size and crystalline levels in the decomposition reactions of explosion inhibitor agents (*i.e.,* phosphates). We fractionated ammonium phosphate- monobasic ($NH_4H_2PO_4$) and dibasic ($(NH_4)_2HPO_4$) at different size ranges, and synthesized zirconium phosphate ($Zr(HPO_4)_2 \cdot H_2O$) at varying size and crystalline levels. Particle size was found to be crucial to improve the

rate of heat absorption of each inhibitor. A simplified model was developed to identify factors dominating the efficiency of dust explosion inhibitors. Finally, we conducted computational fluid dynamic (CFD) simulations to predict overpressures in dust explosions vented through ducts in large scale scenarios. We particularly focused on the adverse effects caused by flow restrictions in vent ducts. Critical parameters, including ignition position, geometric configuration of the vent duct, and obstructions of outflow such as bends and panels were investigated. Comparison between simulation and experimental results elucidated potential improvements in available guidelines.

The theoretical analyses complemented the experimental work to provide a better understanding of the effects of particle size on the evolution of dust explosions. Furthermore, the validation of advanced simulation tools is considered crucial to overcome current limitations in predicting dust explosions in large scale scenarios.

To

God

My parents Emma and Bibiano

My siblings Ana, Oscar and Yamile

My love and best friend Andres

ACKNOWLEDGEMENTS

I would like to express my sincere gratitude to Dr. Mannan for all his assistance and support through my PhD. I am highly thankful for the variety of experiences and challenges that helped me shape into a better scientist. I would like to thank to my committee members, Dr. Zhengdong Cheng, Miladin Radovic, and Dr. Eric L. Petersen, for their guidance throughout the course of this research. Thanks to Dr. Mashuga and Dr. Carreto for their exceptional help that contributed to the success of this research. Special thanks also go to members of the Mary Kay O'Connor Process Safety Centers, especially to Dr. Ha, Valerie, Tricia and Donna; also to Randy and Jason from the Mechanical and physics workshop at Texas A&M University, for their professional assistance and collaboration.

I want to thank to Mr. Skjold, Dr. Pasman, Dr. Eckhoff, Dr. Tamanini and Dr. Rangwala for sharing their knowledge and experience. Their advices were really valuable for this research. I also would like to thank to Dr. Trottier for being willing to participate in this research with the particle size characterization.

I want to extend my gratitude to the companies that contributed with this research, including Dow Chemical Company for donating the 36 L vessel used in this work, to Gexcon S.A. for the assistance on the CFD simulations, to BASF and HYY Aluminum Industry Co. Ltd for donating samples for this investigation.

Finally, special thanks to my mom, my father, my brother and sisters for their encouragement and support; and thank to Andres for his special support and love.

TABLE OF CONTENTS

Page

LIST OF FIGURES

Page

LIST OF TABLES

Page

CHAPTER I

INTRODUCTION

Dust explosions represent a serious industrial problem. They can occur if dust particles are well dispersed in air within a confined space in the presence of an ignition source [1]. One of the first reported dust explosion accidents took place in a flour-warehouse in Turin, Italy in 1785 [1]. In this accident, a dust cloud created while the flour was conveyed between two rooms was ignited by a lamp hanging on the wall. The investigation concluded that besides the turbulence generated, the extremely dryness of the flour was one of the main contributing factors of the accident [1]. In the following decades, there has been a progressive increase of incidents reporting and investigation disclosed common materials, equipment and scenarios leading to these undesired events. In the past 25 years, more than 200 explosions in the United States caused numerous fatalities and economic losses [2]. Materials such as metals, food and plastics are more frequently involved in these accidents [2]; operation units that handle powders having reduced size under highly turbulence levels, such as elevators and mills are more susceptible to dust explosions [1, 3]. Figure 1 shows examples of the consequences that can result from a dust explosion and the typical materials involved [2]. Despite the enormous research efforts to develop strategies to reduce dust explosion risks, this type of event continues to occur in the present time. Hence, a better understanding of the parameters affecting the evolution of a dust explosion is crucial to accurately predict, prevent and mitigate the consequences of this type of accident.

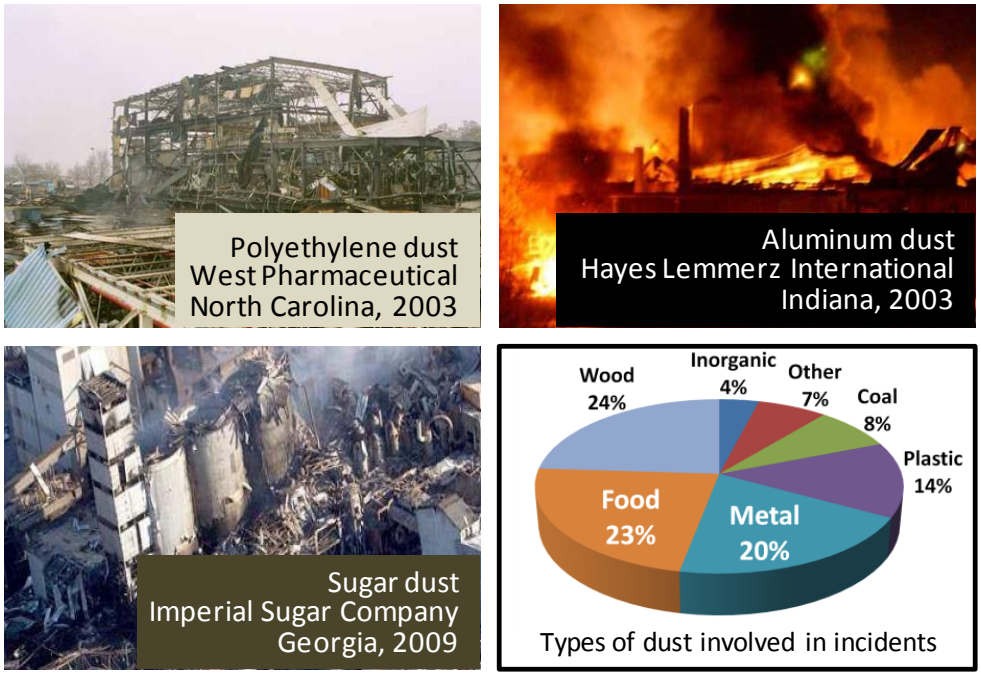

Figure 1. Catastrophic dust explosion accidents and types of dust involved in accidents in the past 25 years. Adapted from [2].

An inherently safer alternative to prevent dust explosions includes modifications of the dust particle size [4]. As particle size increases, the dust surface area available for the combustion process decreases [4-6]. However, particle size is most likely selected based on product specifications. Particle size influences many properties and industrial applications of particulate solids. For instance, the flowability [7], compactibility [8], and dissolubility rate [9-11] in pharmaceutical products, optical properties in metallic pigments [12], the intensity of scattered light in cosmetic products [13], the agglomeration [14], the flowability and reactivity in metal propellants [6], and the

cohesiveness of fine food products [15] are all effected by particle size. However, particle size also affects dust explosiveness.

Typical dust parameters used to identify the severity of a dust explosion are the maximum explosion pressure (P_{max}), the maximum pressure rise $(dP/dt)_{max}$, and the deflagration index (K_{St}). The last one corresponds to the pressure rise multiplied by the vessel volume ($K_{St} = (dP/dt)_{max}V^{1/3}$) [16, 17]. These parameters are used to extrapolate the results from the lab to large scale equipment [17], and they are commonly reported with the respective average dust particle diameter [18]. Theoretical models aiming to predict the dust explosibility are also correlated with an average particle size [5, 18, 19]. Sophisticated computational methods, such as the dust explosion simulator code (DESC), have been able to reproduce experimental results of dust explosions [20]. Nevertheless, DESC still relies on semi-empirical models that require the measurement of P_{max} and K_{St} when particle size is changed [20, 21]. Thus, dust particle size is recurrently used to categorize explosion hazards [5]. Furthermore, powders can be found in a great variety of shapes and polydispersity levels in their particle size distribution (PSD), which may not be fully described by their average particle diameter [22, 23]. The PSD polydispersity can affect the K_{St} characterization [24], and significant uncertainties are found when K_{St} results are extrapolated for a dust with a different PSD. This encourages further research to identify the effect of size polydisperse on the explosion characteristics of combustible dusts.

The consequences of a dust explosion can be lowered by combining inhibitors with the combustible dust to delay the combustion process and reduce the pressure wave

propagation. A variety of materials including, carbonates [25], phosphates [25-30], metal oxides [31], and salts [32] are used for this type of application. However, complete explosion suppression typically requires elevated additive concentration which represents unacceptable product contamination [25-29]. Hence, more research efforts should be devoted to improving the efficiency or exploring alternative materials for inhibition of dust explosions. Herein, we introduce the use of zirconium phosphate ($Zr(HPO_4)_2 \cdot H_2O$) or α-ZrP and diammonium phosphate (DAP), as potential inhibitors to prevent dust explosion accidents. Previous studies have incorporated these materials into flammable substrates to reduce their burning rate [33-37]. α-ZrP increases thermal stability which reduces substrate volatilization [33-35] and DAP absorbs energy by endothermic decomposition [38]. We focused on the influence of inhibitor particle size, chemical composition and crystalline level on the efficiency of these materials as explosion inhibitors. The quantitative comparison of the inhibitors performance was evaluated using thermo gravimetric analysis (TGA), differential scanning calorimeter (DSC) and a 36 L dust explosion equipment.

In many situations, inherent safety design and dust explosion prevention methods must be complemented with mitigation methods to achieve acceptable safety levels. Explosion venting is a mitigation method widely used to reduce the consequences of a dust explosion. This method consists of the release of destructive overpressures through a vent opening once the explosion takes place [1]. Explosion products can be conveyed to safer locations using vent ducts. The effect of ducts on vented dust explosions has motivated several experimental and theoretical studies [39-42]. Some empirical

correlations have been adopted by standards for the design of explosion protection systems [42-44]. However, the experimental results used as foundation of these correlations are not easily extrapolated to the complex geometries commonly found in the industry [45, 46]. Hence, the development and validation of more advanced simulation tools, not limited to simple isolated scenarios, is crucial to accurately extrapolate experimental results and improve the design of vent duct systems. Toward this end we extrapolated laboratory dust explosion results to large scale scenarios using the computational fluid dynamics (CFD) code DESC. A series of dust explosion experiments conducted in an 18.5 m^3 vessel were simulated. Using a wide range of scenarios, we were able to identify crucial design parameters affecting the venting process. Comparison between simulated and experimental results was also useful to identify potential improvements in available standards and guidelines.

1.1. Objectives, significance of the work and methodology

The general objective of this research is to gain understanding of parameters affecting the ignition and propagation of dust explosions in order to develop more efficient methods to prevent and mitigate explosions accidents. Several objectives were formulated:

1) The setup, automatization and calibration of a 36 L vessel. The development of an experimental platform to conduct controlled dust explosions is essential to quantify the consequences of a dust explosion in terms of P_{max}, $(dP/dt)_{max}$, K_{St} values. This work is documented in **Chapter II**.

2) Investigation of the effects of the size polydispersity on the explosion behavior of aluminum dust. This investigation elucidates more suitable ways to describe the particle size distribution rather than the median mean diameters (D_{50}), which is currently used (**Chapter III**). The results are of fundamental importance to predict the real potential explosion hazard, when samples of different polydispersity are handled.

3) Study the influence particle size and crystalline level on the efficiency of dust explosion inhibitors (**Chapter IV**). These results elucidate novel routes for the design and synthesis of more efficient inhibitor materials for dust explosion prevention.

4) Extrapolation of laboratory results to large-scale scenarios using computational fluid dynamics (CFD) simulations. The results are useful to identify critical parameters affecting the dust explosion venting through ducts, including ignition position, geometric configuration of the vent duct and additional obstructions of outflow (bends and panels) (**Chapter V**). This approach reduces the need of large scale experiments, which represents substantial cost reductions on the design of explosion protection systems in complex geometries (industrial scenarios).

The general approach for the study of the influence of particle size and crystalline level on the combustion characteristics of particulate solids to develop more efficient prevention and mitigation methods is presented in Figure 2.

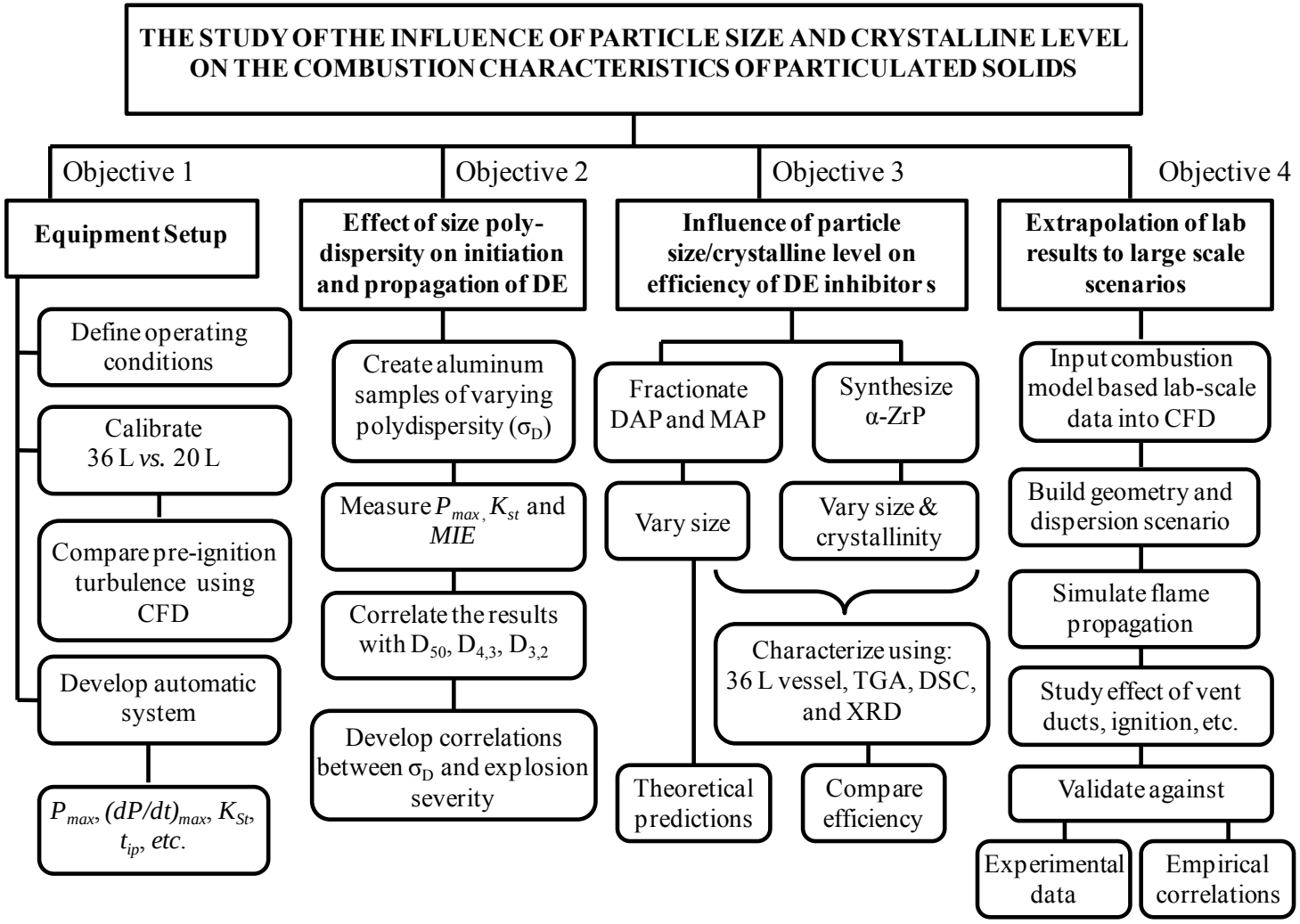

Figure 2. Methodology for the study key parameters affecting dust explosion prevention and mitigation methods.

CHAPTER II

BACKGROUND

2.1. Synopsis

Dust explosion research can be divided into four main areas: dust cloud formation, ignition, propagation and the final wave generation during a dust explosion [47]. The initiation and propagation of dust explosions are of particular interest in this research. This chapter describes the requirements to obtain a dust explosion and main parameters affecting the evolution of the propagating dust explosion. It details the experimental method utilized to quantify the severity of a dust explosion and summarizes common explosion indexes used to characterize the hazards of a combustible dust. Finally, the chapter provides a review of available strategies to prevent and mitigate dust explosions. The more fundamental literature review is extended in each of the following chapters depending on the specific topic discussed.

2.2. Dust explosion

In a combustion reaction, fuel and an oxidizer react to produce oxides and heat [1]. An external energy source locally increases the temperature of the reactants to initiate the combustion reaction. The flame propagation starts once the heat generated becomes larger than the heat of dissipated in a certain volume of combustible [1]. The flame propagates from the ignition point toward the unburned mixture until any of the reactants is consumed [1].

A dust explosion is a combustion reaction characterized by a sudden release of heat that produces a pressure wave during the hot gases expansion [48]. A dust explosion requires five elements to take place: 1) *Fuel*: particles less than 500 μm that are not stable oxides, such as natural and synthetic organic materials, metals and coal [1]. 2) *Oxidizer*: oxygen usually provided by air. 3) *Ignition source*: provides the energy required to start the combustion reaction. 4) *Turbulence*: required to generate the particles suspension. 5) *Confinement*: it enhances the pressure built up during the flame propagation process. These requirements are usually referred to as the explosion "pentagon" as shown in Figure 3 [49].

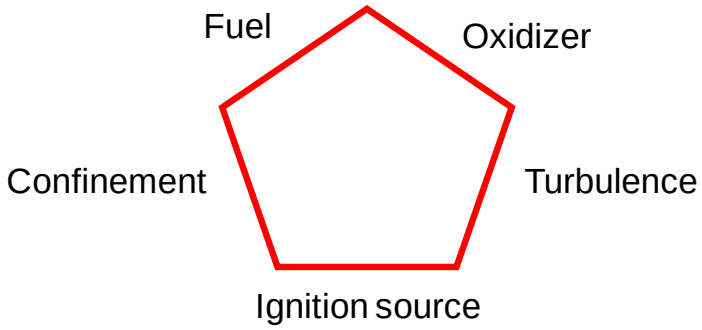

Figure 3. Dust explosion requirements. Adapted from [49]

Depending on the physical state of the combustible dust and the reaction products, different reaction mechanisms can be obtained [50]:

- Heterogeneous combustion, reaction on the solid surface with gaseous products. This mechanism is can be observed in carbonaceous materials ($C_{(s)} + O_{2(g)} \rightarrow$

$CO_{2(g)}$). The reaction is typically governed by the powder surface area [50]. However, depending on the efficiency of the combustion process, nonvolatile products (char) can be produced. In the case of combustion reaction carried out on the solid surface with solid products, solid layer of products (char) limits the oxygen diffusion to the combustible dust [50] and reduces the surface burning rate [51].

- Homogenous combustion, reaction in gas phase with gaseous products [52]. This mechanism is observed in organic powders such as food products [52] and polymers [19, 53, 54], where the combustible dust undergoes pyrolysis, devolatization, and then combustion. The competition between vaporization and combustion rates determines if the combustion reaction is surface area or chemical kinetics controlled [50]. In reality, a combination of these mechanisms is typically obtained, but the latter is more commonly studied in modeling and simulations due to its simplicity.

2.3. Dust explosion testing

Explosion testing in constant volume equipment is useful to consistently combine the five elements required to obtain a dust explosion (Figure 3) [16-18]. Research with this type of equipment has been undertaken with three main purposes: 1) to measure parameters to quantify the risk of having a dust explosion, 2) to estimate the burning velocity, and 3) to study the factors affecting the evolution of a dust explosion. The first point is covered in this section and the background related to the burning velocity and the factors affecting the evolution of the explosion is expanded in section 2.2 and 2.4, respectively.

2.3.1. Quantify the severity of a dust explosion

The explosion severity is quantified by measuring the maximum pressure (P_{max}) and the maximum rate of pressure rise ($(dP/dt)_{max}$), during dust explosion tests [55]. Given that $(dP/dt)_{max}$ depends on the vessel volume, this parameter is multiplied by the cubic root of the volume to obtain the deflagration index ($K_{St} = (dP/dt)_{max} \cdot V^{1/3}$) [16, 17]. K_{St} values can be scaled-up from laboratory-scale tests to plant size equipment [56]. The 1 m^3 and the 20 L vessels are widely used for this type of testing. Figure 4 shows a schematic of the standard 20 L vessel.

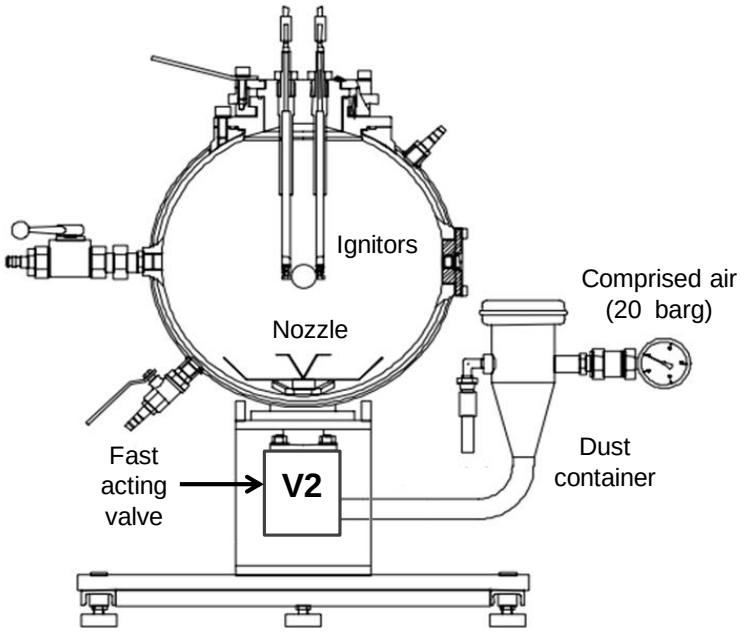

Figure 4. Schematic of standard 20 L vessel [57]

In a typical experiment with this equipment, the vessel is hermetically closed and evacuated to 0.6 bar(a), and the dust sample is loaded into the dust container which is pressurized with air. Then, a fast acting valve (V2) is open, to release the dust-air mixture into the vessel through a rebound nozzle. The dispersion process causes an increase in the vessel pressure to 1 bar absolute. After a specific delay time, two 5 kJ igniters are activated and the resulting explosion pressure history is recorded. Figure 5a. shows the pressure (barg) profile as a function of time (ms) during a dust explosion test, where the maximum pressure P_{ex} and the maximum slope or rate of pressure rise $(dP/dt)_{ex}$ are obtained for a specific dust concentration (C). τ represents the time span to reach the maximum rate of pressure rise. This parameter gives insights of the velocity of the flame propagation of the tested samples.

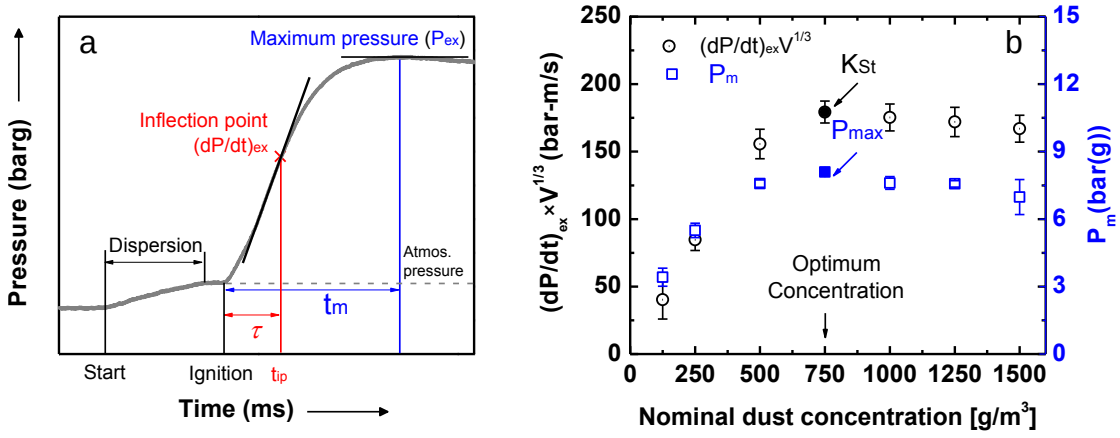

Figure 5. Typical experimental dust explosion results. (a) Pressure profile during a dust explosion test. (b) Explosive characteristics *vs.* dust concentration

P_{ex} is corrected into P_m to account the cooling effects of the vessel walls and the pressure effects caused by the igniters, using the following correlations [58]:

$$\text{for } P_{ex} > 5.5,\ P_m \text{ (bar)} = 0.775\ P_{ex}\ 1.15 \quad \textbf{(1)}$$

$$\text{for } P_{ex} < 5.5,\ P_m \text{ (bar)} = 5.5\ ((P_{ex} - P_{CI})/(5.5 - P_{CI}))1.15 \quad \textbf{(2)}$$

where, P_m corresponds to the explosion pressure, and P_{CI} corresponds to the pressure increase due to the igniters. Additional tests are then conducted by systematically increasing the dust concentration between 250 and 3000 g/m^3, until P_{ex} and $(dP/dt)_{ex}$ results indicate that a maximum value has been reached [58]. $(dP/dt)_{ex}$ is multiplied by the cube root of the vessel volume to obtain $(dP/dt)_{ex}V^{1/3}$. As shown in Figure 5b, P_{max} and K_{St} are the maximum values of P_m and $(dP/dt)_{ex}V^{1/3}$ at varying dust concentrations. The optimum concentration corresponds to the concentration where P_{max} and K_{St} values are found [58]. These parameters are reported along with the median diameter (D_{50}). The deflagration index, K_{St} is used to classify the dust explosion severity, as shown in Table 1.

Table 1. Dust explosibility based on K_{St} values

Definition	Range		Category
$K_{St} = \left(\frac{\mathrm{dP}}{\mathrm{dt}}\right)_{\max} \times \mathrm{V}^{1/3}$	If $K_{St} = 0$	→	Group St0 : non-explosive
	If $0 < K_{St} \leq 200$	→	Group St1 : weak
	If $200 < K_{St} \leq 300$	→	Group St2 : strong
	If $K_{St} > 300$	→	Group St3 : very strong

2.3.2. Explosion indexes

In attempting to reduce dust explosion incidents, a variety of explosion indexes are used to identify the risk associated with dust handling in the process industries [16-18]. The dust explosion risk is a function of the severity of the explosion and its likelihood of occurrence [49]. Table 2 summarizes common explosion indexes used to characterize the combustible dust, the standard used for the measurement, a brief description and the risk component at which it is related to and typical applications.

Qualitative trends of these explosion indexes at varying dust characteristics or operation conditions are found in the literature. However, a quantitative prediction of the explosion hazards at varying industrial environments or materials properties is difficult due to the lack of theoretical models to predict the evolution of the propagating dust explosion and experimental determination is usually required. Therefore, a fundamental knowledge of the parameters affecting the course of the explosion is crucial to develop more effective measures to dust explosions and guarantee a safer operation.

Table 2. Explosion indexes, determination and application [49]

Explosion index	ASTM Standard	Description (risk component)	Application
$\boldsymbol{P_{max}}$ (bar(g)) Maximum explosion pressure	ASTM E 1226 [57]	Maximum explosion pressure measured in a constant volume vessel. (Severity)	Design of containment, venting and suppression systems.
$\boldsymbol{(dp/dt)_{max}}$ (bar/s) Maximum rate of pressure rise	ASTM E 1226 [57]	Related to the velocity of the explosion propagation. (Severity)	As per P_{max}
$\boldsymbol{K_{St}}$ (bar-m/s) Dust deflagration index	ASTM E 1226 [57]	Maximum rate of pressure rise multiplied by the cubic root of the vessel volume. (Severity)	As per P_{max}
MIE (mJ) Minimum Ignition energy	ASTM E 2019 [59]	The lowest energy able to initiate the explosion propagation. (Likelihood).	Identify degree of protection required to avoid ignition sources.
MEC (g/m^3) Minimum explosive concentration	ASTM E 1515 [60]	Measures the lowest dust concentration able to maintain a dust explosion. (Likelihood).	Control of dust accumulations
LOC (volume %) Limiting oxygen concentration	ASTM WK1680	Minimum oxygen concentration for the flame propagation. (Likelihood)	Identify degree of inerting
MIT (°C) Minimum ignition temperature of a dust cloud	ASTM E1491-06 [61]	Lowest temperature leading the explosion propagation. (Likelihood).	Control process temperature
LIT (°C) Minimum ignition temperature of a dust layer	ASTM E2021-06 [62]	Lowest temperature that initiate the combustion reaction of a dust layer. (Likelihood).	Control process temperature

2.4. Estimation of burning velocity from closed vessel experiments

The burning velocity (S_u) is the velocity of the flame propagation in relation to the unburned mixture; it is useful to predict the evolution of a dust explosion as a function of time [63, 64]. S_u of a combustible dust can be estimated using pressure traces obtained from dust explosion tests performed in constant volume equipments [65-69]. Bradley [68] and Dahoe *et al.*, [56] reported similar correlations for S_u using the following assumptions: ignition at the center of the vessel and spherical flame propagation; burning velocity independent of the turbulence flow field, pressure and temperature; irreversible combustion reaction; burned and unburned gases with ideal gas behavior and unchanged heat capacities during the explosion [56].

During the explosion, the changes in pressure are proportional to the burnt mass [70]:

$$\frac{p(t)-p_i}{p_f-p_i} = \frac{m_b(t)}{m_{total}} = \frac{m_b(t)}{m_{u,i}} \quad \textbf{(3)}$$

where p_i and p_f correspond to the initial and final pressure; m_b and m_{total} correspond to the burnt and total mass, and $m_{u,i}$ corresponds to the initial mass of unburned materials.

$$\frac{dp}{dt} = \frac{p_f-p_i}{m_{u,i}} \frac{dm_b(t)}{dt} \quad \textbf{(4)}$$

Based on mass conservation: $m_b = -m_u$

Thus,

$$\frac{dp}{dt} = -\frac{(p_f-p_i)}{m_{u,i}} \frac{dm_u(t)}{dt} \quad \textbf{(5)}$$

The change of burn mass as function of time is given by:

$$\frac{dm_u}{dt} = -A_b \rho_u S_u = -4\pi r_b^2 \rho_u S_u \quad \textbf{(6)}$$

where A_u, r_b, S_u and ρ_u correspond to the area of the growing flame, the radius of the flame and the density of the unburned mixture. Then, the change of pressure with time can be expressed in terms of S_u [70]:

$$\frac{dp}{dt} = \frac{(p_f - p_i)}{m_{u,i}} (4\pi r_b^2 \rho_u S_u) \quad \textbf{(7)}$$

Expressing the unburned mixture density (ρ_u) in terms of the pressure, assuming adiabatic compression:

$$\frac{\rho_{u,i}}{\rho_u} = \left(\frac{p_i}{p}\right)^{\frac{1}{\gamma}} \quad \textbf{(8)}$$

The flame radius (r_b) can be expressed in terms of the vessel volume:

$$V_v = V_b + V_u \quad \textbf{(9)}$$

$$V_b = \frac{4}{3}\pi r_b^3 \quad \textbf{(10)}$$

$$V_u = \frac{m_u}{\rho_u} = m_u \rho_{u,i}^{-1} \left(\frac{p_i}{p}\right)^{\frac{1}{\gamma}} = m_u \rho_{u,i}^{-1} \left(\frac{p}{p_i}\right)^{-\frac{1}{\gamma}} = m_u \frac{V_v}{m_{u,i}} \left(\frac{p}{p_i}\right)^{-\frac{1}{\gamma}} \quad \textbf{(11)}$$

The ratio $m_u/m_{u,i}$ is given by [70]:

$$\frac{m_u}{m_{u,i}} = \frac{p_f - p}{p_f - p_i} \quad \textbf{(12)}$$

Thus,

$$V_u = V_v \left(\frac{p_f - p}{p_f - p_i}\right) \left(\frac{p}{p_i}\right)^{-\frac{1}{\gamma}} \quad \textbf{(13)}$$

where γ is the specific heat ratio. Thus:

$$V_v = V_b + V_u = \frac{4}{3}\pi r_b^3 + V_v \left(\frac{p_f - p}{p_f - p_i}\right) \left(\frac{p}{p_i}\right)^{-\frac{1}{\gamma}} \quad \textbf{(14)}$$

Solving for r_b [70]:

$$r_b = \left\{\frac{3V_v}{4\pi}\left[1 - \left(\frac{p_f - p}{p_f - p_i}\right)\left(\frac{p}{p_i}\right)^{-\frac{1}{\gamma}}\right]\right\}^{\frac{1}{3}} \quad \textbf{(15)}$$

Replacing r_b (from 15) and ρ_u (from 8) into (7) [70]:

$$\frac{dp}{dt} = 4\pi(p_f - p_i)\frac{\rho_{u,i}}{m_{u,i}}\left(\frac{p_i}{p}\right)^{\frac{1}{\gamma}}\left\{\frac{3V_v}{4\pi}\left[1 - \left(\frac{p_f - p}{p_f - p_i}\right)\left(\frac{p}{p_i}\right)^{-\frac{1}{\gamma}}\right]\right\}^{\frac{2}{3}} S_u \quad \textbf{(16)}$$

Solving for S_u [56]:

$$S_u = \frac{1}{3(p_f - p_i)}\left(\frac{dp}{dt}\right)\left(\frac{3V_v}{4\pi}\right)^{\frac{1}{3}}\left(\frac{p_i}{p}\right)^{-\frac{1}{\gamma}}\left[1 - \left(\frac{p_f - p}{p_f - p_i}\right)\left(\frac{p}{p_i}\right)^{-\frac{1}{\gamma}}\right]^{-\frac{2}{3}} \quad \textbf{(17)}$$

Therefore, S_u can be determined from experimental data obtained from constant volume equipments. Based on Dahoe *et al.*, [71], the experimental data used for S_u calculations should be extracted at the inflection point of the pressure profile curve. During the dust explosion, the growing flame ball moves upwards due to the density differences between hot products and cold reactants. The pressure rises until the flame ball reaches the top wall, so the inflection point is reached. At this point, the flame area decreases but the dust combustion proceeds at the lower part of the flame ball and the pressure rate decreases with time. Consequently, the model fits better to experimental data until the inflection point [71].

$$S_{u,ip} = \frac{1}{3p_m}\left(\frac{dp}{dt}\right)_{\mathrm{m}}(V_v)^{\frac{1}{3}}\left(\frac{3}{4\pi}\right)^{\frac{1}{3}}\left(1 + \frac{p_{ip}}{1(bar)}\right)^{-\frac{1}{\gamma}}\left[1 - \left(1 - \frac{p_{ip}}{p_m}\right)\left(1 + \frac{p_i}{1(bar)}\right)^{-\frac{1}{\gamma}}\right]^{-\frac{2}{3}} \quad \textbf{(18)}$$

where $S_{u,ip}$ and p_{ip} are the burning velocity and pressure at the inflection point.

2.5. Estimation of laminar burning velocity

The ultimate goal is to correlate S_u with the laminar burning velocity (S_L) because S_L is characteristic of the fuel nature and fuel/oxidant ratio at a given initial pressure and temperature. The laminar burning velocity is defined as the flame front speed that propagates in a quiescent fuel-air mixture [72]. This parameter is essential to model the overpressure produced during an explosion [73]. In gas explosions, S_L can be determined from measurements using Bunsen-type burners and from pressure variations in constant volume equipment [74, 75]. In the case of a combustible dust, S_L can be measured using Bunsen-type burners [76, 77]. However, S_L cannot be directly measured using a constant volume equipment (*e.g.*, dust explosion apparatus) due to the following: (1) it is not possible to generate a complete quiescent dust-air mixture due to the turbulence and strong forces that arose during dust cloud generation [70]; (2) dust concentrations are usually not uniform within the dust cloud [70, 78]; and (3) the flame front is not easy to identify from visual observations [70, 79]. Due to these limitations, different researchers have focused their efforts on developing correlations between S_u and S_L [63, 70-72]. These correlations are typically developed assuming thin flame zones and homogeneous devolatilization of combustible dust; and they are based on the similarities between gas and dust explosions [68]. Garcia [80] compiles a summary of different combustion models used for gas and dust explosions.

Skjold [81] reported a condensed combustion model for turbulent dust clouds from previous empirical correlations. From this model, S_L can be estimated from experimental parameters such as pressure, time, and rate of pressure rise at the inflection

point. These correlations have been effectively used for S_L calculations of coal and corn dust [81]. A summary is of the correlations is reported here and more detailed information is found in [81]. From the reformulation of empirical correlations proposed for gaseous mixtures [63]:

$$\mathrm{S_u/S_L} = 0.875\mathrm{K_k^{-0.392}}(\mathrm{u'_{rms}/S_L}) \quad \textbf{(19)}$$

where K_k is the Karlovitz stretch factor, and u'_{rms} represents the root-mean-square of the velocity fluctuations. Based on similarities between gas and dust explosions [68], this equation has been modified [82], and solved for S_L [81]:

$$S_{L,ip} = 0.0315\left[S_{u,ip}\right]^{1.276}\left[u'_{rms,ip}\right]^{-0.526}\left[l_{I,ip}\right]^{-0.250} \quad \textbf{(20)}$$

where, $S_{L,ip}$ and $S_{u,ip}$ are the laminar and turbulent burning velocity defined at the inflection point, $u'_{rms,ip}$ represents the root-mean-square of the velocity fluctuations at inflection time (t_{ip}), and $l_{I,ip}$ is the integral length scale at the inflection point.

S_u is obtained from equation 18, and the root-mean-square of the velocity fluctuations and turbulence decay following the dispersion process in the 20 L apparatus is given by [81, 83]:

$$u'_{rms,ip} = u'_{rms,0}\left(t_{ip}/t_0\right)^n \quad \textbf{(21)}$$

where, $u'_{rms,0}$ represent the root-mean-square of the velocity fluctuations at the time of onset of dispersion (t_0). With $u'_{rms,0}$ = 3.75 m/s, t_0 = 0.060 s and n = -1.61 [83, 84]. Finally, the integral length scale empirical correlation is given by [85]:

$$l_{I,ip} = l_{I,0}exp\left\{-3.542ln\left(\frac{t_{ip}}{t_0}\right) + 1.321\left[ln\left(\frac{t_{ip}}{t_0}\right)\right]^2\right\} \quad \textbf{(22)}$$

where, $l_{I,0}$ equals to 0.01285 m and corresponds to the integral length scale at dispersion time.

2.6. Effects of turbulence on dust explosion testing

The turbulence describes the random movement of the components of a dust cloud in different directions [86]. In dust explosion testing, two types of turbulence are obtained, the initial turbulence required to generate the dust cloud suspension and the turbulence generated by the explosion itself [86]. The initial turbulence is the primary focus of this section due to its importance for the equipment setup and calibration.

During the dust air injection into the explosion vessel, the initial turbulence is highly anisotropic [87] and it has a strong effect on course of the explosion test [86, 88, 89]. The initial, or pre-ignition turbulence is quantified by the root-mean-square of the velocity fluctuations (u_{rms}) during dust cloud formation [86]. This turbulence is mainly affected by the type of dispersion nozzle [70, 83], the supplied pressure in the reservoir [90, 91] and the ignition delay time [78, 92-94].

The nozzle geometry affects the velocity fluctuations toward specific directions and the turbulence build up period [73, 95]. The standard test method for explosibility (ASTM 1226) recommends the use of a perforated annular nozzle or a rebound nozzle (Figure 6a and b) [57]. The perforated annular nozzle presents a proper chaotic dispersion. However, fibrous samples can block the small openings in the nozzle [95]. The rebound nozzle does not present this problem. However, the vertical component of the mean velocity is larger than the horizontal component in the first 10 ms [95]. Hence,

when using a rebound nozzle, ignition delay times larger than 10 ms are recommended to prevent any displacement of the growing spherical flame.

Skjold [70] measured the turbulence decay during the dispersion process in a 20 L vessel using different types of injection nozzles (Figure 6 b-d). Skjold [70] reported that u_{rms} values were significantly higher in mushroom and pepper nozzles in comparison with the rebound nozzles. Dahoe *et al.,* [50, 65, 83] used the Laser Doppler Anemometry (LDA) [87] technique to correlate u_{rms} values with the ignition delay time for three different nozzle types, including a rebound, an annular and the Dahoe's nozzle [83]. Several other authors have also investigated the turbulent flow field dependency with the ignition delay time inside dust explosion vessels [96, 97]. Pu *et al.,* [96] studied the effect of the turbulence generated during the dispersion process in vessels of different sizes (*i.e.,* 6, 26 and 950 L) [96]. The pre-ignition turbulence has linear relationship with the velocity of the flame propagation. Pu *et al.,* [98] found that burning velocity of aluminum and cornstarch decrease monotonically as u_{rms} decreases. Similarly, experimental results from methane-air and corn-air mixtures showed a proportional decay of K_{St} and u_{rms} values with increased ignition delay time [96]. van de Wel *et al.,* [99], Mercer *et al.,* [95] and Kauffman *et al.,* [100] also reported the strong effects of turbulence on the propagation of dust explosions. In fact, van de Wel *et al.,* [99] attributed the discrepancies in the results between 20 L and 1 m^3 vessels for different types of dust explosions to differences on turbulence levels at the ignition time. Bradley *et al.,* [68] manipulated the dispersion induced turbulence of gas and dust explosions using a fan-stirred explosion vessel, and correlated the burning velocity to the

turbulence levels [68]. Based on Zhen and Leuckel [90, 91], the burning velocity is not only affected by ignition delay time but also by the initial reservoir pressure and dust loading. In general, equipment operation conditions that diminish the pre-ignition turbulence (*e.g.*, long ignition delay times) will ultimately reduce the explosion severity and burning velocity of dust explosions.

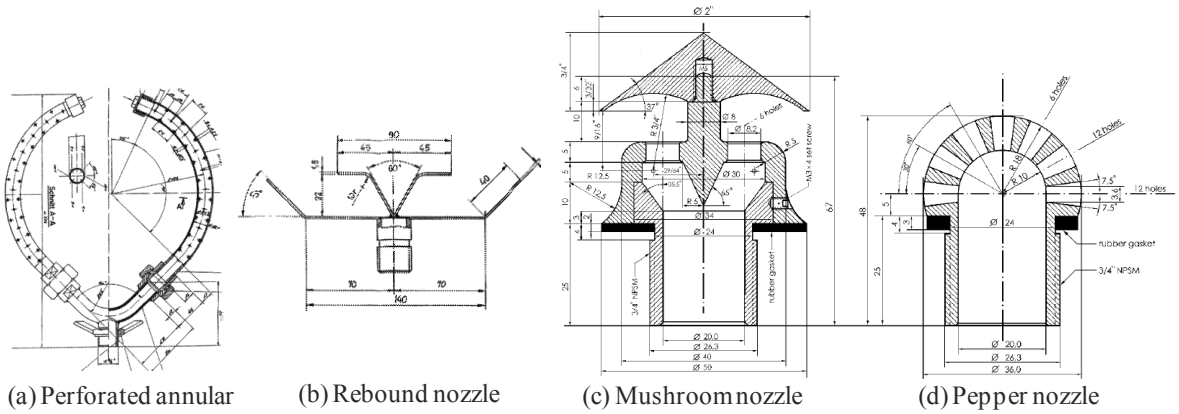

Figure 6. Dispersion nozzles used in dust explosion apparatus [70, 95].

The turbulence caused by the igniter's energy can also affect the course of a dust explosion test [92]. A strong ignition source generates a wave that displaces the dust particles from the center to the outer section of the vessel [101]. As a result of this dust accumulation in the peripheral region, the determination of the minimum explosive concentration (MEC) can be overestimated [101]. Going *et al.,* [102] determined MEC values in the 20 L and 1 m^3 vessels for different dusts using an ignition source of 1, 5, 2.5, 5 and 10 kJ, respectively. The MEC results were significantly lower in the smaller

chamber [102]. The best agreement between MEC values in these two pieces of equipment was found using 2.5 kJ in the 20 L vessel and 10 kJ in the 1 m^3 vessel. This overdriving effect due to the ignition source strength has also been reported by Zhen and Leuckel [92], Hertzberg, *et al.,* [103, 104], Cashdollar, *et al.,* [105, 106], and Proust *et al.,* [107].

2.7. Parameters affecting dust explosion

2.7.1. Chemical composition

The chemical composition affects the thermodynamics and the kinetics of the combustion reaction [1]. The thermodynamics is associated with the amount of heat released during the exothermic combustion reaction that breaks reactants bonds to create new products (typically CO_2 and water). The released energy during the reaction (ΔH), corresponds to the difference between the energy storage in the reactants and products bonds [51]. The kinetics is associated to the rate at which the heat is released, and it depends on the system conditions [51]. In the case of homogeneous combustion reaction (dust volatilization preceding combustion in gas phase), the reaction rate depends on the collisions between reactants molecules which increases with temperature [51]. Based on Parker and Hottel [108, 109], a single spherical particle has an oxidation reaction rate described by the following equation [109]:

$$-\frac{dm}{dt} = \frac{k}{\sqrt{T}}\left[exp\left(-\frac{E_a}{RT}\right)\right] C_g \pi D_p^2 \qquad \textbf{(23)}$$

where m, D_p are the mass and diameter of the particle; k, t and E_a are the reaction rate constant, time and activation energy; and R, T and C_g correspond to the universal gas constant, absolute temperature and oxygen concentration of the system, respectively. E_a

varies with the fuel chemical composition (*e.g.,* E_a values of 60, 26, 17.7 and 14.32 kcal/mol are reported for aluminum [110], cellulose acetate, magnesium [109], and cornstarch [111], respectively). In the case of heterogeneous combustion reaction (combustion on solid surface phase), the flame propagation is governed by the ignition temperature [112], which is also dependent on the chemical composition.

2.7.2. Fuel concentration

Fuel concentration affects P_{max}, $(dP/dt)_{max}$ [70, 113-115] and burning velocity [116-118] of gas and dust–air explosions. The fuel concentration can be expressed in terms of equivalent ratio (ϕ) which is the air-fuel ratio divided by stoichiometric air-fuel ratio. In gas explosions, the maximum values of P_{max} and $(dP/dt)_{max}$ are obtained at the stoichiometric concentration ($\phi = 1$), and both of them decrease as the concentration changes to lean or rich mixtures [70, 115, 119]. This effect is shown in Figure 7. In rich mixtures ($\phi > 1$), some energy released is consumed in heating the excess of reactants, which lowers the system temperature. In lean mixtures ($\phi < 1$), the total amount of energy produced is limited by the oxygen concentration [51]. In dust explosions, the maximum explosion severity is reached at concentrations larger than the stoichiometric concentration. A delayed dust volatilization lowers the effective fuel concentration in the atmosphere at a certain time. Consequently, P_{max} and K_{St} values are usually obtained in fuel rich mixtures ($\phi > 1$). Figure 7 shows the effect of fuel concentration on the explosion severity in gas and dust explosions.

Dust concentration strongly affects the efficiency of heat transference within the cloud. Given that the combustion reaction take place in discrete points, the heat

transference is a function of the inter-particle spacing [112]. At low dust concentrations, large inter-particles spacing restricts the heat diffusion toward the unburned particles whereas at higher dust concentrations, the reduced inter-particle spacing improves the heat transference between particles enhancing the velocity of the flame propagation [112]. This also explains why the maximum explosion severity (P_{max}, K_{St} values) is achieved at $\phi > 1$.

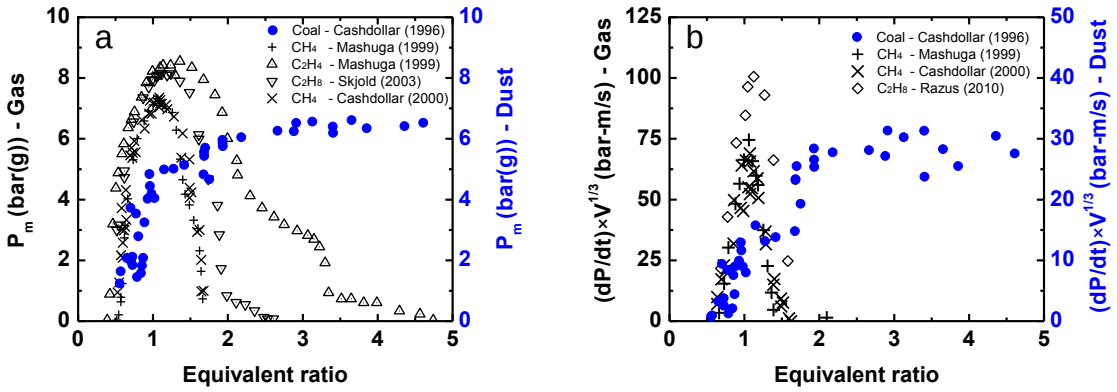

Figure 7. Effect of fuel concentration on explosion severity of gas and dust –air mixtures. (a) P_m and (b) $(dP/dt)_{ex}V^{1/3}$. Data from Cashdollar [24, 119], Mashuga [113], Sjkold [70], Razus [120].

2.7.3. Particle size

Particle size plays a crucial role on the initiation and propagation of dust explosions. Small particles are characterized by a large surface area and a reduced sedimentation velocity that allows them to stay in suspension for a long time [121]. This

favors the heating, devolatilization and combustion reaction rate [19]. Despite several efforts to correlate particle size and explosion severity of combustible dusts (*e.g.,* wood [121], polymers [19], coal [122], iron sulphide [123], aluminum [67, 124], and magnesium [125]), a unified theory to predict explosion hazards as a function of particle size is not yet available. The general trend is an increase of explosion severity as particle size decreases.

However, the explosion severity does not increase infinitely as particle size decreases. There is a critical diameter below which P_{max} and K_{St} values become independent on particle size [1]. This critical diameter depends on the combustion reaction mechanism established [52]. In organic materials (combustion in gas phase, yielding gaseous products), the critical diameter is obtained when the thermo-kinetic parameters reach the highest value, and the rapid pyrolysis-volatilization step causes that the explosion to become governed by an homogeneous combustion [126]. For instance, flour [127] and coal dust [18] present negligible changes on P_{max} and $(dP/dt)_{max}$ for particle sizes below 50 μm, and polyethylene and methylcellulose [127] exhibit a critical diameters of 40 μm. On the other hand, for metallic materials such as aluminum (combustion reaction on the solid surface), the critical diameter is considerably smaller. The dependency of explosiveness on particle size is very prominent in a wide range of sizes, even at nanoscale [128-131].

2.7.4. Agglomeration

Dust agglomeration is caused from inter-particle forces that tend to reduce the interfacial energy by reducing the total surface area [132]. Agglomerated particles

behave as particles of larger size that exhibit lower explosion hazards due to their reduced surface area [1]. The agglomeration susceptibility depends on the competition between attractive (*e.g.*, van der Waal forces, local physical and chemical linkages) and repulsive forces between particles (*e.g.*, electrostatic charges). These forces are affected by several factors, including surface energy, roughness, chemical characteristics, and inter-particles contact area [8]. Large particles present small attractive forces in comparison to gravitational and inertia forces, whereas smaller particles (< 10 μm) present attractive forces comparable to gravitational forces [8]. Hence, smaller particles are more prone to agglomerate [8, 133]. The breakup of this agglomeration is possible by varying the nozzle configuration and the dispersion air velocity during dust cloud formation [134]. However, the complete dispersion of nanoparticles is very difficult given that new agglomerates can be created after the dust cloud dispersion process by inter-particles collision [135]. Wu *et al.,* [136] and Bouillard *et al.,* [137] reported a reduction of the explosion hazards of aluminum nanopowder as particle size decreased. Hence, when agglomeration is expected, moving from microscale to nanoscale is safer [138]. Particle agglomeration can also arise from the addition of liquids to dusts which provide liquid bridges that favor particles' attractive forces [139]. In fact, liquid spraying is used in the industry to reduce dust explosion hazards by preventing dust cloud formation [1, 138].

2.7.5. Humidity content

Dust humidity content not only influences the effective particle size (by inducing agglomeration), but also the ignition sensitivity of combustible dusts [140]. Statistics of

dust explosions in the US confirm the increased explosion risks with reduction of humidity content [2]. For instance, seven out of the eight most catastrophic dust explosions in the US occurred during the winter, which is the driest season of the year [2]. The presence of water provides a heat sink effect by the water vaporization [140], while at lower humidity contents the susceptibility for thermal and spark ignition increases [141].

2.8. Dust explosions protection

Dust explosion protection is achieved by prevention and mitigation methods. Preventive systems aim to avoid the occurrence of the explosion while mitigation systems are used to reduce the consequences if the explosion takes place [1].

2.8.1. Prevention of dust explosions

A dust explosion is prevented by avoiding the formation of a dust cloud having fuel and oxygen concentrations above *MEC* and *LOC*, respectively; and by preventing the existence of ignition sources [1, 4].

2.8.1.1. Avoidance of dust cloud formation

Maintaining the fuel concentration below the MEC is not always feasible. Inside a process equipment, localized high concentration regions (> MEC) are unpredictable [1]. Outside the operational equipment, unintentional dust accumulations are usually prevented by proper housekeeping. One alternative to control the fuel concentration consists of premixing solid inerts with the combustible dust. For instance, coal explosions are prevented by mixing the coal with rock dust (dolomite and milestone) [142]. A disadvantage of this alternative is the elevated inertant concentration (>50%)

required to absorb the heat required for combustion [28, 142, 143]. Parameters such as particle size, specific heat, rate and temperature of decomposition influence the inertant effectiveness [25]. Manipulation of oxygen concentration is also very effective to prevent the dust cloud formation. Dust severity [144, 145] and ignition sensitivity [146] are systematically reduced by decreasing oxygen level. For instance, a slight reduction of oxygen concentration from 21 to 16%, moderates P_{max} and K_{St} values of coal dust explosions from 8.1 bar(g) and 124 bar-m/s to 6.8 barg(g) and 55 bar-m/s, respectively [145]. The limiting oxygen concentration (LOC) is used to determine the required inerting levels [102, 147]. An advantage of gaseous inerting is that gaseous additives such N_2 and O_2 do not result in product contaminations. However, it must be taken into account that nitrogen represents an asphyxiation hazard[148].

2.8.1.2. Avoidance of ignition sources

Typical ignition sources include, smoldering [149], open flames, hot surfaces, sparks from mechanical impact, electrical and brush discharges [150, 151]. Flameproof equipment is recommended to prevent open flames. Additionally, the selected equipment should not produce inductive or electrical discharges [152]. Prevent equipment overloading to reduce the chances of dust accumulations and hot spots. Removal of foreign materials (*e.g.*, loosed metal screws) by magnets is used to prevent friction sparks [152]. Ensuring grounding and bounding of equipment and transportable containers can also be used to minimize ignition sources [149]. Even with these precautions, total elimination of ignition sources is very difficult to achieve [48].

2.8.2. Mitigation of dust explosions

In some situations prevention methods are not enough to achieve acceptable levels of safety, and then it is necessary to implement mitigating methods to reduce the consequences of a dust explosion. Among the variety of available mitigation alternatives containment, venting and suppression will be discussed here.

2.8.2.1. Containment

Protection by containment consists of the design of the structure to be able to withstand the explosion. The equipment can be pressure or shock resistant. In the former case, the equipment should withstand the explosion without deforming; while in the second case, deformation of the process unit is allowed as long as rupture does not take place [73]. Containment might not always be economically viable, but it is used in small-scale plans or when the dust is highly toxic [148].

2.8.2.2. Isolation

This explosion protection method is used to avoid that the explosion propagates to other process units. Hollow *et al.,* [153, 154] and Lunn *et al.,* [155] studied the propagation of dust explosions in interconnected vessels. The dust explosion in one vessel was propagated to a secondary vessel through a pipe. Due to the increased turbulence and flame acceleration through the pipe, the secondary vessel experienced a more severe explosion. This pressure increase depended on the pipe diameter and length [153]. Simulation results in interconnected vessels showed that in addition to the pipe characteristics, the severity of the secondary explosion was also affected by the ignition

position [64]. The results confirm the importance of dust explosion protection by isolation.

2.8.2.3. Suppression

The objective of a suppression system is early detection of the explosion to stop it by injecting of a material able to absorb the heat required to sustain the explosion [28]. This active protection system includes detection, initiation and action [148], hence it is relatively complex and expensive. A variety of investigations have been conducted to evaluate the efficiency of different materials as dust explosion suppressants [25, 29, 156]. Common solid suppressant agents include, monoamonium phosphate ($NH_4H_2PO_4$) [25, 157], sodium and calcium bicarbonate ($NaCO_3$ and $CaCO_3$) [25, 26], sodium chloride [27], and rock dust. In addition to the effectiveness of the suppressant agent, other parameters such as the velocity of pressure rise detection and injection are crucial for an effective suppression system. Too early suppressant injection might prejudicially increase the turbulence of the incipient explosion and late injection might not be able to control the explosion [30].

2.8.2.4. Venting

Using venting as a protective system, the explosion occurs and at a specific pressure a vent opens to release burned and unburned products into the surroundings, relieving destructive overpressures [158]. Venting is a one of the most common protection systems due to its convenient implementation and low cost [159]. Figure 8 shows the comparison between the pressure profiles and maximum pressures reached during a vented and unvented dust explosion. The maximum pressure obtained during a

vented dust explosion is called reduced pressure (P_{red}). This parameter along with P_{max} and K_{St} values are useful to calculate the venting area required to ensure an explosion overpressure is within the accepted safety levels [46, 160, 161]. The development of models to predict the evolution of a vented dust explosion is very difficult due to the variety of parameters affecting this process. An extensive literature review of vented explosions through ducts is included in Chapter VI.

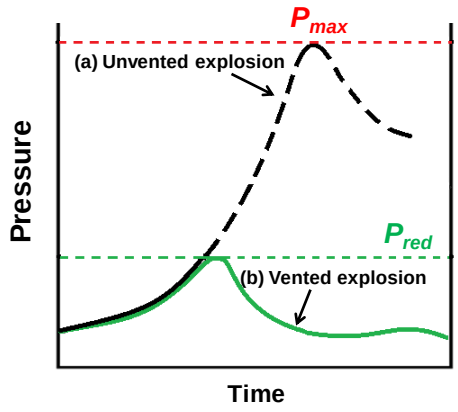

Figure 8. Typical pressures profile during a dust explosion (a) unvented and (b) vented. Adapted from [1].

2.9. Conclusions

Proper identification of dust explosion hazards is essential to develop optimal safety measures. Several explosion indexes used to categorize the dust explosion hazards are measured in the 1 m^3 and 20 L vessel. The application of dust explosion testing in constant volume equipments is threefold: 1) determine the severity of a dust

explosion, 2) estimate the velocity of the flame propagation and 3) identify the influence of particle and process parameters on the evolutions of a dust explosion. Furthermore, empirical equations allow the correlation between turbulent and laminar burning velocity, which is a more fundamental parameter used to describe the evolution of the explosion.

Significant efforts have been done by scientists to predict the evolution of dust explosions. However, experimental determination of the explosion severity and burning velocity is still frequently required at varying particle properties (*e.g.*, particle size, humidity content) or operation conditions (*e.g.*, pressure, temperature, turbulence). Moreover, despite the variety of prevention and mitigation methods to reduce dust explosion consequences, the recurrence of these events encourage more research toward a deeper understanding of a dust explosion event to improve the measurement of explosion indexes, advance the characterization of influencing parameters, and develop alternative and more effective solutions to prevent and mitigate dust explosions.

CHAPTER III

DESIGN, AUTOMATIZATION AND CALIBRATION OF A 36 L DUST EXPLOSION EQUIPMENT

3.1. Introduction

Constant volume equipment is commonly used to measure thermodynamic and kinetic combustion parameters of a dust explosion. The ISO standard refers to the 1 m^3 dust explosion vessel to determine P_{max} and K_{St} values of a combustible dust [55]. Although, smaller dust explosion vessels (*i.e.,* 20 L) have been developed to reduce costs, both in terms of work and the amount of sample used [99, 107, 162]. Vessels smaller than 20 L are not recommended to measure K_{St} values because flame area distortion by the vessel walls might affect the accuracy of the results [93]. During the calibration process of a dust explosion equipment, the pre-ignition turbulence is manipulated in order to reproduce the K_{St} results obtained using the 1 m^3 vessel. The pre-ignition turbulence is mainly affected by the injection velocity of the dust cloud into the vessel and the ignition delay time [56]. The 20 L vessel has been extensively validated against the 1 m^3 vessel [55, 99, 107]. For instance, similar K_{St} values are obtained in the 20 L and the 1 m^3 vessel using an ignition delay time of 60 ms and 600 ms, respectively [99]. However, van der Wel *et al.,* [52, 99] showed that the K_{St} results are not always in good agreement especially when the dust dispersability affects the pre-ignition turbulence. This suggests that an additional analysis of the turbulence inside the equipment is required to complement the equipment calibration.

The turbulence generated during the transient dispersion of air and dust into the explosion vessel significantly affects the dust burning rate [84]. Several authors have measured the decay of turbulence levels inside the standard 20 L vessel during the dispersion process [70, 73, 84, 87], and empirical correlations and models have been developed to account for these effects [83, 91, 163, 164]. Some of these correlations are only valid for the equipment where they have been measured (*i.e.,* 20 L vessel [83]). In this study, due to the complexity and high cost of turbulence measurements during the dispersion process in the 36 L vessel, an approximation of the turbulence decay was obtained using computational fluid dynamic (CFD) simulations.

This chapter details the 36 L dust explosion equipment set up, automatization, and calibration. The approach followed to calibrate the 36 L vessel is similar to the procedure followed to validate the 20 L vessel with respect to the 1 m^3. The analysis of turbulence induced during dust cloud formation was performed using the Flame Acceleration Simulator (FLACS), which is a commercial software widely validated for gas dispersion and explosion simulations [82, 165, 166]. The standard 20 L vessel has been taken as a reference to design the 36 L vessel configuration and operation mode. It is expected that the same methodology can be used for calibrating other equipment with different configurations, where transient decay of turbulence has a strong effect in the course of dust or gas explosions.

3.2. Dust explosion equipment overview

The dust explosion equipment used in this work utilizes a 36 L vessel shown in Figure 9. The semi-spherical stainless steel vessel has a wall thickness of 1.6 in (4 cm)

and two main openings of 4.5 and 2.5 in diameter at the top and the bottom, respectively. The vessel was hydrostatic tested, its maximum allowing working pressure (MAWP) is 1000 psia, and its maximum allowable temperature is 500 ºF. Appendix A shows details of the vessel dimensions.

Figure 9. Dust explosion equipment.

The vessel is equipped with a vacuum, a dispersion, an ignition and a data acquisition system. The equipment diagram is shown in Figure 10. The vacuum system consists of a filter (F) and a vacuum pump (P). The dust dispersion system includes a 1-L air reservoir (R) connected to an electrical fast acting valve (V2), a check valve (V3), a dust container (DC), and a rebound nozzle (N). Initially, V2 was a pneumatic valve (Swagelok: SS-63TS12-33DCB-L1). However, due to its delayed actuation, it was replaced by an electrical valve (ASCO P/N: 8210G026). Appendix B shows details of the pneumatic valve actuation delay time analysis. The ignition system consists of two chemical igniters (IG, Cesana Corporation) connected to a pair of electrodes installed in the reactor top flange (FG1), so the igniters can reach the vessel central point. For gas explosions, an electric spark ignition source is also available. Appendix C shows details of the spark generator. The data acquisition system (DAQ) processes information from one pressure transducer connected to the vacuum system (PT0), two static pressure transducers (SPT1, SENSOTEC P/N: 060-3147-01 and SPT2 OMEGA P/N: PX309-500G5V) and one dynamic piezoelectric pressure transducer (DPT1, PCB Piezotronics P/N: CA102A04) connected to the vessel wall. Appendix D includes specifications of main equipment components.

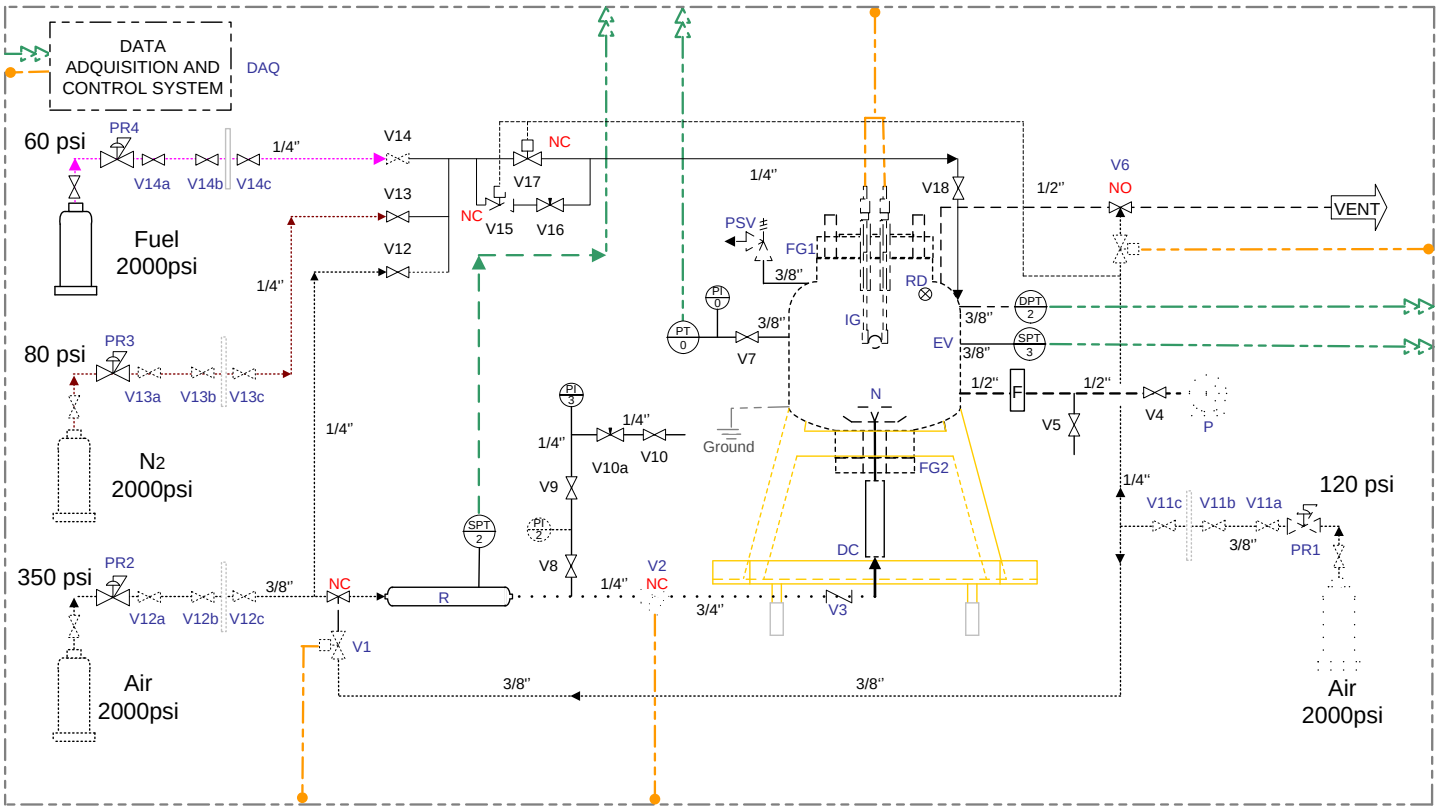

Figure 10. 36 L dust explosion equipment diagram.

3.3. Data acquisition hardware and control panel

The data acquisition hardware and control panel allows the remote and manual activation of solenoid valves (V1, V2, and V6) and chemical igniters. The control box shown in Figure 11 has dimensions of 13×17×4 in (L×W×H). A capacitor coupled to the powder source provides a 24-volts peak required for the igniter's activation. Three solid state relays connected to a 5-volt supply are used to control V1, V2, and V6. A 16-bit PCI-6251 card (National Instruments) connects all the measurement and control devices to a computer. Figure 12 shows a detailed description of the PCI-6251 card connections. A detailed electrical schematic for the 36 L vessel control box is shown in Appendix E.

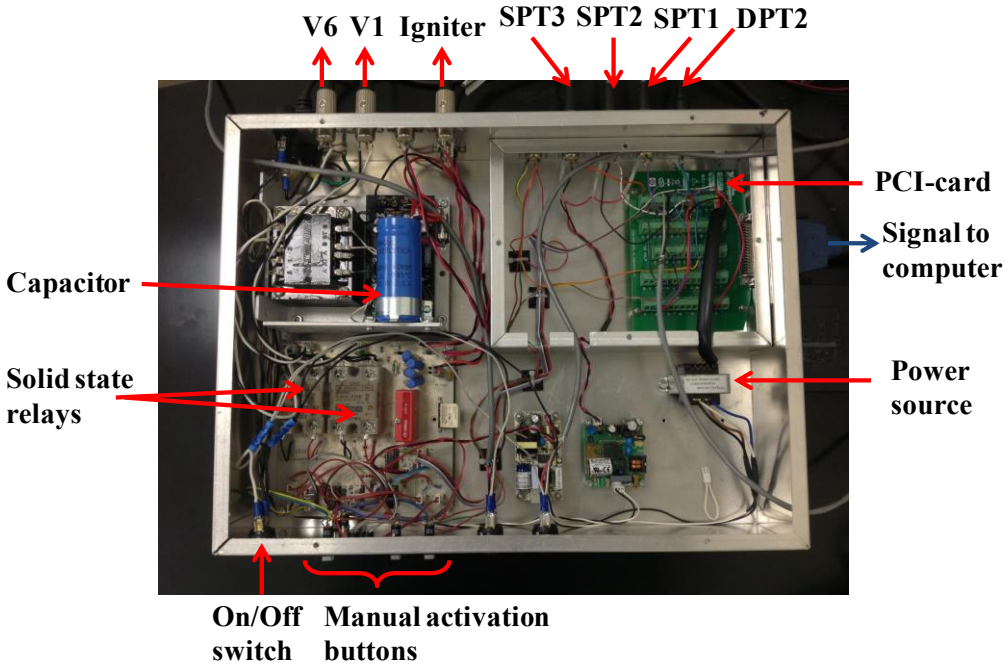

Figure 11. Control box of the 36 L dust explosion equipment.

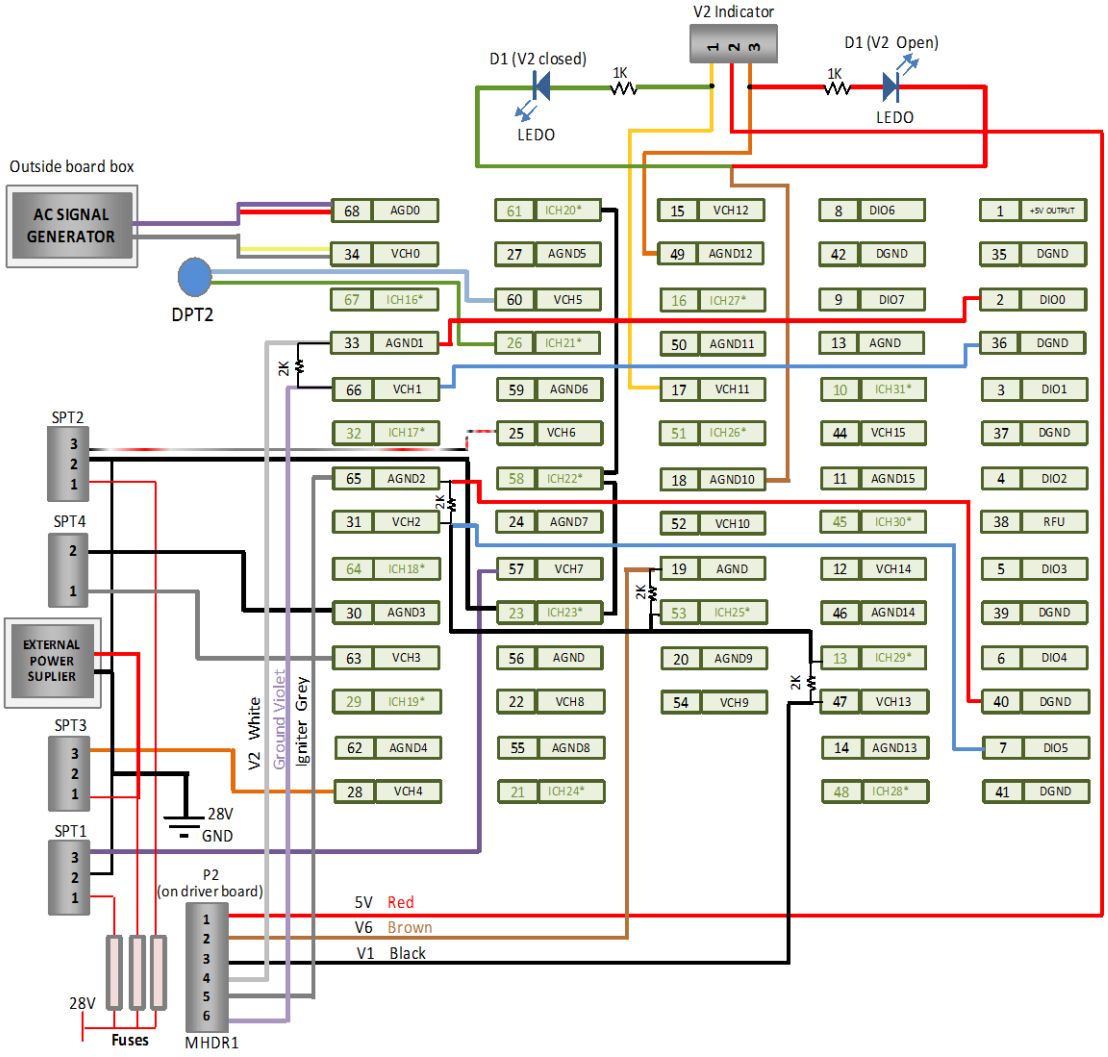

Figure 12. Equipment data acquisition card (PCI-6251, National Instruments) and control connections.

3.4. Safety measures

Several safety measures were designed to protect the operator of the equipment. The main hazardous scenarios and corresponding safeguards are listed below:

- Undesirable dust or gas releases: The entire equipment system is installed into a canopy hood to provide adequate ventilation during equipment operation and cleaning. An elephant trunk located above the vessel opening is used to exhaust gases and particulate residues from the explosion tests. To prevent dust dispersion by accidental actuation of the solenoid valves, a safety button located in the control panel should be simultaneously pulsed during their manual operation.

- Unexpected dust cloud ignition: The vessel is grounded to avoid ignition sources from electrostatic discharges. To prevent undesired activation of the chemical igniters, an interlock system maintains in open position the electrical circuit to the electrodes until the vessel and the enclosure box are closed.

- Equipment overpressure: The equipment has a manual and automatic safety shutdown system. V1 and V2 fail close to prevent air entrainment into the 36 L vessel, and V6 (venting line) fails open to relieve any overpressure at the reactor. Additionally, the reactor is equipped with a pressure relief valve and a rupture disc set to 500 and 1000 psia, respectively. Sizing of the pressure relief system is found in Appendix F.

3.5. Operation mode

The equipment operation mode is based on ASTM standard E-1226-05[58]. In a dust explosion test, a dust sample is loaded into the dust container, then the 36 L vessel

is closed, evacuated, and the air reservoir is pressurized. A fast acting valve (V2) is opened, for 50 ms, to transfer air from the reservoir and disperse the sample inside the vessel through a rebound nozzle. This dispersion process increases pressure inside the vessel pressure to 1 bar absolute. Subsequently, after a delay time of 25 ms, two 5 kJ chemical igniters are activated and the resulting explosion pressure profile is recorded. A customized LabView™ program controls the equipment and processes the data from the experiments. This test procedure is slightly different to the procedure of the 20 L vessel presented in section 2.1.1. The operation conditions are different and the sample is dispersed by the pressurized air, instead to be premixed with air in the dust container. However, the typical experimental results are the same as shown Figure 5. The detailed operation procedure of the 36 L dust explosion equipment is found in Appendix G.

3.6. Automated software (LabView™)

The equipment was automated using LabView™ to ensure precise equipment control along with a consistent data collection and analysis. LabView™ is a graphical programming platform that provides a dynamic user-equipment interaction. To remotely control the equipment, the customized program has a virtual channel corresponding to each device connected to a physical terminal at the PCI card (Appendix H).

The general structure of the LabView program is summarized in Figure 13. This program is used to input information about the sample and operation conditions, to control the air injection into the reservoir and the vacuum level inside the vessel. Then, it displays a safety alarm to close the igniters' safety interlock and initiates the test by activating V2 and IG. The program automatically collects, processes, and stores the data

under a unique file number. Finally, it displays a series of graphs summarizing the experimental results, including P_{ex}, $(dP/dt)_{ex}$, V2 and IG voltage signals as a function of time.

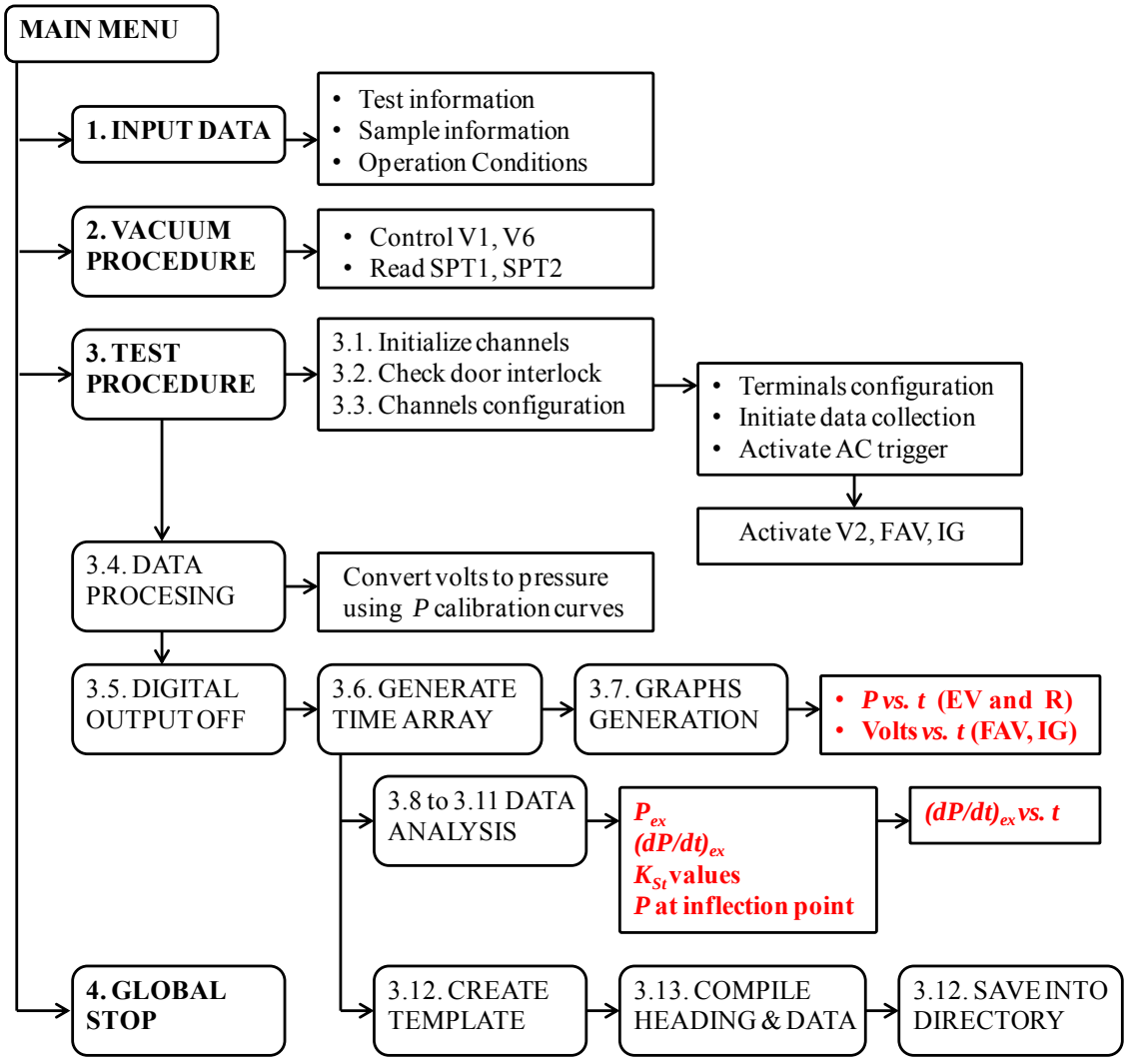

Figure 13. Simplified LabView™ program structure.

To precisely control V2 and IG activation time, their signal channels were connected to two counters at the PCI card that work as internal clocks. Once the test is initiated, an external trigger consisting of an AC sine signal drives the V2 and IG counters to initiate in phase. Thus, the events sequence is consistently controlled through LabView™. Pressure transducers signal noise is minimized by collecting data at a high scan rate (5000 Hz) and averaging the results every 10 data points.

3.7. Equipment calibration

The 36 L vessel was calibrated by adjusting the operating conditions until P_{max} and K_{St} were similar to the results obtained with a standard 20 L vessel and the 1 m^3 vessel. The calibration process was divided into two steps: 1) selection of optimum equipment operating conditions and 2) characterization of a combustible sample previously tested in standard calibrated equipment.

3.7.1. Selection of equipment operating conditions

Initially, the dispersion system was calibrated to yield atmospheric pressure inside the reactor after air and dust injection. Three parameters were manipulated (vacuum level, reservoir pressure (P_r), and dispersion time (t_{FAV})) to generate 15 possible combinations (Appendix I). Subsequently, a 2^k factorial experimental design was used to identify the relative influence of equipment operating conditions on K_{St} values. Using k equal to 3, three factors were evaluated and each factor was tested at two discrete levels (*e.i.*, 2^3 factorial design), as shown in Table 3 [167, 168] The levels were initially selected based on operating conditions from a calibrated 26 L equipment [169].

Table 3. Factors and levels used in the 2^3 factorial experimental approach

	Factors		Low Level (-1)	High Level (+1)
A	t_{FAV}	Fast acting valve time, ms	300	400
B	t_{ig}	Ignition delay time, ms	20	50
C	P_r	Reservoir pressure, bara	15 (221 psia)	18 (261 psia)

The systematic combination of factor levels and the corresponding K_{St} results from coarse cornstarch explosions are shown in Table 4.

Table 4. Experimental results and calculations following the 2^3 factorial approach

$z \rightarrow$	A	B	C	AB	AC	BC	ABC	y_i (bar-m/s)
1	-1	-1	-1	1	1	1	-1	13.8
2	-1	1	-1	-1	1	-1	1	7.44
3	1	-1	-1	-1	-1	1	1	6.78
4	1	1	-1	1	-1	-1	-1	6.62
5	-1	-1	1	1	-1	-1	1	12.27
6	-1	1	1	-1	-1	1	-1	10.32
7	1	-1	1	-1	1	-1	-1	6.84
8	1	1	1	1	1	1	1	6.80
$q_z{}^2$	4.40	1.13	0.04	1.03	0.02	0.32	0.29	
$Q_z = \frac{q_z^2}{8}$	35.24	9.05	0.32	8.22	0.15	2.57	2.30	$\sum_z Q_z = 57.85$
$Y_z = \frac{Q_z}{\sum Q_z}$	**61%**	16%	1%	14%	0%	4%	4%	$Y = 100\%$

Each row in this table corresponds to a dust explosion test. For example, row 1 represents a test conducted using P_r = 221 psia, t_{FAV} = 300 ms and $t_{ig} = t_{FAV}$ + 20 ms. The y_i column corresponds to the resulting K_{St} value. The effect of factors interaction is shown in columns AB, AC, BC, ABC. Each factor contribution (q_z) is given by [168]:

$$q_z = \frac{1}{2^3}\sum_i x_{z,i} y_i \quad \textbf{(24)}$$

where $x_{z,i}$ corresponds to column z and row i coefficient. This analysis shows that t_{FAV} is the most influencing factor on K_{St} values (61%). From these experimental results, the calibration procedure was guided toward lower t_{FAV} and higher P_r values. Higher K_{St} values were obtained in subsequent experiments using P_r equal to 21.7 barg, t_{FAV} between 50 to 100 ms, and t_{ig} in a range of 10 and 20 ms, respectively.

Finally, to clearly define t_{FAV} and t_{ig} values, two different niacin samples ($C_6H_6N_2O$) with known P_{max} and K_{St} values were utilized. These samples were previously used in a calibration round robin (CaRo). During this type of calibration a dust sample is characterized by different laboratories located around the world. Then, the results are compiled and compared against the mean value of all the laboratories. In this case, a niacin sample, from CaRo-1998, with a K_{St} value of 236 bar-m/s at 550 g/m^3 was used to define t_{FAV}, and a niacin sample from CaRo-2003, with K_{St} equal to 232 bar-m/s at 880 g/m^3 was used to define t_{ig}. The operating conditions of the 36 L vessel used in this procedure and K_{St} results are summarized in Table 5.

Table 5. K_{St} results obtained at different operating conditions using the 36 L vessel

Objective	P_r (bara)	t_{FAV} (ms)	t_{ig} (ms)	K_{St} (bar-m/s)	Reference K_{St}	Deviation from reference
Identify t_{FAV}	21.7	100	20	195	236 bar-m/s (CaRo-1998)	-18%
	21.7	75	20	225		-5%
	21.7	50	20	254		7%
Identify t_{Ig}	21.7	50	20	268	232 bar-m/s (CaRo-2003)	16%
	21.7	**50**	**25**	**231**		**-1%**
	21.7	50	30	219		-6%
	21.7	30	50	186		-20%

The set of operating conditions that gave a K_{St} value with the lowest deviation from the reference was selected. The operating conditions for the 20 L and 36 L vessels are summarized in Table 6.

Table 6. Operation conditions of the 20 L and 36 L dust explosion vessels.

Component/ Operating conditions	Standard 20 L vessel	36 L vessel
Vessel volume	20 L	36 L
Reservoir volume	0.6 L	1 L
Initial vessel pressure	0 barg	0 barg
Initial reservoir pressure (P_{ri})	20 bara	21.7 bara
Initial vessel pressure (P_{vi})	-0.6 barg	-0.3 barg
Vessel pressure after dispersion (P_{fi})	0 barg	0 barg
Fast acting valve time (t_{FAV})	45 ms	50 ms
Ignition delay time (t_{Ig})	15 ms	25 ms

3.7.2. Explosive characterization of niacin dust

The operating conditions previously defined were used in the 36 L vessel to reproduce experimental data from other calibrated equipment. Niacin and lycopodium are samples commonly used in calibrations of similar equipment to the 36 L vessel. In this case, a pyridine-3-carboxamide dust (niacin) sample ($C_6H_6N_2O_2$) having a D_{50} of 28 μm was tested. This sample was previously used during the Round Robin calibration (CaRo 00/01) [70, 170]. The combustion reaction of niacin in air is [171]:

$$2C_6H_6N_2O_2 + (25/2)O_2 \rightarrow 12\ CO_2 + N_2 + 6H_2O$$

The stoichiometric niacin dust concentration corresponds to 168 g/m^3 [171]. The sample was tested in "as received" condition. The results from the 36 L vessel were compared with results obtained in a 20 L vessel [70] and the values reported from CaRo 00/01[170], using the same sample (Figure 14). Note that CaRo 00/01 results represent the average values of explosive dust characteristics from 41 vessels using the same sample.

The data obtained in the 36 L vessel presented a good repeatability. Aditionaly, experimental results (P_{max} = 8.3 ± 0.2 barg and K_{St} = 238 ± 12 bar-m/s) were in agreement to data reported by Skjold for 20 L [70] (P_{max} = 8.5 ± 0.1 barg and K_{St} = 238 ± 19 bar-m/s) and results reported from CaRo 00/01 for 20 L [170] (P_{max} = 8.4 ± 0.8 barg, K_{St} = 220 ± 22 bar-m/s).

To analyze the equipment precision, 12 niacin dust explosions were repeated using the same experimental conditions. Appendix J includes the experimental results and Table 7 summarizes the mean values ($\bar{x}$) and resulting standard deviations (*StDev*).

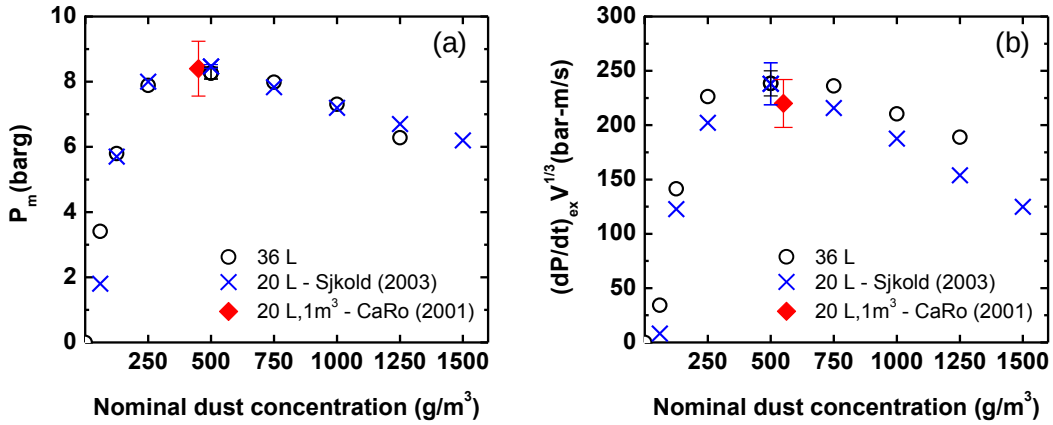

Figure 14. Explosive characteristics of niacin ($C_6H_6N_2O_2$) for different nominal dust concentrations. (a) P_m and (b) $(dP/dt)_{ex}V^{1/3}$

Table 7. Dust explosion equipment precision analysis

Conc. **500 g/m^3**	$P_{r,i}$ **(barg)**	$P_{r,f}$ **(barg)**	$P_{v,i}$ **(bara)**	$P_{v,f}$ **(bara)**	P_{ip} **(barg)**	τ **(ms)**	t_m **(ms)**	P_m **(barg)**	K_{St} **(bar-m/s)**
$\bar{x}$	20.7	10.4	0.7	1.0	4.3	19.5	31.1	8.3	238
StDev	0.0	0.3	0.0	0.0	0.1	2.1	2.9	0.2	12

$P_{r,i}$ and $P_{v,i}$ correspond to the reservoir and vessel initial pressures, respectively. $P_{r,f}$ and $P_{v,f}$ correspond to the reservoir and vessel pressure after air dispersion. P_{ip} and t_{ip} correspond to pressure and time at inflection point and t_m is the time at the maximum pressure. $P_{v,f}$ values can be calculated from the following mass transference equation:

$$n_{v,f} = n_{v,i} + (n_{r,i} - n_{r,f}) \quad \textbf{(25)}$$

where n_v and n_r represent the moles in the vessel and the reservoir, respectively. The initial and final states are indicated by the subscripts *i* and *f*, respectively. Thus, the difference between n_v and n_r will correspond the moles of air transferred from the reservoir to the vessel. Assuming ideal gas behavior and using initial and final vessel and reservoir temperatures equal to 25°C:

$$\frac{P_{v,f}V_v}{RT} = \frac{P_{v,i}V_v}{RT} + \frac{P_{r,i}V_r}{RT} - \frac{P_{r,f}V_r}{RT} \quad \textbf{(26)}$$

$$P_{v,f} = \frac{P_{v,i}V_v + (P_{r,i} - P_{r,f})V_r}{V_v} \quad \textbf{(27)}$$

where, V_v corresponds to the vessel volume (36 L), V_r is the reservoir volume (1 L), *R* and *T* correspond to the ideal gas constant and temperature, respectively.

For instance, using the first data set shown in Appendix J, the vessel pressure after dispersion can be calculated as follows:

$$P_{v,f} = \frac{0.71\ (bara) \times 36(L) + \big(20.75\ (bara) - 9.83(bara)\big) \times 1(L)}{36\ (L)}$$

$$P_{v,f} = 1.01\ (bara)$$

3.8. Analysis of initial turbulence levels using CFD simulations

The transient nature of the dust dispersion process significantly complicates the process of extracting relevant combustion parameters from small-scale dust explosion experiments, and additional information regarding the decay of turbulence in dust explosion vessels is required to estimate parameters such as the laminar burning velocity S_L. The present section aims at investigating the relationship between results obtained in vessels of different sizes using CFD simulations. Two vessels specifically are to be

compared, a standard 20 L vessel at the University of Bergen [70] and a 36 L vessel at the Mary Kay O'Connor Process Safety Center (MKOPSC). These CFD simulations were performed using FLACS. This software solves momentum, mass, and energy balances; transport equations for fuel; mixture fractions; and energy generated and dissipated by turbulence, all in finite volumes [81, 82]. FLACS has been widely validated for gas explosion simulations [82, 165, 166]. The geometry models implemented in FLACS for the 20 L and the 36 L vessels are shown in Figure 15a and b, respectively.

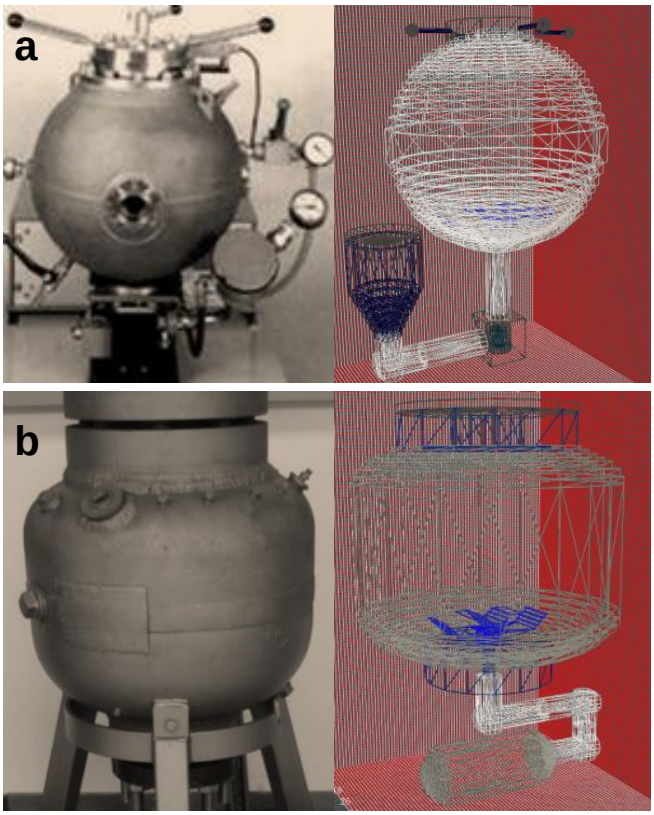

Figure 15. Actual vessels and models for (a) a 20 L vessel and (b) a 36 L vessel.

Besides the size and shape, both pieces of equipment differ in their dispersion systems. In the 20 L vessel the dust sample is loaded into a 0.6 L reservoir, pre-mixed with pressurized air and then dispersed into the vessel through the fast acting valve (FAV). Due to the high velocity flow of this mixture through the piston shape valve, the dust sample might experience reductions in particle size [172]. This potential reduction of particle size is prevented using the configuration of the 36 L vessel. The dust sample is loaded into a dust container located downstream of the FAV. Thus, the dust sample does not flow through the valve as it is transferred to the vessel.

The dispersion scenario set up in FLACS was based on operating conditions shown in Table 6. Cubical grid cells with sides of 0.06 meters were used in all the simulations. To imitate the initial vacuum level in the vessels, the initial ambient pressure in the total control volume was specified as -0.6 and -0.3 barg for the 20 L and 36 L vessel, respectively. A SETUP file was required to specify an initial high pressure region in the air reservoir equal to 20 and 21.7 barg for the 20 L and 36 L vessel, respectively. Additionally, an EVENTS file was used to place a panel in the vertical inlet pipe to mimic the opening and closing of the FAV. The rebound nozzle geometry was built using vertical and horizontal panels that match the grid limits. Once the simulation is started, the air in the high pressure region is injected into the vessel through the nozzle and then the artificial FAV is closed. The CFD simulations were performed without considering the actual delay opening time for the valve. Simulated results of the

air dispersion process and experimental results during a dust explosion in the 20 L and 36 L vessels are shown in Figure 16.

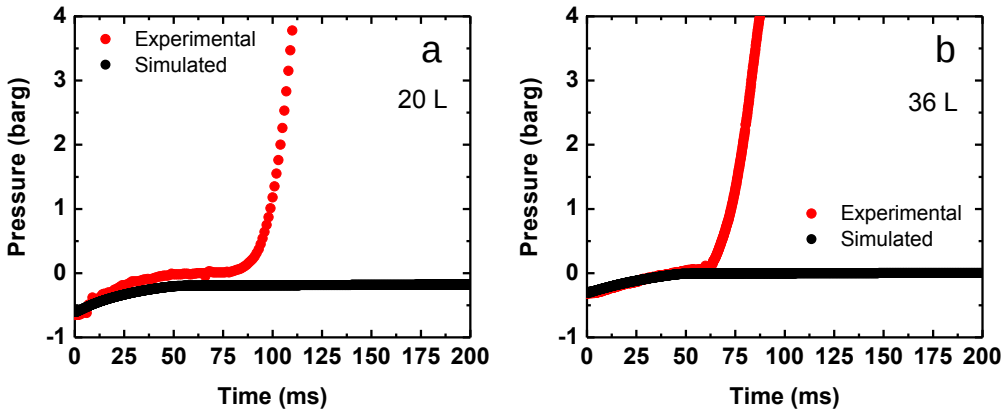

Figure 16. Simulated and experimental pressure-profiles during the air dispersion process for (a) a 20 L vessel and (b) a 36 L vessel.

The simulated pressure values provided a fairly good representation of the experimental pressure evolution during the dispersion process. The simulations presented in Figure 16 were subsequently used to determine the turbulence decay following the dispersion process in the 20 L and the 36 L as shown in Figure 17.

Figure 17 shows the comparison between the u_{rms} values obtained from the FLACS simulations. FLACS models turbulence with the standard k-ε model, where the root-mean-square of the turbulent fluctuation velocity are modeled as [70]:

$$u'_{rms} = \sqrt{\frac{2}{3}k}$$

where k is the turbulent kinetic energy from the k-ε model. The simulated results were compared to the values obtained from the empirical correlation of turbulence decay developed by Dahoe *et al.*,[83, 84], presented in section 2.3. (Equation 21, pag 20). The equation is valid for a range between 60 and 200 ms [81, 84].

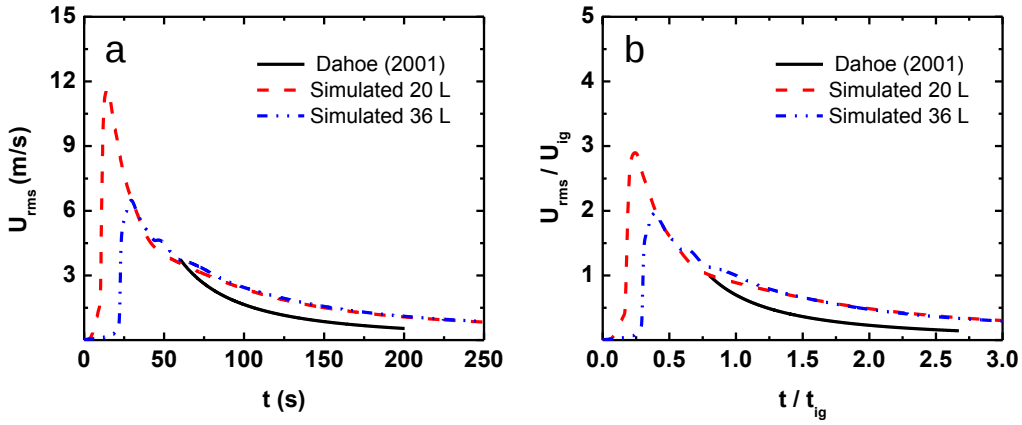

Figure 17. Simulated results for turbulence decay after air dispersion in the 20 L and 36 L explosion equipment. (a) root-mean-square velocities (u_{rms}). (b) Normalized values with respect the ignition point.

As shown in Figure 17, turbulence decay in the 36 L vessel has a similar tendency as the 20 L vessel. In agreement with previous experimental observations [70], the turbulence rapidly increases during the first 10 ms and the isotropic decay period

starts around 30 ms after the onset of air injection [73]. To account for differences in the ignition delay time in both pieces of equipment (60 ms and 75 ms, for the 20 and 36 L vessel, respectively), the u_{rms} values were normalized with respect the values obtained at ignition point (Figure 17b). The curves were compared after t/t_{ig} equal to 1 which corresponds to the time range where the explosion is triggered. Despite the vessels considered here having different size, shape, and initial operating conditions, the decay of turbulence at ignition time (t/t_{ig} = 1) is in good agreement to calculated values using empirical correlations from Dahoe, *et al.,* [84]. Although the simulations were limited to pure air dispersion, it is foreseen that this methodology can be used for obtaining approximate estimates for the turbulence levels in equipment of different size and shapes where direct measurements are not possible.

3.9. Estimation of laminar burning velocity from pressure measurements

The correlations to estimate S_L presented in section 2.3 are valid for experimental combustion parameters obtained from the 20 L vessel [81]. To validate these correlations for S_L estimations using experimental parameters obtained in the 36 L vessel, the same cornstarch sample was tested in a calibrated 20 L and the 36 L vessels. Then, P_{max}, K_{St} values and S_L calculations were compared.

In this case, dust explosion tests were conducted using cornstarch $(C_6H_{10}O_5)_n$ having D_{50} equal to 15 µm. The samples were dried in a vacuum oven at 70°C during 24-hr (3% humidity) and 48-hr (0% humidity) time periods to identify the effect of the humidity content on the explosion parameters. The samples were tested in the 36 L vessel at MKOPSC and the 20 L vessel at Gexcon A.S. (Norway). The explosive

characteristics of these samples were additionally compared against reference data from a 20 L vessel at the University of Bergen [173] as shown in Figure 18.

Experimental results in the 36 L vessel (P_{max} = 8.1 ± 0.2 barg and K_{St} = 179 ± 8 bar-m/s) were in very good agreement to results reported by Skjold (P_{max} = 8.7 ± 0.2 barg and K_{St} = 170.8 ± 7.0 bar-m/s)[173]. The experimental results obtained in the calibrated 20 L vessel at Gexcon A.S. presented a large data scattering as concentration increased beyond 750 g/m^3. The results might be attributed to poor dust dispersion inside the vessel. Hence, $(dP/dt)_{ex}$ values are less reliable for concentrations above 1000 g/m^3.

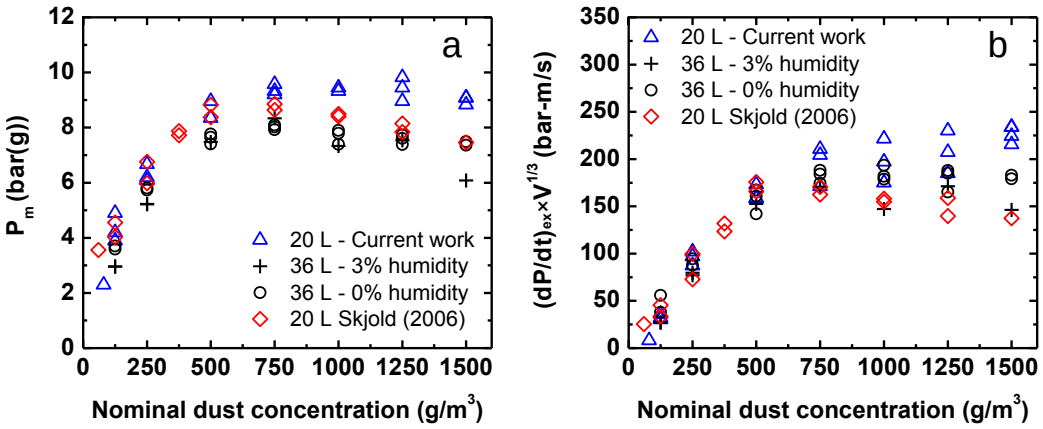

Figure 18. Explosive characteristics of cornstarch dust for different nominal dust concentrations. (a) P_m and (b) $(dP/dt)_{ex}V^{1/3}$. Samples tested in the 20 L vessels have 0% humidity content.

The experimental results obtained at 750 g/m^3 (P_{max} = 9.4 ± 0.2 barg, K_{St} = 195 ± 21 bar-m/s) are very consistent with the results obtained in the 36 L vessel and other reference values [173]. It was observed that 0 to 3% difference on the humidity content does not cause significant changes on the cornstarch explosion severity.

The experimental data from cornstarch (0% humidity content) explosions conducted in the 20 L and the 36 L vessels was used to calculate S_L using the methodology described in section 2.3. To account with the differences in the ignition delay time in both pieces of equipment, t_0 was equal to60 and 75 ms for the 20 L and 36 L vessel, respectively, in equations 21 and 22. The estimated burning velocities are shown in Figure 19.

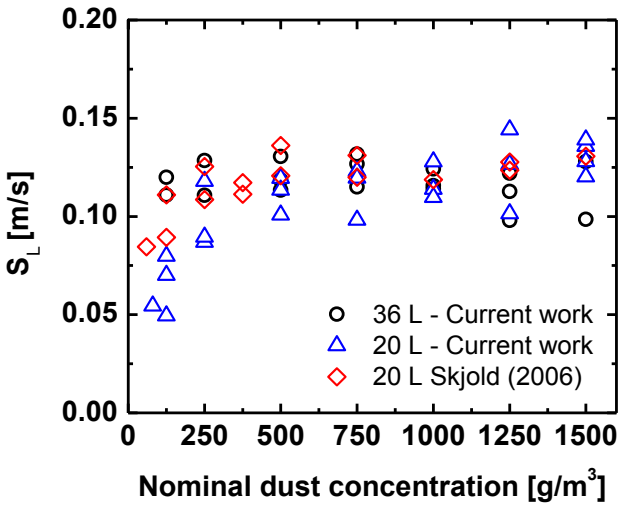

Figure 19. Estimated laminar burning velocities for cornstarch-air mixtures at different dust concentrations using a standard 20 L and our 36 L vessel.

The S_L values obtained using experimental data from 36 L vessel (S_L = 0.12 ms ± 0.01) were in very good agreement with the S_L values obtained from the 20 L vessel (S_L = 0.11 ms ± 0.03) and the reference values (S_L = 0.14 ms ± 0.12) [173]. Results presented in Figure 19 suggest that the combustion model presented in section 2.3, developed for the 20 L vessel [81, 82], can also be used to predict S_L values using experimental data obtained in the 36 L vessel.

3.10. Conclusions

A 36 L dust explosion vessel was assembled and calibrated at Mary Kay O'Connor Process Safety Center. The equipment automation using LabView™ facilitated the apparatus control, provided a consistent data collection and analysis, and enhanced the results repeatability. The experimental procedure for the 36 L vessel was validated by comparing explosion parameters, such as P_{max} and K_{St} values obtained for the same type of solid fuels in the standard 20 L and the 36 L vessels. Experimental results of niacin and cornstarch dust obtained in the 36 L vessel were in excellent agreement with reference values. FLACS simulations were used to examine the air dispersion process in the 20 L and 36 L vessels. The simulated turbulence during air dispersion in both vessels was compared to empirical correlations of dust-air dispersion developed by Dahoe *et al.,* [83, 84]. Although the vessels considered here had different size, shape, dispersion system, and initial operating conditions, the simulated air turbulence levels were very similar in the time range when the explosion occurs (60 ms to 200 ms).

Finally, S_L estimations using experimental results obtained from the 20 L and 36 L vessels were in good agreement. It is expected that the methodology outlined in this chapter can be used to guide the calibration process of dust explosion equipment having different sizes and shapes. Moreover, a similar simulation strategy can be conducted to analyze the velocity profile during the dispersion process and roughly estimate the turbulence levels inside the vessel where direct measurements are not possible.

CHAPTER IV

THE EFFECT OF PARTICLE SIZE POLYDISPERSITY ON THE EXPLOSIBILITY CHARACTERISTICS OF ALUMINUM DUST

4.1. Synopsis

This paper reports on experimental results elucidating the effect of particle size polydispersity (σ_D) on the explosion severity of aluminum dust. Five mixtures with a median diameter (D_{50}) of 15 μm and σ_D values of 0.95, 1.17, 1.48, 1.87, and 2.51, were systematically prepared by mixing original aluminum samples having narrow size distributions. The explosion severity of each sample was determined in a 36 L dust explosion vessel by measuring the maximum pressure (P_{max}), the maximum rate of pressure rise ($(dP/dt)_{max}$), and the deflagration index (K_{St}). The ignition sensitivity of the blends was assessed in terms of the minimum ignition energy (*MIE*) using a MIKE3 apparatus. Interestingly, results showed that values of P_{max}, K_{St} and *MIE* revealed an increase in explosion severity as σ_D increases, where K_{St} and *MIE* presented a more dramatic effect due to the contribution of fine particles on the combustion kinetics. The burning velocity of the original samples was calculated using a simplified dust combustion model. The effect of dust concentration on the explosion propagation was analyzed comparing the time span to reach $(dP/dt)_{max}$, (τ), during a dust explosion. τ was obtained from the experimental pressure traces of the original samples and their mixtures. The values of P_{max}, K_{St} and *MIE* were plotted as a function of the median diameter (D_{50}) and the volume- ($D_{4,3}$) and surface- ($D_{3,2}$) weighted mean diameters. The

surface weighted mean diameter $D_{3,2}$ provided a better description of the average sample size and D_{50} was inadequately related the real hazard potential of aluminum dust. Therefore, it is suggested that the explosion hazard characterization of these types of materials should be reported in terms of $D_{3,2}$ and σ_D.

4.2. Introduction

A dust explosion is a surface-area dependent process [1, 52]. Consequently, the parameters utilized to predict the consequences (P_{max} and K_{St}) and ignition sensitivity (MIE) of a dust explosion for a given scenario must be reported along with the median diameter (D_{50}). This work demonstrates that dust explosion hazards can be affected not only by the mean diameter but also by the size polydispersity (σ_D). σ_D is a measure of the width of the particle size distribution (*PSD*) and is not frequently reported along with the mean diameter [22, 23]. σ_D can affect K_{St} values [24], and significant uncertainties can be found during the extrapolation of K_{St} values for a given dust with varying σ_D.

Many natural and industrial dusts present a wide particle size distribution (high σ_D). However, most of the experimental and theoretical combustion studies are carried out with samples of low σ_D. In addition, it is difficult to compare experimental data from different researchers when the results are reported in relation to different definitions of average particle size. In order to understand the effect of σ_D on dust explosion hazards, the present analysis was restricted to aluminum dust samples.

Aluminum dust has several important production methods and applications [174]. For instance, aluminum dust can be used to improve the optical properties of pigments [12, 175], increase the fire rates of chromium (Cr) production [174], and

enhance the combustion and reactivity in propellants [14, 176]. Aluminum dust with low σ_D has been used to study several combustion parameters, such as burning velocity [77, 177], ignition temperature [177], combustion [176, 178], and ignition time [179]. Given that aluminum dust has been involved in devastating explosion accidents [1, 125, 180, 181], several investigations have been conducted to analyze the effect of particle size on explosion hazards parameters such as P_{max}, K_{St} and *MIE* [125, 182, 183]. These combustion parameters are very sensitive to the variation of particle size [19, 99, 124, 128, 184]. Huang *et al.,* [131] reported that the aluminum dust laminar flame speed is affected by the fine particle concentration within the mixture. Therefore, for a dust at a given particle diameter, the values of P_{max} and K_{St} will be affected by a systematic variation of the small and large particle size fraction contained in the mixture (*i.e.,* different σ_D).

This study explores the effect of aluminum dust size polydispersity on the dust hazard parameters such as P_{max}, K_{St} and *MIE*. Aluminum samples of similar D_{50} but varying σ_D were prepared by mixing commercially available samples of different D_{50} and narrow size distributions. The original samples and their mixtures were tested in a 36 L dust explosion vessel and a MIKE3 apparatus. The time span to reach the maximum rate of pressure rise (τ) was calculated from the pressure time curves obtained in the 36 L vessel. τ values give insights of the effect of D_{50}, σ_D and dust concentration on the velocity of the flame propagation of the tested samples. Additionally, the laminar burning velocity (S_L) of the original samples was calculated using experimental parameters obtained in the 36 L vessel such as pressure, time, and rate of pressure rise at

the inflection point. The results obtained in this research demonstrate the importance of σ_D on aluminum dust explosion hazard characterization.

4.3. Methodology

4.3.1. Determination of P_{max}, K_{St}, τ and MIE values of aluminum dust

The methodology used to measure P_{max} and K_{St} has been previously described in section 3.5. Figure 5 (Chapter II) shows how $(dP/dt)_{ex}$, P_{ex}, and τ are obtained during a dust explosion for a specific dust concentration. To determine the *MIE* values of the aluminum dust samples, a MIKE3 equipment was used (Figure 20).

Figure 20. MIKE3 equipment.

The operation mode is based on the ASTM standard E2019-03 [59]. In a typical experiment, the sample is evenly distributed on the bottom of the tube, around a mushroom shaped nozzle. A blast of compressed air disperses the dust into a 1.2-L

cylindrical glass vessel. The cloud is then ignited by an electric spark. The spark is generated between two tungsten electrodes separated by a 6-mm gap that are located at one-third of the tube height. Tests were performed using an inductance of 1 mH and an ignition delay time of 120 ms. The *MIE* values were found by varying the dust cloud concentration between 60 to 3,000 g/m^3 and varying the ignition energy between 1 to 1,000 mJ. The ignition was determined by visual observation.

In the MIKE3 equipment, two levels of energy are identified, E1 and E2. E1 corresponds to the lowest energy level where explosion is observed, whereas E2 represents the highest energy level where no explosion is obtained in ten consecutive tests. The *MIE* value is calculated based on the probability of ignition, using the following expression [185]:

$$MIE = 10 \text{ ^ } \left(log\ E2 - I\langle E2\rangle \cdot \left(\frac{log\ E2 - log\ E1}{(NI+I)\langle E2\rangle + 1} \right) \right) \quad \textbf{(28)}$$

where I is the number of tests with ignition and NI is the number of tests with no ignition. $I\langle E2\rangle$ is the number of tests having ignition at E2 and $(NI + I)\langle E2\rangle$ is the total number of tests at E2. In our experiment, a minimum of 5 tests at different concentrations were performed at the energy level E2.

In the literature, the *MIE* values are used to categorize the ignition sensitivity of the sample. Dust is considered extremely, very, and fairly sensitive to electrostatic ignition for *MIE* values below 3 mJ, between 3 to 30 mJ, and between 30 to 1000 mJ, respectively[186].

4.3.2. Aluminum sample preparation and size characterization

In order to understand the effect of σ_D at a fixed D_{50} during a dust explosion, aluminum samples with the following mean diameters: 2, 5, 9, 15, 20, 25, and 30 μm were systematically combined. The mixtures were prepared by adding each component in a jar filled to about two-thirds capacity and manually blending each sample for 30 minutes using a *figure-8-track* to ensure self-mixed samples. Original samples and the resulting mixtures were stored under a nitrogen atmosphere to prevent aluminum oxidation.

The particle size distribution of the original samples was determined using a Mastersizer 3000 analyzer (Malvern Inc, Worcestershire, UK) and a LS 13 320 Coulter multi-wavelength laser diffraction particle size analyzer (Beckman Coulter, Inc. Brea, CA). The laser diffraction measurement was performed in wet-mode using water as the suspension medium. Micro 90® manufactured by International Products Corporation was used as a surfactant. Aluminum *PSD* results from both instruments were in very good agreement. The measurements provide the size distribution on a volume (or mass) basis and the statistical diameters, D_{10}, D_{50}, and D_{90}. D_{xx} refers to the particle size for which xx% of the particles by weight are finer. Table 8 summarizes the particle size characterization of these samples.

Table 8. Particle size characterization of the original aluminum samples using a Malvern laser diffractometer.

Original sample mean diameter (μm)	D_{10} (μm)	D_{50} (μm)	D_{90} (μm)	σ_D	Specific surface area (m^2/g)
2	0.98	2.32	4.62	1.57	4.39
5	2.66	4.57	7.49	1.06	2.01
9	6.03	8.84	12.96	0.78	0.71
15	9.41	14.90	23.55	0.95	0.43
20	12.70	19.98	31.31	0.93	0.32
25	15.46	24.67	39.08	0.95	0.26
30	18.15	30.42	52.77	1.14	0.21

Table 9. shows the corresponding mass fractions of the original aluminum samples used to prepare each of the five blends having similar D_{50} and varying σ_D.

The particle size polydispersity (σ_D) characterized by the span of the size distribution is calculated using the following expression:

$$\sigma_D = \frac{D_{90} - D_{10}}{D_{50}} \quad \textbf{(29)}$$

The *PSD* of the resulting mixtures was calculated by adding the initial size distributions in accordance to their contributions or mass fractions. The aluminum dust density is the same in all samples. The calculated size distributions shown in Figure 21 were also verified experimentally with the Beckman Coulter analyzer described above. The calculated and experimentally measured *PSD* presented excellent agreement.

Table 9. Mass fractions of initial aluminum samples used to generate five blends at similar particle mean diameter (D_{50}) and varying size polydispersity (σ_D).

Blend	Mass fraction							D_{10} (µm)	D_{50} (µm)	D_{90} (µm)	σ_D
	2 (µm)	5 (µm)	9 (µm)	15 (µm)	20 (µm)	25 (µm)	30 (µm)				
1	-	-	-	1	-	-	-	9.41	14.90	23.55	0.95
2	-	-	0.200	0.600	0.200	-	-	8.07	14.32	24.83	1.17
3	-	0.125	0.125	0.500	0.125	0.125	-	5.79	14.26	26.85	1.48
4	0.100	0.100	0.100	0.400	0.100	0.100	0.100	3.44	14.21	30.00	1.87
5	0.333	-	-	0.333	-	-	0.333	1.68	14.55	38.23	2.51

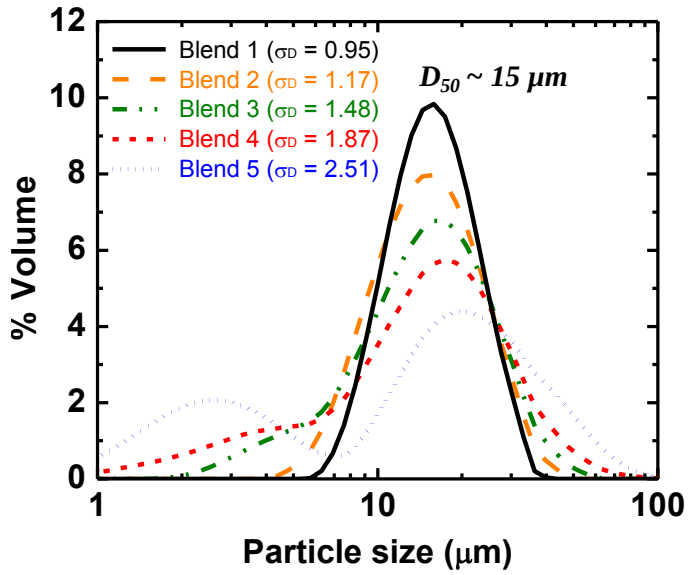

Figure 21. Summary of particle size distributions for mixtures having D_{50} of 15 µm and varying σ_D . Blend 1, 2, 3, 4, and 5 correspond to polydispersities of 0.95, 1.17, 1.48, 1.87, and 2.51, respectively.

Micrographs of aluminum mixtures were obtained using scanning electron microscopy (SEM-JEOL JSM-7500F). Figure 22 shows the SEM images of the resulting mixtures. As observed from the micrographs, polydispersity increases from blend 1 to blend 5. Blend 1 (σ_D = 0.95) presents the highest homogeneity in particle size, while blend 5 (σ_D = 2.51) is the most heterogeneous in particle size.

4.4. Results and discussion

4.4.1. Effect of D_{50} on P_{max} and K_{St} values of aluminum dust at low σ_D

In order to analyze the effect of D_{50} on P_m and $(dP/dt)_{ex}V^{1/3}$ at a relatively low polydispersity, the original samples listed in Table 8 were tested using the 36 L dust explosion vessel. Figure 23 shows the experimental explosion hazard parameters of the original samples as a function of aluminum dust concentration. In general, finer particles (D_{50} = 2 μm) produced a higher P_m and $(dP/dt)_{ex}V^{1/3}$. The P_{max} and K_{St} values obtained at the optimum concentrations can be found in Table 10. In agreement with Dufaud *et al.,* [124, 187], P_{max} and K_{St} values monotonically increase as D_{50} reduces. These results confirm that the combustion reaction is directly related to the total surface-area available.

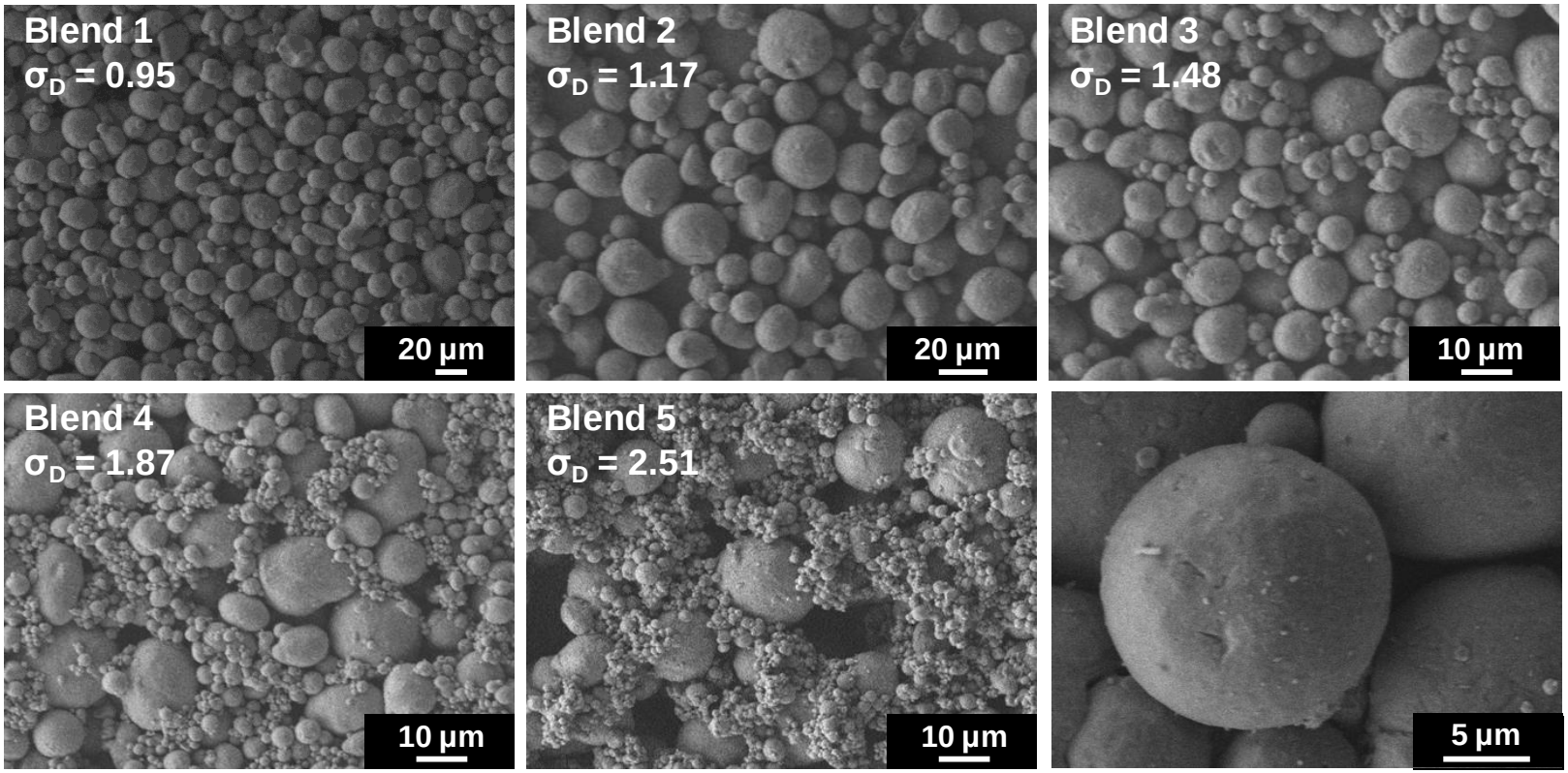

Figure 22. SEM micrographs of aluminum samples having D_{50} of 15 µm and varying σ_D. Blend 1, 2, 3, 4, and 5 correspond to σ_D of 0.95, 1.17, 1.48, 1.87, and 2.51, respectively. Right bottom micrograph corresponds to a typical aluminum particle having a diameter of around 15 µm.

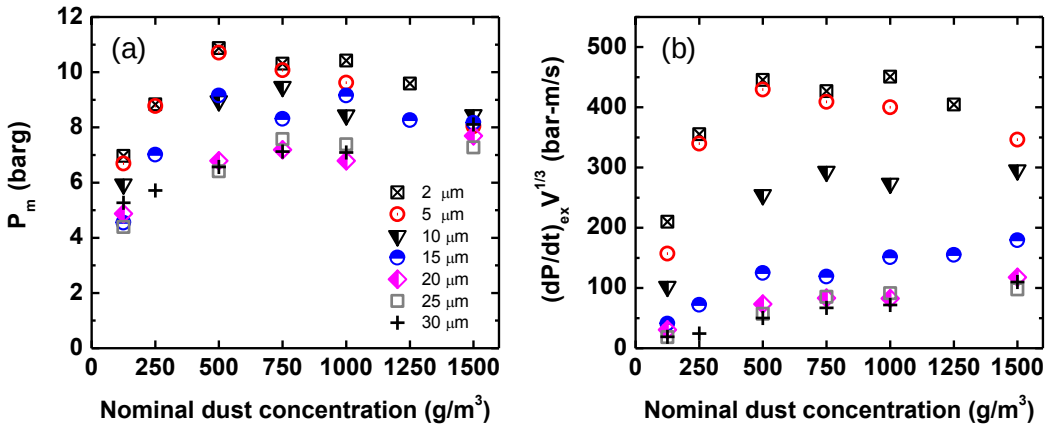

Figure 23. Experimental results of the original aluminum dust samples having D_{50} of 2, 5, 10, 15, 20, 25, and 30 μm and σ_D of 1.57, 1.06, 0.78, 0.95, 0.93, 0.95, and 1.14, respectively. (a) P_m and (b) $(dP/dt)_{ex}V^{1/3}$ *versus* nominal dust concentration.

Table 10. Summary of P_{max} and K_{St} values of original aluminum dust samples

Original sample D_{50} (μm)	P_{max} (barg)	K_{St} (bar-m/s)
2	10.9	451
5	10.7	430
9	9.5	296
15	9.2	179
20	7.7	118
25	7.6	98
30	8.1	110

4.4.2. Effect of σ_D on P_{max} and K_{St} values of aluminum dust at a fixed D_{50}

To study the effect of σ_D on P_m and $(dP/dt)_{ex}V^{1/3}$ at a fixed D_{50} (~15 µm), the blended samples previously described in Table 9 were tested following the exact same procedure used with original samples. Figure 24 shows experimental results of P_m and $(dP/dt)_{ex}V^{1/3}$ for dust explosion tests performed at different dust concentrations.

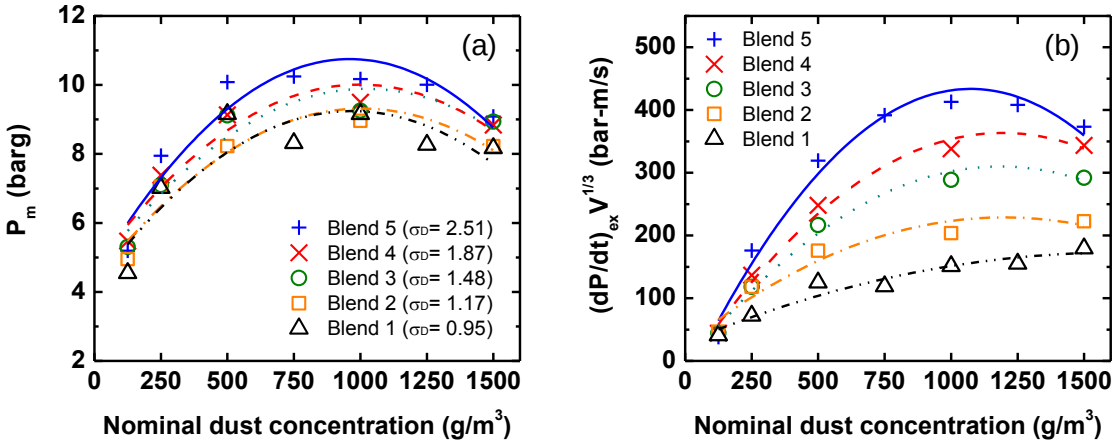

Figure 24. Experimental results of aluminum blends having D_{50} of 15 µm at varying σ_D, using a 36 L dust explosion vessel. Blends 1, 2, 3, 4, and 5 correspond to σ_D of 0.95, 1.17, 1.48, 1.87, and 2.51, respectively. (a) P_m and (b) $(dP/dt)_{ex}\cdot V^{1/3}$ values

Interestingly, although the samples are characterized by a similar D_{50}, the aluminum explosibility increases along with σ_D. Significant variations on $(dP/dt)_{ex}V^{1/3}$ values were observed, which reveal that the effect of σ_D on the combustion reaction kinetics cannot be neglected (Figure 24b). This gradual increase in P_m and $(dP/dt)_{ex}V^{1/3}$

values is attributed to the higher fraction of fine particles suspended in the cloud. The fine aluminum particles presented in the dust cloud increases the total surface area available for combustion to occur, thus increasing the combustion reaction rate [188]. Table 11 contains P_{max} and K_{St} values obtained at the optimum concentrations for the different blends at varying σ_D. Experimentally, the sample with the lowest polydispersity (blend 1, $\sigma_D \sim 0.95$) resulted in a K_{St} of 179 bar-m/s, whereas the sample with the highest polydispersity (blend 5, $\sigma_D \sim 2.51$) presented a K_{St} value of 413 bar-m/s. Thus, risk assessment evaluations based on hazards associated to samples with low σ_D, can lead to significant underestimations.

In comparison to large-sized particles, it is well known that small ones exhibit lower ignition temperature [177, 189], lower heat diffusion time [112], and faster burning rate [131, 177]. Hence, particles of reduced diameters possess more efficient flame propagation. It is generally assumed that micro-sized aluminum particles are covered by an alumina (Al_2O_3) shell. This alumina layer can break by melting at 2,350 K or via core-thermal expansion [77]. During shell-breaking, the aluminum particles can easily ignite. The smaller particles present a lower ignition temperature due to their large specific surface area that improves the heat transfer to the aluminum core [190]. Once the ignition temperature is reached, the combustion process initiates and the produced heat is transferred to the neighboring-unburned particles [112]. The efficiency of this heat transference can be favored by a shorter inter-particle spacing (*i.e.,* high nominal dust concentration) [112]. Flame propagation continues until the heat released from the combustion process is not able to maintain the ignition temperature of the

unburned particles [112]. Thus, in our experiments we are expecting that the fraction of smaller particles added into the dust samples will ignite at lower temperatures and facilitate the heat transfer to the larger particles.

Table 11. Summary of P_{max} and K_{St} values of blended aluminum dust samples

Blend	P_{max} (barg)	K_{St} (bar-m/s)
1	9.15	179
2	8.96	223
3	9.25	292
4	9.50	344
5	10.25	413

To quantitatively relate the explosibility parameters with size polydispersity, P_m and $(dP/dt)_{ex} \cdot V^{1/3}$ values were plotted as a function of σ_D for each dust concentration, as shown in Figure 25a and b, respectively. From Figure 25 the highest values were selected, which correspond to P_{max} and K_{st} (Table 11). From data interpolation, a linear relationship of P_{max} and K_{st} as a function of σ_D was obtained:

$$K_{St} = (52 \pm 24) + (149 \pm 14) \times \sigma_D \quad \textbf{(30)}$$

$$P_{max} = (8.2 \pm 0.3) + (0.76 \pm 0.15) \times \sigma_D \quad \textbf{(31)}$$

Equations 30 and 31 are valid for aluminum dust of D_{50} = 15 μm in a range of polydispersity between 0.95 and 2.5. In general, a monotonic growth of the explosion severity parameters, P_{max} and K_{St}, along with σ_D was observed. The values of K_{St} during

the dust explosion tests presented a stronger effect from σ_D compared to P_{max}. The slope of these correlations is given by the effective concentration of the fine particles in the cloud, which might be affected by the particles dispersion inside the dust explosion vessel. Liu *et al.,* [7] reported a strong powder flowability dependency on particle size and *PSD*. The y-intercept of these correlations might be influenced by the particle median mean diameter, surface chemistry, and chemical composition. It is worth mentioning that these correlations should not be extrapolated for mixtures outside the stated polydispersity range ($0.95 \leq \sigma_D \leq 2.5$). Additional factors such as particle agglomeration can reduce their effective surface area within the dust cloud, leading to unexpected reductions on the explosion severity. For instance, Bouillard *et al.,* [137] reported that 200 and 100 nm aluminum particles presented K_{st} values of 673 and 362 bar-m/s, respectively. This surprising reduction on K_{st} was attributed to a higher tendency of the 100 nm particles to aggregate. Interestingly, Figure 25b shows that at low aluminum dust concentrations (< 250 g/m^3), $(dP/dt)_{max} \cdot V^{1/3}$ was not significantly affected by σ_D. This effect might be explained by the large inter-particle spacing found at low dust concentrations. Although reduced diameter aluminum particles burn at lower temperatures, the heat is dissipated into the air instead of being transferred to the neighbor particles. On the other hand, as dust concentration approaches an *optimum value* (~ 1,000 g/m^3), the inter-particle spacing is reduced and the effect of size polydispersity becomes more significant (*i.e.,* the fine particles concentration increases). Therefore, the role played by the fine particles facilitating flame propagation within the dust cloud is more appreciable at higher nominal dust concentrations.

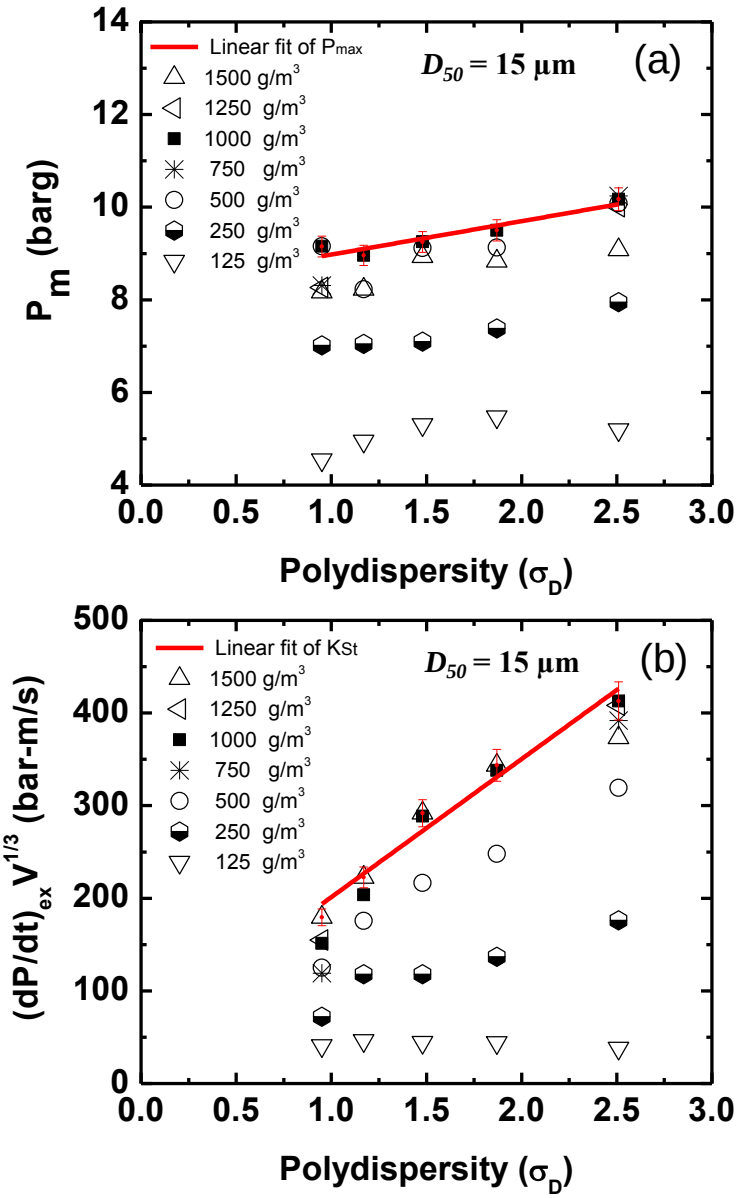

Figure 25. Experimental results plotted as a function of aluminum dust polydispersity. (a) P_m values. The solid line is the linear fit of P_{max} values, P_{max} = (8.2 ± 0.3) + (0.76 ± 0.15) × σ_D. (b) $(dP/dt)_{ex} \cdot V^{1/3}$ values. The solid line represents the linear fit of K_{St} values, K_{St} = (52 ± 24) + (149 ± 14) × σ_D.

4.4.3. Effect of D_{50} on MIE values of aluminum dust samples at low σ_D

To evaluate the effect of D_{50} on *MIE* values, the original samples listed in Table 8 were tested in the MIKE3 equipment. The resulting energy levels (E1 and E2) with the corresponding observations of ignition and not ignition at varying dust concentrations are shown in Figure 26. The MIE values estimated from equation 28 are summarized in Table 12. In agreement with previous experimental work [125, 129], ignition sensitivity systematically increases (reduction of MIE values) as particle size decreases.

Table 12. Summary of *MIE* values of original aluminum dust samples

Original sample D_{50} (μm)	*MIE* (mJ)
2	4
5	5
9	21
15	38
20	120
25	120
30	150

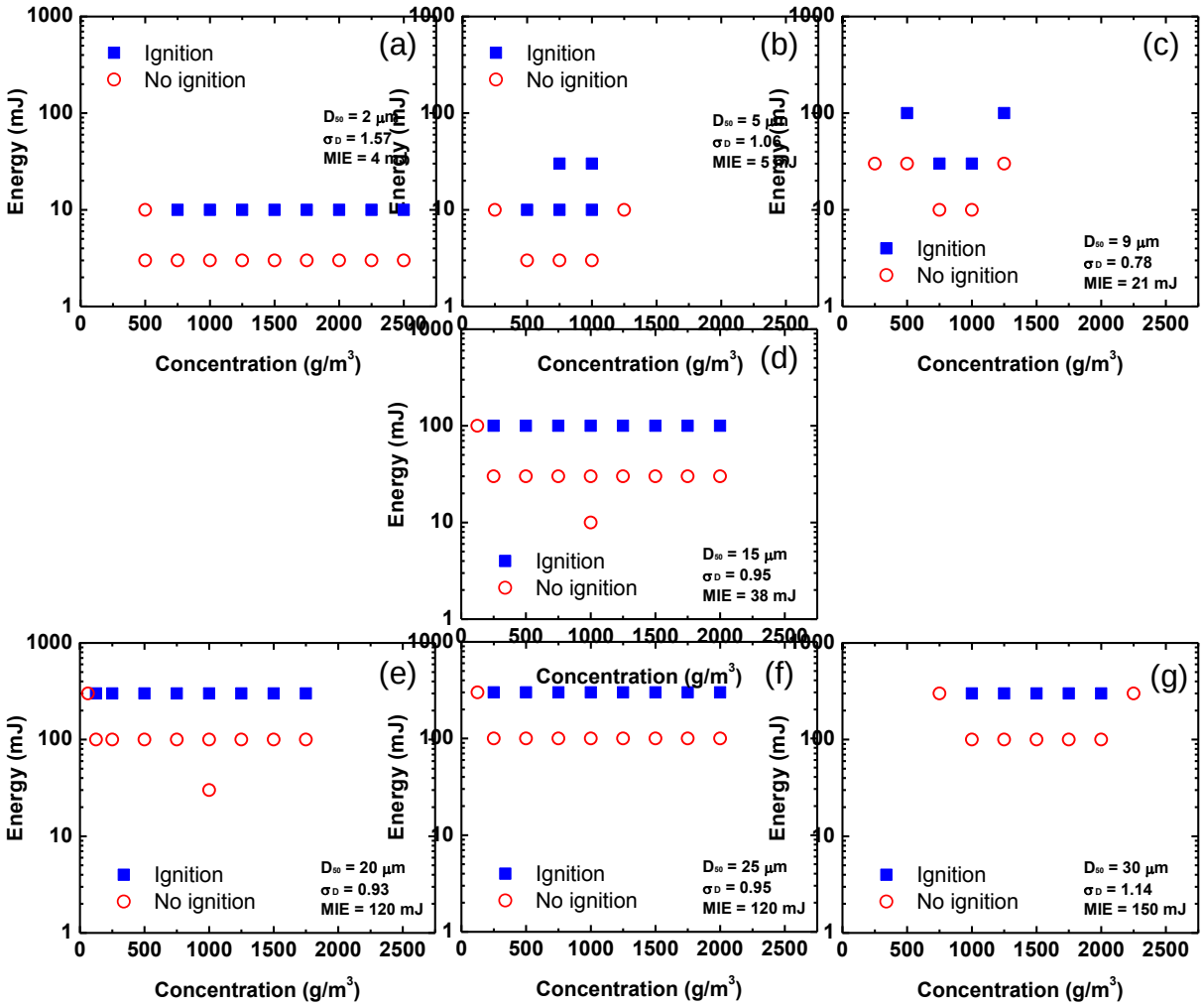

Figure 26. Determination of the *MIE* values of aluminum dust samples with narrow size distribution and varying D_{50}

4.4.4. Effects of σ_D on MIE values of aluminum dust at a fixed D_{50}

In order to evaluate the effect of σ_D on the ignition process of aluminum dust clouds, the *MIE* values of blends 1 and 5 were tested in a MIKE3 equipment. In this apparatus, the ignition of the fuel-air mixture occurs when the discharged energy is able to reach the minimum ignition temperature of the particles located between the electrodes gap. The flame produced propagates through the dust cloud [1] (see Section 4.2.1). From these experiments, it was observed that σ_D not only affects P_{max} and K_{St}, but also the ignition sensitivity (*MIE*). Figure 27 shows the *MIE* values as a function of σ_D values.

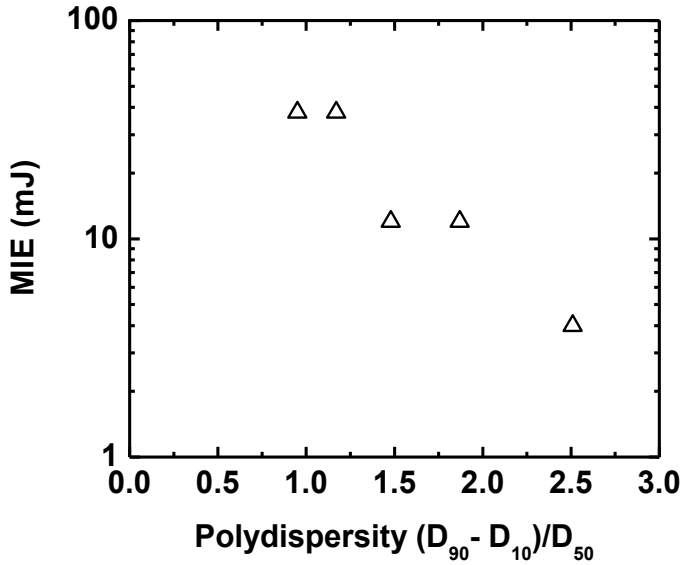

Figure 27. *MIE* values of aluminum dust samples with D_{50} of 15 µm and varying size polydispersity (σ_D)

The *MIE* values decrease from 41 mJ to 4.1 mJ when σ_D increases from 0.95 to 2.51. This dramatic reduction on the *MIE* value occurs due to the ignition temperatures differences of the particles forming the cloud. The ignition temperature for particles between 1 to 100 μm can vary appro imately from 1,700 to 2,200°C [177]. As a result, the blend with the highest σ_D (*i.e.,* largest percentage of 2 μm particles) ignites easier.

4.4.5. Analysis of the explosibility characteristics versus D_{50}, $D_{4,3}$, and $D_{3,2}$

K_{St}, P_{max} and *MIE* values were also analyzed in terms of different definitions of particle size. Figure 28 shows K_{St}, P_{max}, and *MIE* values plotted as a function of median mean diameter (D_{50}), and volume- ($D_{4,3}$) and surface- ($D_{3,2}$) weighted mean diameters, respectively. In the case of the original samples (low σ_D), P_{max} and K_{St} values presented a strong influence with D_{50}, $D_{4,3}$, and $D_{3,2}$. However, the blended samples did not present a coherent relationship with P_{max} and K_{St} along with D_{50} and $D_{4,3}$. This observation was specially noticed in samples having σ_D values larger than 1.5 (Figure 28 a, b, d and e). On the other hand, Figure 28c and f show that regardless of the σ_D value, $D_{3,2}$ is more adequately related to the hazard potential of the material.

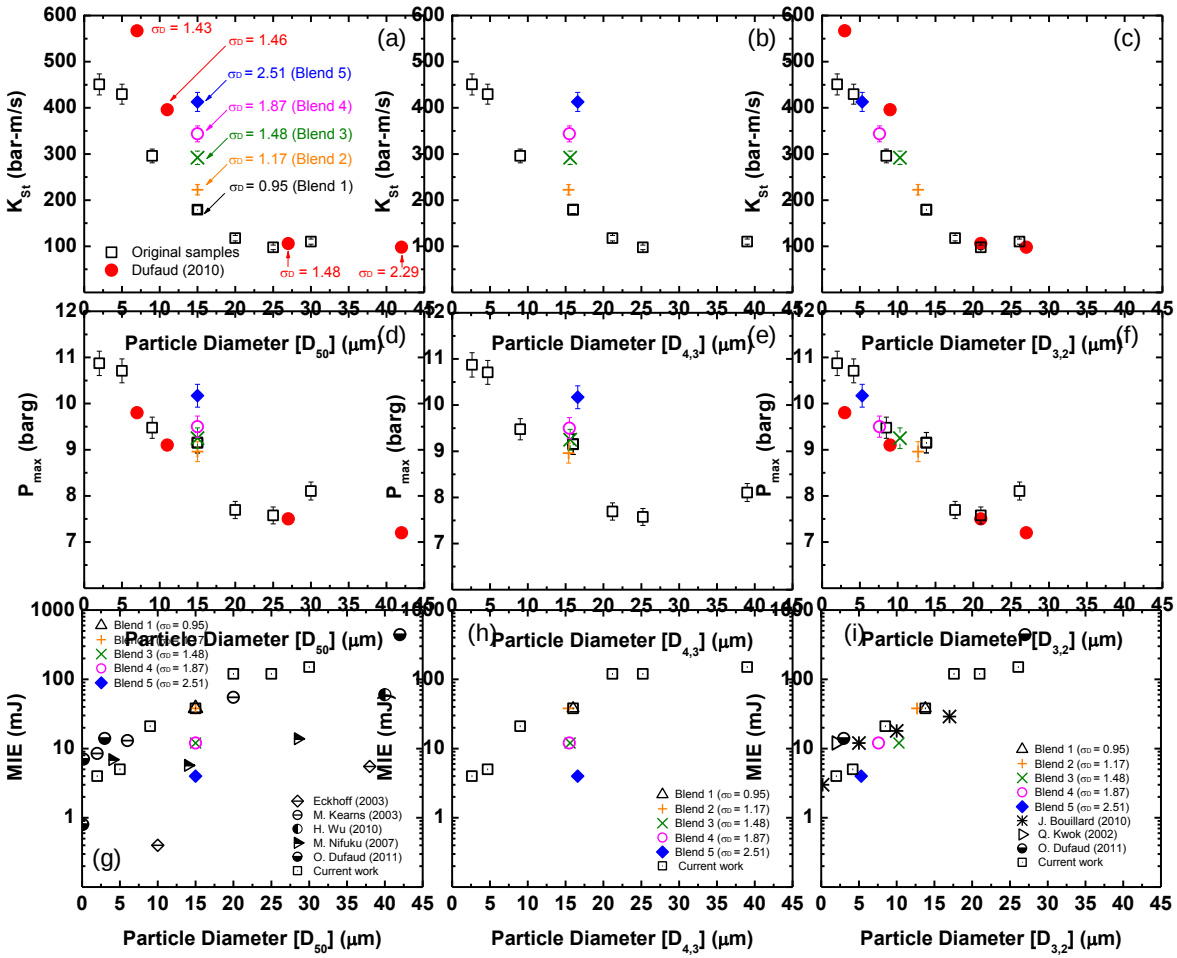

Figure 28. Explosion characteristics of aluminum dust in relation to different definitions of average particle size. (a), (b), and (c) K_{St} values. (d), (e) and (f) for P_{max}. (g), (h) and (i) *MIE* values.

Similar conclusions were obtained from *MIE* results (Figure 28g, h and i). For instance, in Figure 28g, *MIE* values are not properly correlated with the sample particle size. A large data scattering is obtained between D_{50}, $D_{4,3}$, and the sample ignition sensitivity, while Figure 28i clearly shows an increase on MIE values with particle size. Hence, the surface-weighted average diameter ($D_{3,2}$) provides the best description of the particle size distribution. This confirms that the combustion process is essentially a surface-area-related process. Given that D_{50} does not properly describe the *PSD* of a combustible dust, the explosion hazard characterization of these types of materials should be reported in terms of $D_{3,2}$ and σ_D.

4.4.6. The effect of D_{50} and σ_D on the flame propagation velocity

In this study, two parameters were used to compare the velocity of the flame propagation on the dust samples: the time span to reach the maximum rate of pressure rise (τ, Figure 5) and the burning velocity (S_L). τ was measured during each dust explosion test conducted with original and blend samples. S_L was exclusively calculated on the original samples.

4.4.6.1. C c u f τ for original and blended samples

Figure 29a and b show the calculated τ values as a function of nominal dust concentration of original and blend samples, respectively. τ values give insights of the effect of the particle size, σ_D and concentration on the velocity of the flame propagation. For the original samples, Figure 29a shows a monotonic reduction of τ as D_{50} decreased and as dust concentration increased. In the case of blended samples, τ reduced as σ_D and

concentration incremented as shown in Figure 29b. Interestingly, τ presents a stronger dependence on concentration at relatively high σ_D. For instance, a dramatic reduction on τ was observed on blend 5, where τ dropped from 37.3 to 9.7 ms as the dust concentration incremented from 125 to 1,500 g/m^3. This effect is explained from the role played by the fine particles on the combustion process, which is enhanced by the reduction of the inter-particle spacing.

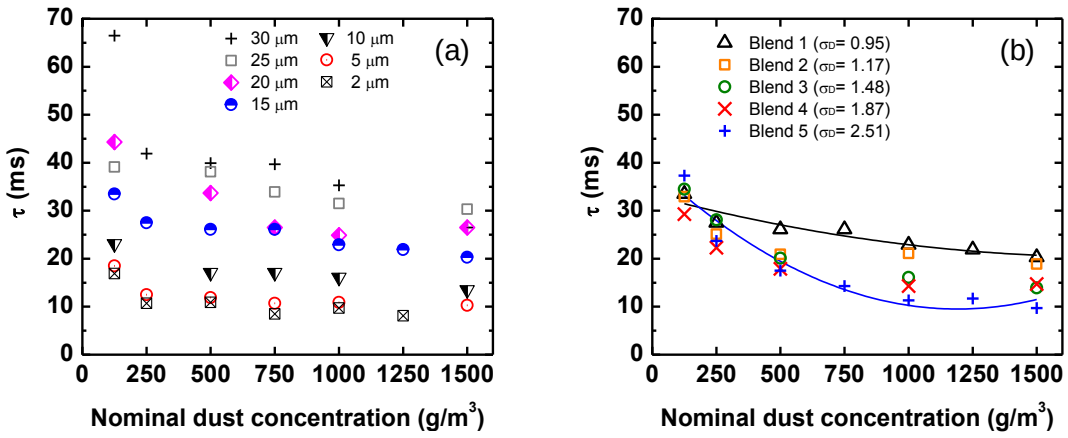

Figure 29. Calculated τ values as a function of nominal dust concentration. (a) Original dust samples having D_{50} of 2, 5, 10, 15, 20, 25, and 30 µm (b) Dust blends having D_{50} of 15 µm at varying σ_D.

4.4.6.2. Calculation of the laminar burning velocity

The turbulence burning velocity was estimated using experimental parameters such as pressure, time, and rate of pressure rise at the inflection point, the calculation procedure is described in section 2.2. Subsequently, the laminar burning velocity was

estimated using the combustion model reported by Skjold [81] (summarized in section 2.5). As previously mentioned, these correlations assume thin flame zones and homogeneous devolatilization of combustible dust [81]. This may limit their application for aluminum dust explosions due to their thicker flame in comparison to gas explosions [67]. However, Santhanam *et al.*, [67] estimated that aluminum flame zone is thick but still significantly small compared to the vessel diameter. Thus, the application of these correlations on aluminum dust explosions becomes acceptable [67]. Nevertheless, we only performed S_L calculations of original samples given that polydisperse samples present a thicker flame zone [131].

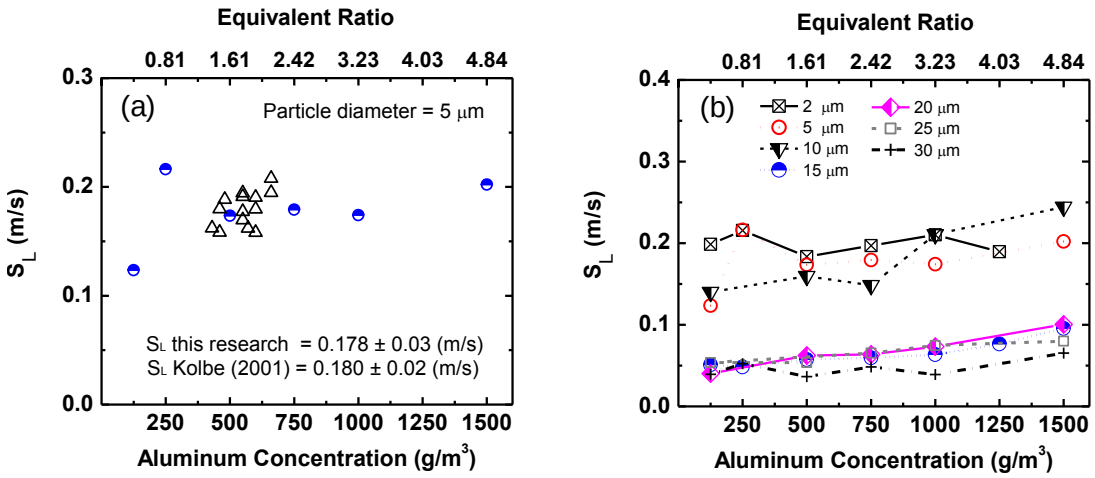

Figure 30. Aluminum dust laminar burning velocity (S_L) as a function of nominal dust concentration. (a) S_L at fixed D_{50} f 5 μ . (b) S_L at different aluminum dust particle size.

Figure 30a illustrates S_L calculations of aluminum dust having a D_{50} of 5 μm *versus* dust concentration and equivalent ratio. Equivalent ratio represents the aluminum dust concentration over the stoichiometric concentration (310 g/m^3)[191]. The stoichiometric aluminum dust concentration was calculated based on the following combustion reaction:

$$4Al + 3\left(O_2 + \frac{79}{21}N_2\right) \rightarrow 2Al_2O_3 + \frac{79}{7}N_2$$

Despite the assumptions that limit the applicability of these empirical correlations for aluminum dust samples [56], the estimated S_L presented very good agreement with the experimental results reported by Kolbe *et al.,* [76] using a Bunsen-type burner (Figure 30a). In both cases, S_L was approximately 0.2 m/s and little variations were observed at varying dust concentrations. S_L values presented in Figure 30a, were also in agreement with experimental data [77, 192] and theoretical values predicted by Huang *et al.,* [177] for equivalent ratios in the range of 0.7 to 1.

In addition, we calculated S_L values for aluminum dust at varying D_{50} (Figure 30b). Surprisingly, we found two different regimes below and above 10 μm. Aluminum dust of D_{50} between 15 to 30 μm presented S_L between 0.07 and 0.05 m/s. However, when the particle size is reduced below a critical value of 10 μm, a sudden shift of the burning velocity was observed. Similar behavior was observed by Huang *et al.,* [131]. They concluded that aluminum particles having a size above 10 μm, burn under a diffusion controlled process and the combustion process is not strongly dependent on the environmental temperature (*i.e.,* oxygen diffusion < aluminum reaction rate at the surface). In contrast, aluminum particles in a range between 130 nm to 10 μm, burn

under a kinetic controlled process (*i.e.,* oxygen diffusion > aluminum reaction rate at the surface) [131].

4.5. Conclusions

In conclusion, the effect of particle size polydispersity (σ_D) on the propagation of aluminum dust explosions was elucidated. A series of dust samples of varying σ_D at a fixed median mean diameter (D_{50} ~ 15 μm) were prepared by mi ing original samples having narrow size distributions. It was found that at constant D_{50}, the explosion hazards dramatically increased with σ_D. The sample with the lowest σ_D (0.95) resulted in a lower explosion hazard, with a P_{max} of 9.15 barg, a K_{St} value of 179 bar-m/s and an *MIE* of 41 mJ. While the sample with the highest σ_D (2.51) showed the greatest explosion hazard with a P_{max} of 10.25 barg, a K_{St} value of 413 bar-m/s and an *MIE* of 4.1 mJ. This effect was attributed to the concentration of aluminum particles of reduced diameter suspended in the dust cloud. In comparison with large-sized aluminum dust, fine particles not only ignite at lower temperatures but also combust more rapidly due to their extensive specific surface area. We also observed that $D_{3,2}$ exhibited the best correlation between particle size and the explosion parameters, P_{max}, K_{St} and *MIE*. Thus, the explosion hazards characterization of combustible dust should be reported in terms of $D_{3,2}$ and σ_D.

Finally, a simplified combustion model for dust explosions was utilized to estimate burning velocity (S_L) of the original aluminum samples. In agreement with previous experimental data and theoretical predictions, a sudden increase of S_L was observed when D_{50} was reduced below 10 μm.

It is expected that the methodology used here can be extended to other combustible metals such as titanium, magnesium, tungsten, and boron. Similar correlations can be applied to design proper explosion protection systems to prevent undesirable catastrophic events in the dust-handling industry.

CHAPTER V

INFLUENCE PARTICLE SIZE AND CRYSTALLINE LEVEL ON THE EFFICIENCY OF DUST EXPLOSION INHIBITORS

5.1. Synopsis

We introduce diammonium phosphate (DAP) and zirconium phosphate (α-ZrP) crystals as alternative dust explosion inhibitors. The influence of size and crystallinity on the efficiency of dust explosion inhibition was systematically studied. Particle size of DAP was manipulated by milling and sieving. The size and crystallinity of α-ZrP were tailored during its synthesis by adjusting the phosphoric acid (H_3PO_4) concentration and the reaction time [193, 194]. A common dust explosion suppressant, monoammonium phosphate (MAP), was utilized as reference. To evaluate the inhibitor efficiency of each material, we analyzed the thermal stability of mixtures containing cornstarch and DAP/α-ZrP/MAP, using thermo-gravimetric analysis (TGA) and differential scanning calorimeter (DSC). In addition, the dust explosion severity (*i.e.,* maximum pressure (P_{max}) and maximum rate of pressure rise ($(dP/dt)_{max}$)) of these mixtures was obtained by performing dust explosion tests using a 36 L vessel. The experimental results show that α-ZrP provides the highest thermal stability but the lowest rate of heat absorption of the mixtures. On the other hand, DAP provides a lower thermal stability in comparison to α-ZrP and MAP, but exhibits a remarkable rate of energy absorption during its decomposition reaction. In general, the efficiency of dust inhibitors increased by decreasing particle size. Particularly, DAP and MAP presented a critical diameter (*i.e.,*

128 μm), where the inhibitor efficiency was enhanced. However, the performance of α-ZrP as an inhibitor was not considerably affected by the variation of particle size and crystalline level. Finally, a semi-empirical model was developed to identify the factors dominating the reduction of cornstarch explosion severity. In agreement with aforementioned results, the simplified model presents a critical diameter below which the inhibitor efficiency is significantly improved.

5.2. Introduction

Combination of additives with combustible materials is a common strategy used to prevent or reduce the consequences of dust explosions. The additive can be premixed with the combustible dust to prevent or inhibit the explosion, but it can also be injected at early stages of the explosion to suppress or reduce the explosion consequences [28]. These additives have two typical mechanisms to impede the combustion process, a chemical mechanism consisting on chemical interference of the combustion reaction and a physical mechanism centered on the reduction volatiles production. A variety of materials is indifferently used for both suppression and inhibition, although their functional distinction must be considered during the additive design and synthesis [28]. Nevertheless, research advances in areas such as inerting, suppression and extinction are also useful to understand parameters affecting the inhibitors behavior.

Several experimental and theoretical studies have been conducted to investigate the factors affecting the efficiency of dust explosion protection additives [30, 195-197]. The increase of suppressant specific heat capacity, thermal conductivity [25], and the rate of heat absorption [198] improve the suppressant performance. The first two

parameters are closely related to the chemical composition, and the latter is more dependent on the suppressant particle size [198, 199]. As suppressant size decreases, the suppressant decomposition and rate of heat absorption increases, which limits the combustible dust de-volatilization and the amount of flammable material able to participate in the combustion reaction [157, 200]. Dastidar *et al.,* [157] and Kui *et al.,*[201] demonstrated that less additive is required to control the explosion as additive surface area increases. Testing thirteen different inorganic salts as gas explosion suppressants, Dolan and Dempster [202] reported that the surface area is one of the most important parameters determining the suppression efficiency of the additives. Phosphates [156, 201] and carbonates [203] are typically used as fire and explosion suppressants. Previous studies suggest that these materials present a combination of chemical and physical inhibition mechanisms, heat absorption through their endothermic decomposition and termination of flame radicals [25, 156, 201]. Among all phosphates, monoammonium phosphate (MAP) has been widely studied as an explosion suppressant [25-30] and as an extinguishing agent due to its recognized ability to absorb heat through chemical decomposition [25, 204]. However, large quantities of inhibitor must to be added to effectively control the explosion [25, 26, 29, 201, 205]. In industrial applications, dust explosion control using less amount of suppressant is essential to reduce product contamination [25, 29].

In this research a systematic study is conducted to identify crucial parameters affecting the inhibitor efficiency, including particle size, mass load and crystalline level. The first two parameters were analyzed using mixtures of cornstarch as combustible dust

and diammonium phosphate (DAP, $(NH_4)_2HPO_4$) or monoammonium phosphate (MAP, $NH_4H_2PO_4$) as inhibitors. MAP was utilized as reference. The effect of particle size and crystalline level on the inhibitor efficiency was studied using samples containing cornstarch and zirconium phosphate (α-ZrP, $Zr(HPO_4)_2 \cdot H_2O$) as an alternative dust explosion inhibitor. Although DAP and α-ZrP have never been tested as explosion inhibitors, we believe that these materials have an enormous potential based on their ability to prevent thermal degradation of a variety of materials. For instance, DAP has been utilized to fabricate fire retardant composites [37, 206, 207]. DAP is characterized by a significant energy absorption resulting in the production of ammonia and water during chemical decomposition [38]. Additionally, DAP enhances char formation which is a deposit of solid combustion products that lower the combustion of the host material [206]. In the case of α-ZrP, this layered material has been utilized to enhance char formation [208, 209] and improve flame retardancy of polymer nanocomposites [34, 35, 209, 210] due to its outstanding thermal stability [33, 208, 211]. Particularly, α-ZrP is an interesting synthetic material, where the lateral size and crystalline level of the particles can be precisely manipulated by varying the synthesis conditions [193, 194]. In this work, the acid concentration and reaction time were varied to achieve crystals from nano- to micro- scale [193, 194]. It is expected that the results from this study can be a starting point in the design and synthesis of novel materials able to prevent and inhibit more efficiently dust explosions.

5.3. Effect of particle size and concentration on MAP and DAP effectiveness as explosion inhibitors

5.3.1. Samples preparation

The cornstarch sample $(C_6H_{10}O_5)_n$ used as combustible dust possess an average diameter of 15 μm. MAP (CAS# 7722-76-1) and DAP (CAS# 77783-28-0) were of ACS grade and purchased from EMD and AMRESCO, respectively. A series of inhibitor sizes were obtained by mechanical size reduction and sieving. The sieve' ranges and approximated average particle size are included in Table 13.

Table 13. Sieve range and inhibitor average diameter.

Sieve range (μm)	Average diameter (μm)
180 to 300	240
150 to 180	165
106 to 150	128
90 to 106	98
63 to 90	76.5
45 to 63	54

5.3.2. Evaluation of inhibitor efficiency

Three different techniques were used to quantitatively compare the role played by the inhibitor in the cornstarch combustion: DSC, TGA and dust explosion testing in a 36 L dust explosion vessel. DSC was used to estimate the onset of ignition temperature

and to determine the heat of the reaction. These parameters reveal the ability of the inhibitor to delay and reduce the heat released during cornstarch decomposition. TGA was utilized to determine the percentage of weight losses due to sample volatilization [206]. Finally, dust explosion tests in a 36 L vessel were carried out to obtain the pressure profile generated during the ignition of the dispersed dust within a confined space. The explosion severity of cornstarch samples with and without inhibitors are compared in terms of maximum pressure (P_{max}) and maximum rate of the pressure rise multiplied by the vessel volume ($(dP/dt)_{max}V^{1/3}$) achieved during the explosion tests. These three techniques are complementary, where the weight loss and heat of reaction obtained from TGA and DSC, respectively, are mainly affected by chemical composition and the ratio between cornstarch and inhibitor. The pressure profiles obtained from the 36 L vessel will elucidate the effect of inhibitor particle size and degree of dispersion within the dust cloud.

5.3.3. Thermo-gravimetric analysis (TGA)

The thermal stability of cornstarch/inhibitor mixtures was evaluated using thermo-gravimetric analysis (TGA). Figure 31a and b show the weight loss and derivative of weight loss percentage, respectively, as a function of temperature of samples containing cornstarch only and mixtures of cornstarch and each inhibitor in a ratio of 1:1. As observed, the thermal stability of cornstarch was significantly modified by the presence of each inhibitor. As indicated by Figure 31a and b, the cornstarch curve presents a sharp decrease of the weight percentage and a strong peak of the weight derivative at 300 ^{o}C, respectively.

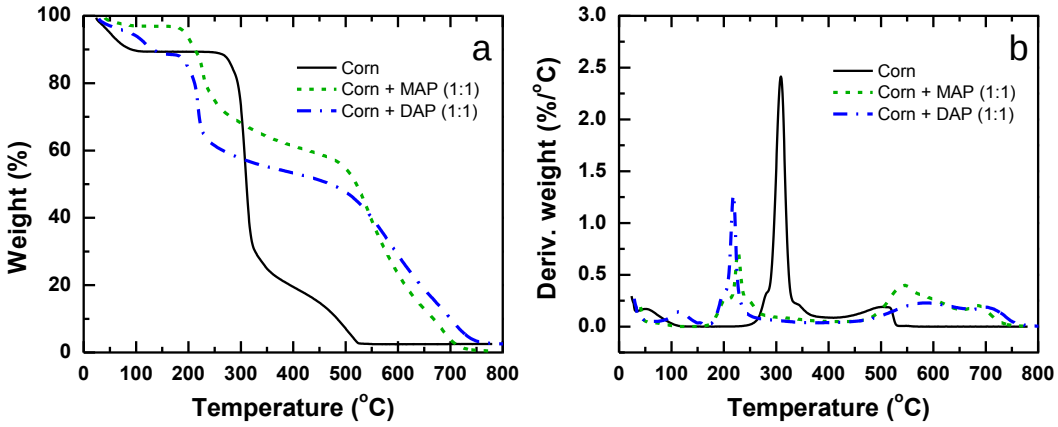

Figure 31. Thermo-gravimetric curves of cornstarch and cornstarch in the presence of explosion inhibitors using a heating rate 10°C min^{-1}(in air). (a) Weight percentage. (b) Derivatives to the weight percentage.

The initial weight losses of the mixtures are explained by the chemical decomposition of the inhibitors at temperatures below cornstarch devolatilization. For instance, in Figure 31a, the curve corresponding to the mixture containing DAP presents an initial weight loss below 160 °C due to ammonia release from the structure. The curve gradually decreases starting from a temperature of 209 °C. This observation can be explain from the following simplified reaction mechanism [212]:

$$(NH_4)_2HPO_4(s) \xrightarrow{160℃} NH_3(g) + NH_4H_2PO_4(s) \quad \textbf{(32)}$$

$$(NH_4)_2HPO_4(s) \xrightarrow{160℃} 2NH_3(g) + H_3PO_4(l) \quad \textbf{(33)}$$

$$NH_4H_2PO_4(s) \xrightarrow{209℃} NH_3(g) + H_3PO_4(l) \quad \textbf{(34)}$$

$$3H_3PO_4\ (l) \xrightarrow{160℃,\ 209℃} 2H_2O(g) + 2H_4P_2O_7(l) \quad \textbf{(35)}$$

$$2H_4P_2O_7\ (l) \xrightarrow{>209°C} 4H_2O(g) + P_4O_{10}(s) \quad \textbf{(36)}$$

In contrast to DAP, MAP chemical decomposition is accounted only on reactions 3 to 5, which indicates that MAP devolatilization initiates at 209 °C, producing ammonia and phosphoric acid [203], where the latter decomposes into P_4O_{10} and water [213]. The anticipated weight losses of the mixtures correspond to the endothermic decomposition of the inhibitor, which reduces the system temperature and prevents the combustible dust (*i.e.,* cornstarch) volatilization. This observation agrees with previous studies using MAP [214, 215] and DAP [212] as fire retardant materials. Additionally, decomposition products such as H_2O or NH_3 dilute the concentration of combustible gases which limit the combustion propagation [216]. Furthermore, the combustible material volatilization can be inhibited by inducing char formation, which reduces the mass and heat transference to the combustible surface and consequently the flame propagation [216, 217].

5.3.4. Differential scanning calorimeter (DSC)

The heat released during the decomposition of cornstarch, MAP and DAP was evaluated separately using differential scanning calorimeter (DSC, TA Instruments Q200). Mixtures containing cornstarch and MAP or DAP in a ratio of 1:1 were characterized to quantify the inhibitor efficiency absorbing heat during cornstarch chemical decomposition. Each sample of around 1 mg was placed into a capillary tube and maintained under cryogenic conditions during flame sealing of the tube to prevent chemical variation of the sample [218]. This sealed holder allows testing under a nitrogen atmosphere and prevents the escape of volatile products [218]. The capillary

tube is able to withstand 21 MPa and provides higher temperature and enthalpy resolution [218, 219]. The equipment used was daily calibrated with indium (25.9 to 31.5 J/g). All samples were tested under a nitrogen atmosphere. The test procedure consists of temperature rise from 40 ^{o}C to 400 ^{o}C using a heating rate of 10 ^{o}C/min.

The DSC measures the energy input differences between the sample and a reference empty capillary as function of temperature [220]. From the DSC thermograms, exothermic and endothermic reactions are characterized by a positive and a negative peak in the heat flow axis, respectively. The area under the curve represents the total heat released or absorbed during the reactions. The results from the mixtures are normalized by the initial weight of cornstarch. The temperature where the exothermic reaction begins is indicated by the onset of exothermic reaction. This parameter was approximated as the intersection between the baseline and the tangent line of the curve.

The DSC thermograms of MAP and DAP under an inert atmosphere are shown in Figure 32 a and b, respectively. MAP exhibited a single endothermic peak of 221 J/g between 176 to 242 ^{o}C. This range indicates the temperature where the chemical acts as inhibitor material. Interestingly, DAP presented a wider temperature range between 159 to 325 ^{o}C and a remarkable heat absorption of 455 J/g. Later, DSC measurements to mixtures of cornstarch with MAP or DAP in a ratio of 1:1 were performed. As a reference, the thermogram of pure cornstarch was obtained. As shown in Figure 33, MAP and DAP affected significantly the total heat released during cornstarch

decomposition. The reaction heat and the onset temperature of the mixtures are listed in Table 14.

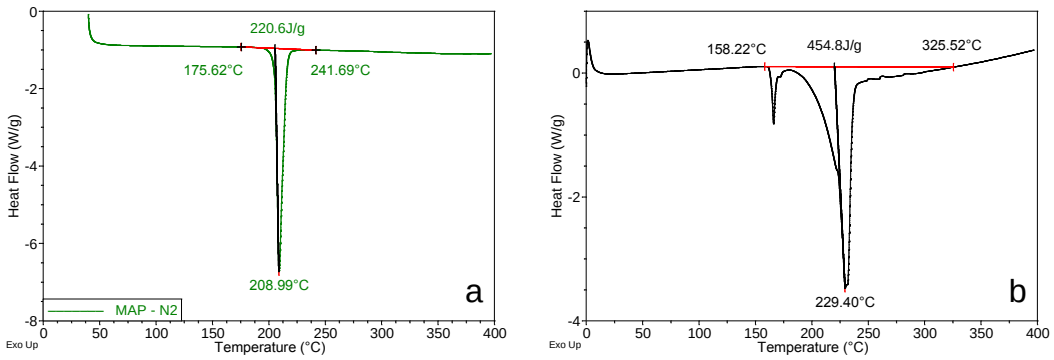

Figure 32. DSC thermograms of inhibitors under inert atmosphere. The temperature was rised from 40 °C to 400 °C, using a heating rate of 10 °C/min. (a) MAP and (b) DAP.

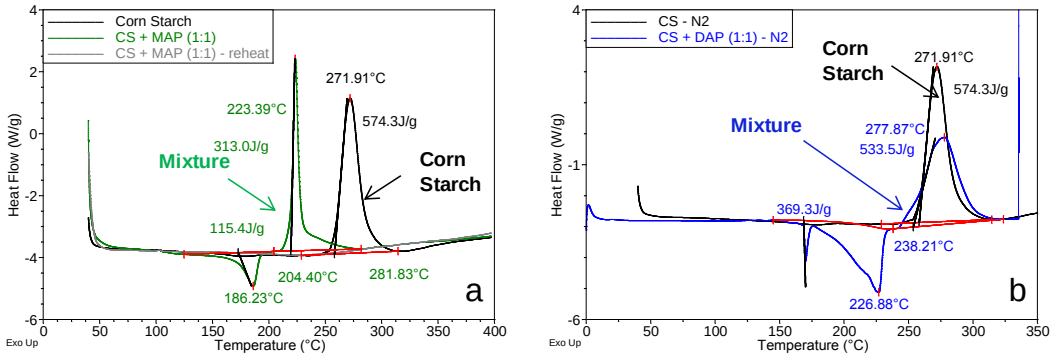

Figure 33. DSC thermograms of samples under inert atmosphere.The temperature was rise from 40 °C to 400 °C, using a heating rate of 10 °C/min. (a) Mixture of cornstarch and MAP (1:1). (b) Mixture of cornstarch and DAP (1:1). Results normalized based on cornstarch dust mass.

Table 14. Total heat released during mixtures decomposition measured using DSC.

Sample	Heat released (J/g of cornstarch)	Onset of exothermic reaction
Cornstarch (CS)	574	258.03 ^{o}C
CS + MAP	198	204.04 ^{o}C
CS + DAP	164	253.75 ^{o}C

The DSC thermograms confirm that the presence of MAP and DAP reduce the heat released during cornstarch decomposition by 65.5% and 71.5%, respectively. Both mixtures exhibited an endothermic peak from the initial heat absorbed by the inhibitor, followed by an exothermic peak corresponding to the heat released from the cornstarch decomposition. Surprisingly, the exothermic peak of the mixture containing MAP was shifted to lower temperatures in comparison to the pure cornstarch sample (Figure 33a). The onset of thermal decomposition was lower by about 25^{o}C. This anticipated initiation of the exothermic reaction suggests that MAP catalyzes the initiation of cornstarch combustion. Therefore, this material should be used as suppressant or extinguisher rather than as inertant to prevent the explosions. The variation on the reaction kinetics confirms the chemical inhibition mechanism undergone by MAP. Previous research with phosphorous containing materials as fire inhibitors have reported promoting effects attributed to the production of OH radicals by the reaction: $PO_2 + H_2O \rightarrow HPO_4 + OH$ [221]. In contrast, DAP did not affect the onset of the exothermic reaction and an outstanding inhibition efficiency is obtained.

5.3.5. Dust explosion tests in a 36 L vessel

A 36 L vessel is used to perform controlled dust explosions tests with mixtures of cornstarch and inhibitors at different weight ratios. The mixture is loaded into a dust container and dispersed inside the vessel through a rebound nozzle to create a uniform dust cloud. Subsequently, the mixture is ignited with a pair of 5 kJ chemical igniters. The pressure profile is recorded as a function of time to obtain the maximum pressure (P_{ex}) and maximum rate of pressure rise $(dP/dt)_{ex}$, during the explosion. P_{ex} is corrected into P_m to account the cooling effects of the vessel walls [58] and $(dP/dt)_{ex}$ is normalized by the vessel volume to obtain $(dP/dt)_{ex} \times V^{1/3}$. The test is repeated at different sample concentrations. The maximum pressure (P_{max}) and the deflagration index (K_{St}) are the maximum values of P_m and $(dP/dt)_{ex} \times V^{1/3}$ at varying dust concentrations. P_{max} and K_{St} are related to the thermodynamics and the kinetics of the combustion reaction, respectively. These parameters are widely used to quantify the severity of a dust explosion [1].

This procedure was used to measure the explosion severity of cornstarch. The samples were dried for 24 hours in a vacuum oven at 70^{o}C before the explosion tests. Experimental P_m and $(dP/dt)_{ex} \times V^{1/3}$ profiles as a function of nominal dust concentration are shown in Figure 34. Both, P_{max} (8.1± 0.2 barg) and K_{St} (179 ± 8 bar-m/s) values were achieved at a nominal cornstarch concentration of 750 g/m^3. Explosive characteristics of cornstarch samples were in agreement with experimental results reported by Skjold [173].

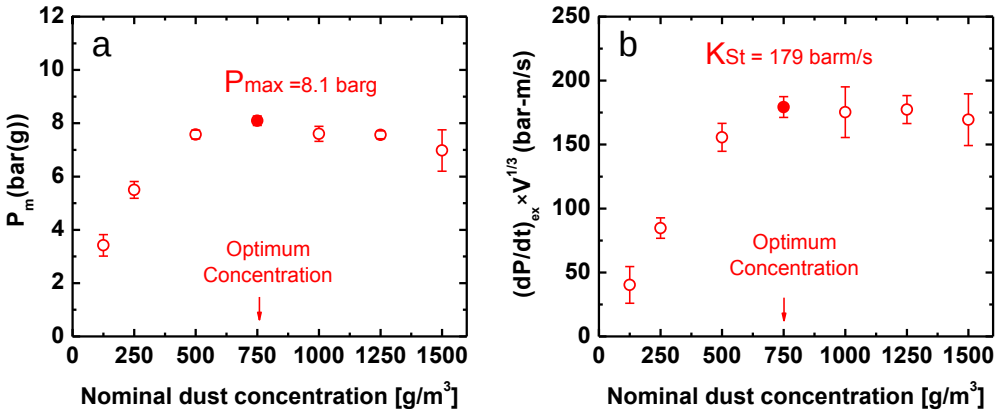

Figure 34. Explosive characteristics of cornstarch *vs.* dust concentrations. (a) P_m and (b) $(dP/dt)_{ex}V^{1/3}$.

To verify the effect of the inhibitors in reducing the cornstarch explosion severity, dust explosion tests were carried out using MAP and DAP at the optimal cornstarch concentration (750 g/m^3). We also analyzed the effect of inhibitor particle size and concentration. The experiments were performed using particles of MAP and DAP in size of 26, 54, 76.5, 98, 128, 165 and 240 µm (Table 13). Finally, we tested mixtures containing 27 g of cornstarch and MAP amounts of 9.5, 13.5 and 20.3 g, which correspond to 35, 50 or 75% of the total cornstarch weight. Similarly, we evaluated DAP in a mixture of 27 g of cornstarch and 13.5 g of DAP (50 wt%). The obtained values of P_{max} and K_{St} for the mixtures were plotted as a function of inhibitor particle size as shown in Figure 35.

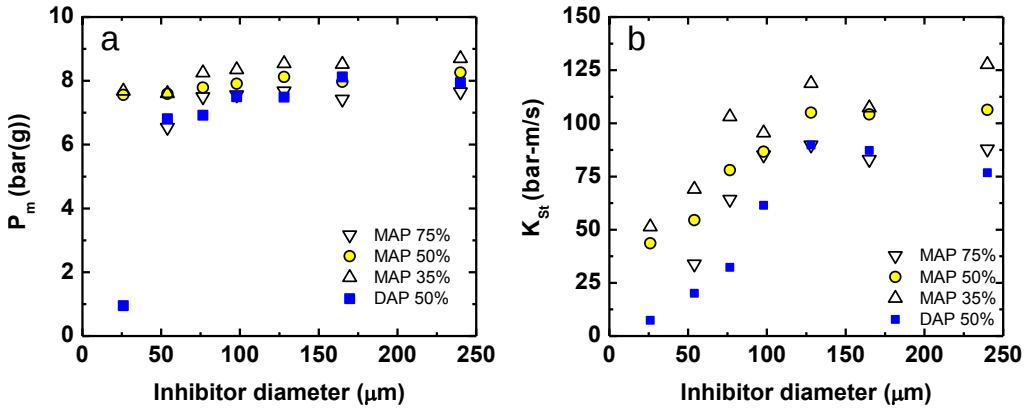

Figure 35. The effect of inhibitor on cornstarch explosion severity. MAP concentrations of 35%, 50% and 75 %, and DAP concentration of 50%. (a) P_{max} and (b) K_{St}.

The explosion characteristics of cornstarch decrease with the addition of an inhibitor in the mixture (Figure 35). Figure 35a shows that P_{max} values are not significantly affected by inhibitor size and concentration. However, the explosion was completely prevented (P_{max} < 2 bar) by adding 50 wt% of DAP of 25 μm. On the other hand, Figure 35b shows a dramatic reduction of K_{St} values by decreasing the inhibitor size and increasing inhibitor concentration. Samples containing 50 wt% of MAP between 128 to 240 μm presented roughly constant K_{St} values around 100 bar-m/s. This K_{St} values corresponds to a reduction of almost 45% percent of the pure cornstarch results. For MAP particle size lower than 128 μm, the K_{St} values were strongly dependent on inhibitor particle size. For instance, K_{St} values decreased from 105 to 44 bar-m/s as particle size changed from 128 to 26 μm. This effect might be attributed to a rapid MAP volatilization due to an increment on the particle surface area (*i.e.*, reduced

particle size). DAP exhibit similar trends before and after 128 μm. Although, DAP presented a remarkable inhibition efficiency compared to MAP. As observed in Figure 35b, the blue squared data points corresponding to DAP presented lower K_{St} values than MAP in the whole range of particle size. For instance, K_{St} of cornstarch (*i.e.,* 179 bar-m/s) is reduced to 65 and 30 bar-m/s using MAP and DAP of 75 μm, respectively. The results confirm that DAP controls more rapidly the explosion propagation even using lower concentrations than MAP.

The superior DAP efficiency can also be explained by the fuel dilution effect offered by prominent production of nonflammable gases. Horackect and Grabner [222], reported that as temperature increases from 73 to 125^{o}C, MAP vapor pressure presents negligible changes, whereas DAP vapor pressure changes from 107.6 to 300 kPa, respectively. As the effect of K_{St} is associated to the rate of pressure rise, we believe that in the course of a dust explosion, the presence of DAP and MAP will mainly affect the cornstarch combustion kinetics rather than the thermodynamics.

5.4. Semi-empirical model

A simplified model was developed to identify the factors dominating the reduction of cornstarch explosion severity. The model is useful to understand the effect of the inhibitor size on the amount of heat absorbed during the homogeneous combustion of cornstarch. The inhibitor particles consume heat to reach the flame temperature and during their endothermic decomposition. The model proposed here is particularly focused on the sensible heat absorption prior to particle decomposition. Figure 36 shows

a schematization of the combustion wave propagating through a mixture of cornstarch, air and inhibitor.

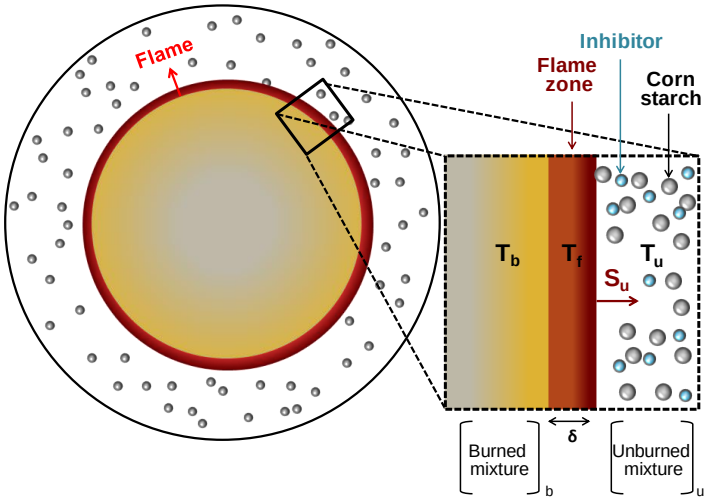

Figure 36. Schematization of cornstarch explosion propagation in a constant volume vessel in presence of inhibitor particles. T_b and T_u represent the temperature of the burned and unburned mixture and T_f is the flame temperature. S_u represents the burning velocity and δ is the thickness of the flame zone.

For the model, we assumed a fast pyrolysis-volatilization of cornstarch, where the unburned mixture is exclusively composed by combustible gas and inhibitor particles. The heat released from the gas combustion is transferred to the inhibitor particles to raise their temperature from T_u to T_b. The rate of temperature rise of a single inhibitor particle is affected by the mass, surface area and heat capacity as shown in the following expression:

$$h_g A_p\left(T_g - T_p\right) = m_p C_p \frac{dT_p}{dt} \quad \textbf{(37)}$$

where, t, h_g and T_g correspond to the time, gas heat transfer coefficient (20 W/m^{2}K) and temperature of the gas mixture; A_p, m_p, C_p, and T_p represent the surface area, mass, heat capacity and temperature of the inhibitor particle, respectively. The number of inhibitor particles is obtained from the total mass of the inhibitor added to the gas cloud:

$$m_p = n\rho_p V_p \quad \textbf{(38)}$$

where, n, ρ_p and V_p correspond to the number, density and volume of inhibitor particles. Hence, the temperature rise of a set of multiple inhibitor particles as a function of time is given by:

$$h_g n A_p\left(T_g - T_p\right) = n\rho_p V_p C_p \frac{dT_p}{dt} \quad \textbf{(39)}$$

The rate of heat transfer from the gas (volatilized cornstarch) to a set of particles causes a gas temperature reduction as a function of time:

$$h_g n A_p\left(T_g - T_p\right) = -\rho_g V_g C_g \frac{dT_g}{dt} \quad \textbf{(40)}$$

where, ρ_g and V_g represent the gas density and volume. The gas volume was considered equal to the explosion vessel volume (36 L).

The gas (T_g) and inhibitor particles temperature profiles (T_p) were calculated as a function of time by solving differential equations 3 and 4 numerically using the Runge-Kutta method. The inhibitors' properties used in this calculation are listed on Table 15. At t = 0, T_g was taken equal to the maximum flame temperature of 20 μm cornstarch (1564 K)[191], and T_p was assumed near to ambient temperature (300 K). The calculated T_g and T_p values as a function of time, for mixtures of cornstarch and MAP or

DAP are plotted in Figure 37. Similarly to the experimental work described in section 5.2.5., the calculations were conducted using MAP and DAP having a size of 26, 54, 76.5, 98, 128, 165, and 240 μm. Additionally, the effect of inhibitor concentration was evaluated by using 35, 50 or 75% of MAP and 50% of DAP, independently.

Table 15. The characteristics of MAP and DAP

Inhibitor	Molecular weight	[a]C_p	[b]ΔH^o_f
MAP ($NH_4H_2PO_4$)	99 kg/kmol	33.93 cal/kmol (1432.6 J/K-kg) [223]	-29000 cal (1224 J/mol) [224]
DAP ($(NH_4)_2HPO_4$)	116 kg/kmol	42.82 cal/kmol (1543 J/K-kg) [225]	-48,500 cal (1747 J/mol) [224]

a: Heat capacity at constant pressure

b: Standard enthalpy of formation at 298.15 K

In general, we observed that by reducing the inhibitor size, the particles temperature increases more rapidly. This effect is attributed to the particle surface area, which increases as particle diameter decreases. Based on equations 37 and 40, the increment on particle surface area favors the heat transference from the gas phase to the inhibitor particles, which ultimately causes a faster gas temperature reduction.

The effect of inhibitor concentration on T_g is observed in Figure 37a, b, and c. T_g decreased promptly as inhibitor mass load increases. This result is explained by the increment of the total number of inhibitor particles, n, and thus the total surface area

available for heat transference (Equation 40). The small differences on the chemical structures of MAP ($NH_4H_2PO_4$) and DAP ($(NH_4)_2HPO_4$) resulted in significant differences on their efficiency as explosion inhibitors. Figure 37b and d show that for a given inhibitor concentration and size, DAP reduces more rapidly the gas temperature than MAP. These results are due to the additional endothermic reactions undergone by DAP (Equations 32 and 33).

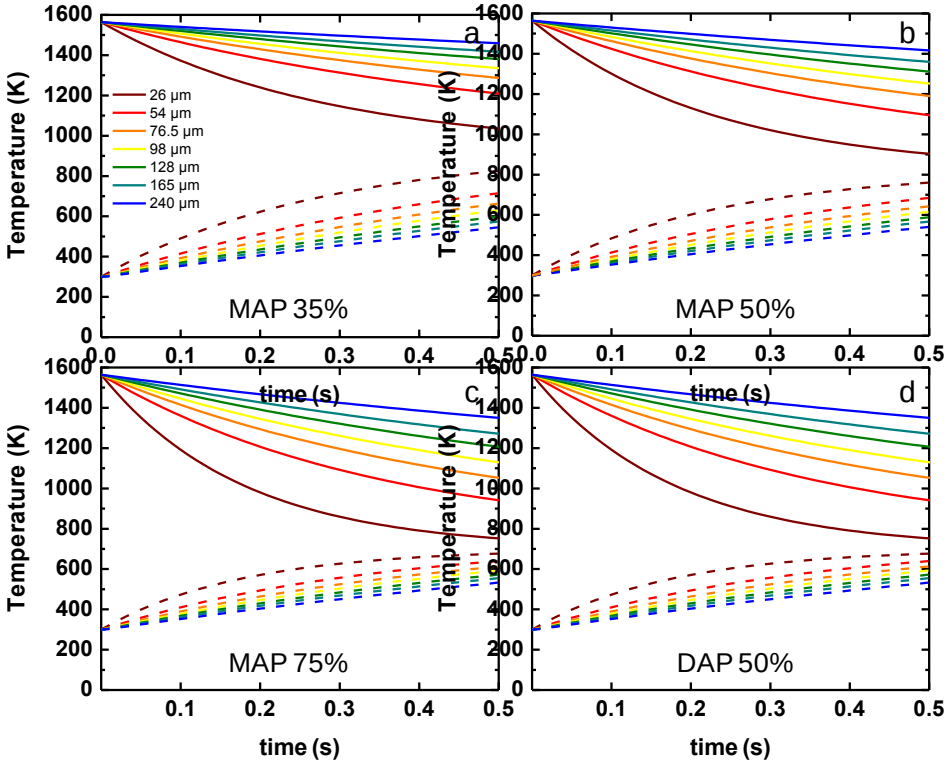

Figure 37. Temperature profiles of gas (T_g) and inhibitor (T_p). Mixtures of cornstarch and (a) MAP 35%, (b) MAP 50%, (c) MAP 75% and (d) DAP 50%. T_g and T_p correspond to solid and dashed lines, respectively.

5.4.1. Correlation between flame temperature and K_{St} values

The temperature profiles shown in Figure 37 were used to evaluate the temperature reduction obtained during each explosion using different inhibitors. The gas temperature was evaluated at the combustion time (t_c), which is the time span between ignition and P_{max}. Figure 38a shows the pressure (barg) profile as a function of time (ms) in three different explosion tests, where t_c are obtained. Mixtures of cornstarch with 35% of MAP having diameters of 76, 54 and 26 μm presented t_c values of 59, 57 and 55 ms, respectively. We observed that MAP particles with the smallest size (26 μm) inhibit more efficiently the flame propagation; P_{max} is achieved at higher t_c values, which means that the explosion energy is released in longer periods of time. The t_c values obtained in Figure 38a were used as a reference in Figure 38b to estimate the gas temperature. Finally, the temperature of the burning gas corresponds to the flame temperature. Figure 38b confirms that longer t_c values are associated to lower flame temperatures.

Subsequently, T_f was correlated to the rate of pressure rise based on similarities with gas explosions. In general, the flame propagation velocity and the rate of pressure rise of gas explosions are proportional to the flame temperature [118]. Figure 39a shows the flame temperature and the normalized rate of pressure rise as a function of fuel concentrations. At any given concentration, T_f and $(dP/dt)_{ex} \times V^{1/3}$ are directly related. These parameters achieved the maximum values at stoichiometric conditions (equivalent ratio = 1), and decrease as the fuel-air mixture becomes lean (equivalent ratio <1) or reach (equivalent ratio >1).

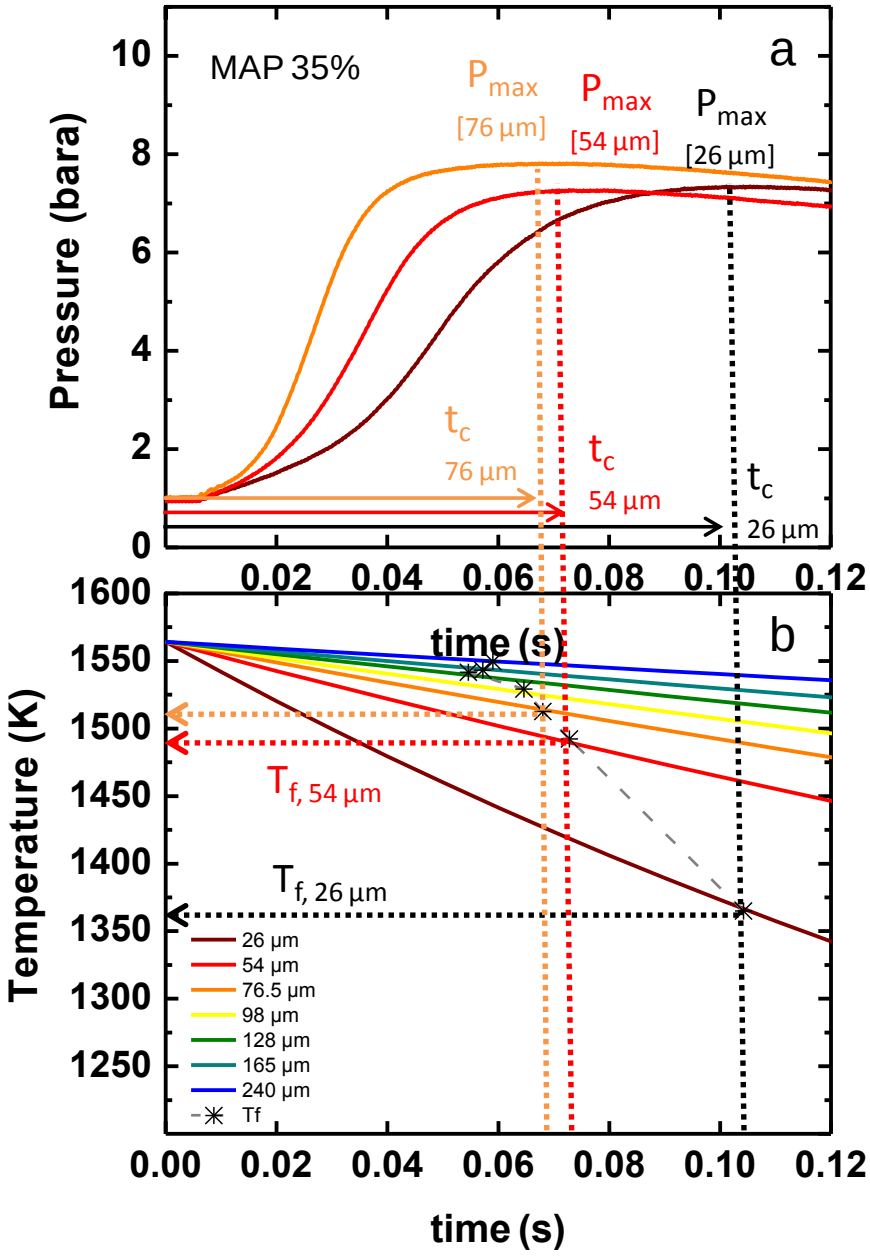

Figure 38. Calculated flame temperature achieved during dust explosion tests (a) Experimental pressure profiles obtained from dust explosion tests and (b) calculated flame temperatures as a function of time.

Figure 39b shows experimental T_f and $(dP/dt)_{ex} \times V^{1/3}$ values as a function of dust concentration, obtained in a fluidized bed [191] and a 36 L vessel, respectively. The amount of fuel volatilized per unit volume in each piece of equipment is different. However, the linear portion of the curves in Figure 39b suggest that the reduction on $(dP/dt)_{ex} \times V^{1/3}$ from 156 to 40 bar-m/s, corresponds to a reduction on T_f from 1564 to 733 K. Therefore, $(dP/dt) \times V^{1/3} \sim 0.16\ T_f - 77.3$. Finally, $(dP/dt)_{ex} \times V^{1/3}$ can be replaced by K_{St} because the inhibitors were tested at the optimum cornstarch concentration (750 g/m^3), hence:

$$K_{St} \sim 0.16\ T_f - 77.3 \qquad \textbf{(41)}$$

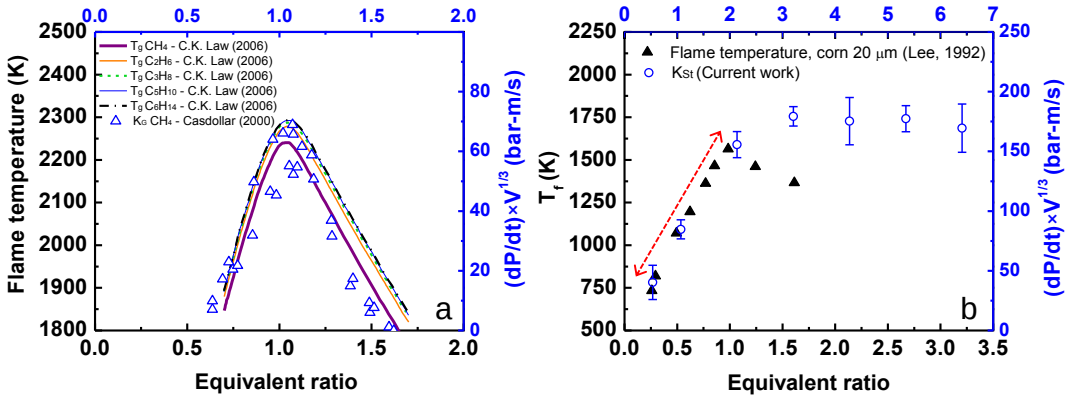

Figure 39. Flame temperature (T_f) and the normalized rate of pressure rise ($(dP/dt) \times V^{1/3}$) as a function of fuel concentrations. (a) Gas explosions (b) Dust explosions.

Basically, the experimental t_c value (Figure 38a) is used to estimate T_f (Figure 38b), which is translated into K_{St} using Equation 41. The same procedure was followed with other inhibitor concentrations and particle size. Finally, the predicted K_{St} values are compared with the experimental results as illustrated in Figure 40. Although the model neglects the inhibitor volatilization process, the trends of experimental K_{St} values are captured reasonably well. Despite the lack of information about the detailed reaction mechanisms of the mixtures, this simplified approach provides valuable information regarding the inhibition mode. For instance, the calculated values show that the heat consumed to raise the inhibitor particle temperature is significantly lower compared with the heat consumed during the inhibitor decomposition.

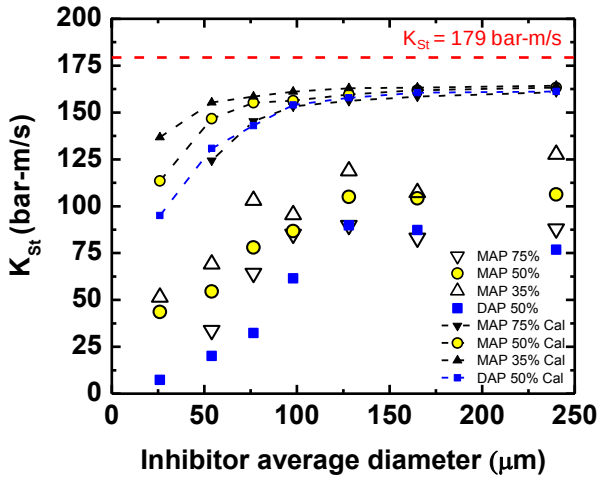

Figure 40. Predicted and experimental K_{St} values as a function of inhibitor average diameters. Mixtures containing cornstarch and MAP or DAP at different concentrations. Red dashed line represents the reference values of pure cornstarch (K_{St} = 179 ± 8 bar-m/s).

In agreement with experimental results, calculated K_{St} values are almost constant using inhibitor size above 128 μm. However, below 128 μm, the large inhibitor surface area favors heating and volatilization and accordingly enhances the inhibitor efficiency. The results suggest that above 128 μm, the inhibition mechanism is controlled by heat transfer, whereas below 128 μm the inhibition mechanism is dominated by mass transfer.

5.5. Effect of particle size and crystallinity on *α*-ZrP effectiveness as explosion inhibitor

5.5.1. Samples preparation

Particle size and crystalline level of *α*-ZrP can be precisely controlled using different phosphoric acid concentrations and reaction times during its synthesis by the reflux or hydrothermal method [193, 194]. In reflux method (RF), 1 g of $ZrOCl_2 \cdot 8H_2O$ is refluxed with 10 mL of H_3PO_4 solution in a Pyrex glass flask at 100^{o}C for 24 h [194]. In hydrothermal method (HT), 1 g of $ZrOCl_2 \cdot 8H_2O$ is mixed with 10 mL of H_3PO_4 solution. The mixture is subsequently heated at 200^{o}C for 24 h in an autoclave with a Teflon lining inside. In both methods, the reaction products are centrifuged and dried at 65^{o}C for 24 h [194]. The synthesis procedure and resulting *α*-ZrP sample characteristics are summarized in Table 16.*α*-ZrP X-ray Diffraction (XRD) patterns and Scanning Electron Microscopy (SEM) micrographs for the synthesized samples are shown in Figure 41 a and b, respectively.

Table 16. Characteristics of *α*-ZrP samples synthesized at different conditions

Sample size	Method	H_3PO_4 Concentration	Reaction time	Temp.	Crystalline level
3 µm	HT	15 M	24 h	200 °C	Regular
500 nm	HT	6 M	24 h	200 °C	Regular
200 nm	HT	3 M	24 h	200 °C	Intermediate crystallinity (IC)
200 nm	RF	12 M	24 h	200 °C	High crystallinity (HC)
-	RF	3 M	2 h	25 °C	Amorphous (A)

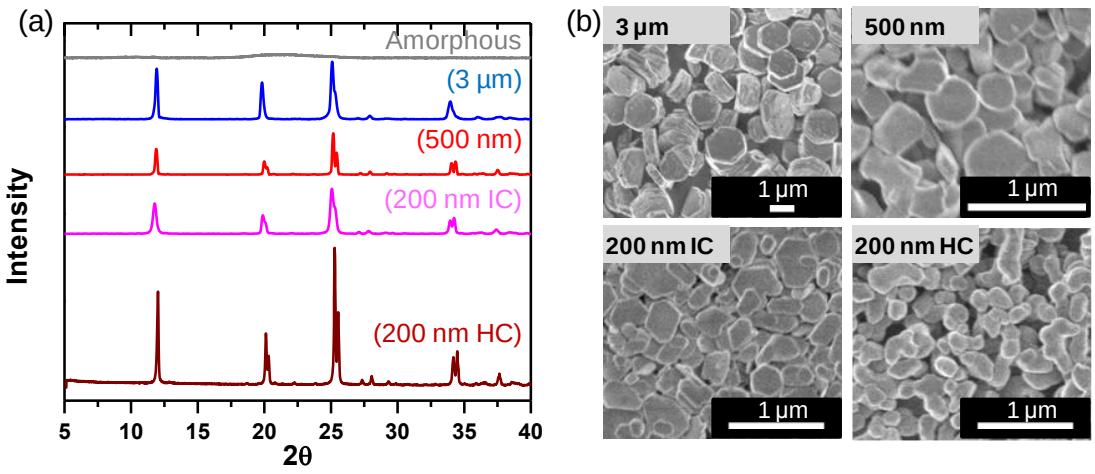

Figure 41. *α*-ZrP phosphate crystals prepared by reflux (RF) and hydrothermal (HT) method [194]. (a) XRD diffractogram and (b) SEM micrographs of different *α*-ZrP sizes prepared by reflux (RF) and hydrothermal (HT) method.

5.5.2. Thermo gravimetric analysis (TGA)

The thermal stability of mixtures of cornstarch with α-ZrP was evaluated using thermo-gravimetric analysis (TGA). Figure 42 a and b show the weight loss and derivative of weight loss percentage, respectively, as a function of temperature of samples containing cornstarch only and mixtures of cornstarch and each type of α-ZrP in a ratio of 1:1.

We observed that the thermal stability of cornstarch was improved by the presence of α-ZrP. As shown in Figure 42 a and b, mixtures containing α-ZrP presented a reduction of weight losses in comparison to the sample containing pure cornstarch. As temperature increases, α-ZrP undergoes the following decomposition reaction [33]:

$$Zr(HPO_4)_2 \cdot H_2O \xrightarrow{-H_2O} Zr(HPO_4)_2 \xrightarrow{-H_2O} ZrP_2O_7 \quad (10)$$

In general, the thermogravimetric curves of the mixtures containing α-ZrP exhibit three regions: the release of solvent from the crystal surface between 25 to 91^{o}C, followed by a loss of the water intercalated in the structure between 91 to 178^{o}C, and finally the condensation of the phosphates around 505^{o}C [226]. However, the weight loss percentage does not overtake 100% because the α-ZrP is not fully decomposed at 800^{o}C.

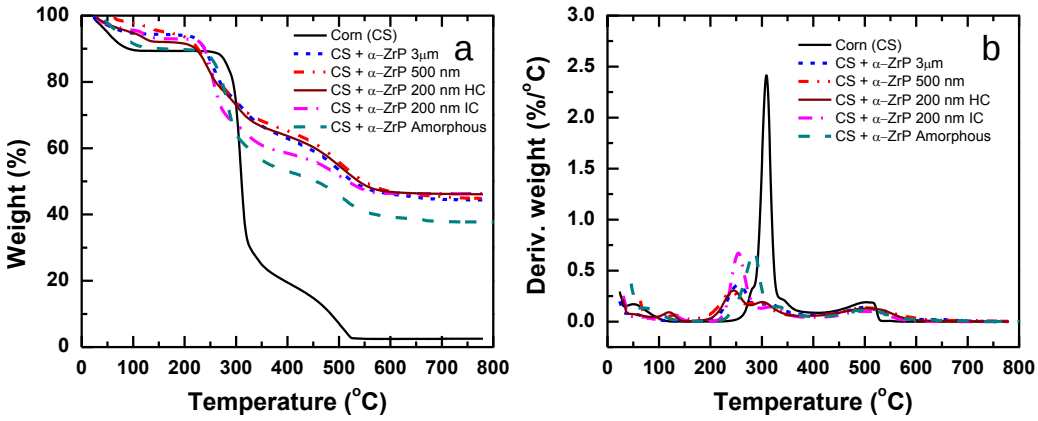

Figure 42. Thermo-gravimetric curves of cornstarch and cornstarch in the presence of explosion inhibitors, heating rate 10°C min^{-1}(in air). (a) The weight percentages of the mixtures. (b) Derivatives to the weight percentages.

The thermogravimetric curves of the mixtures containing α-ZrP of 3 μm and 500 nm, presented similar profiles of percentage of weight loss (Figure 42a). In contrast, the TGA profiles from the mixtures containing different crystallinity were dissimilar. Interestingly, the percentage of weight loss decreases more sharply as crystallinity decreases. This behavior can be explain by the differences on the water release rate and differences on the surface energy of α-ZrP created by reflux and hydrothermal method. As the α-ZrP crystallinity decreases, the water escapes more easily from the structure. For instance, the mixtures containing amorphous α-ZrP presented the largest water release below 100°C. Inhibitors characterized by intermediate (*i.e.*, α-ZrP 200 nm IC) of very low crystallinity (α-ZrP 200 amorphous) exhibited accelerated rates of weight loss at 255 and 285°C, respectively (Figure 42b). Additionally, materials with imperfections,

including surface defects, or crystallographic misalignments inside the structure generated during the crystal synthesis, represent places with high energy state. In these places the atoms are less regularly bonded, so they can be unstable with temperature changes and more prone to react [227]. Previous studies report that initial weight losses of composites containing α-ZrP can be associated to the promotion of char formation [208, 209, 228]. However, more evidence is needed to distinguish if the weight loss acceleration benefits the α-ZrP performance as inhibitor for dust explosion applications. Interestingly, the mixture containing α-ZrP of 500 nm offers the highest thermal stability to the mixture, likely associated to a gradual release of water from the structure.

5.5.3. Differential scanning calorimeter (DSC) of α-ZrP

The DSC thermograms of mixtures containing cornstarch and α-ZrP in a ratio of 1:1 are shown in Figure 43. Samples containing α-ZrP at two different sizes and three different crystalline levels were evaluated. The experiments were conducted using the procedure described in section 5.2.4. DSC results of pure cornstarch are also included as a reference. In general, all mixtures containing α-ZrP as inhibitor exhibited a reduced exothermic peak compared to pure cornstarch sample (Figure 43). The heat released from the analyzed mixtures is summarized in Table 17.

Reductions on inhibitor particle size seem to benefit the inhibitor efficiency. For instance, decreasing the inhibitor size from 3 μm to 500 nm reduced the heat released from 446 to 331 J/g. On the other hand, results from the variation of inhibitor crystallinity are not very conclusive. Apparently, an optimum crystalline level is required to improve the inhibitor efficiency. As indicated in Figure 43 and Table 17,

mixtures with α-ZrP having extremely low (*i.e.*, amorphous) and high crystalline levels, presented a marginal reduction of the cornstarch heat release (*i.e.*, 437 and 530 J/g, respectively). Nevertheless, the mixture with α-ZrP having an intermediate crystalline level (α-ZrP 200 nm IC) presented a lower heat release during the mixture decomposition (382 J/g). This behaviour might be explained by the extremely rapid release of water from the amorphous inhibitor and the restricted release of water from the highly crystalline inhibitor. Therefore, we conclude that a gradual release of water from the interlayer is crucial to enhance the inhibitor efficiency.

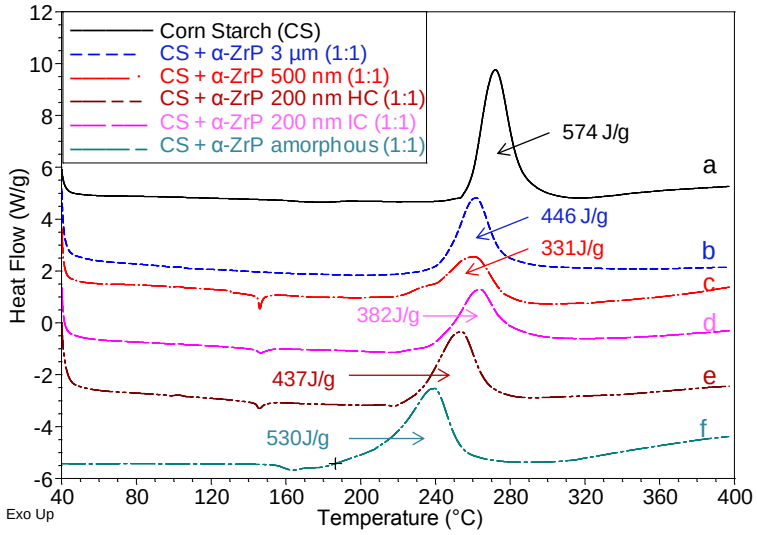

Figure 43. DSC thermograms of inhibitors under inert atmosphere. The temperature was rise from 40 ^{o}C to 400 ^{o}C, using a heating rate of 10 ^{o}C/min. (a) Pure cornstarch. (b-f) Mixtures (1:1) of cornstarch and α-ZrP of 3µm, 500 nm, 200 nm intermediate crystallinity, 200 nm high crystallinity, and amorphous nano-crystals. Results normalized based on cornstarch weight.

Table 17. Total heat release during decomposition using differential scanning calorimeter.

Mixture	Heat released (J/g of cornstarch)
Pure cornstarch (CS)	574
CS + α-ZrP 3 μm	446
CS + α-ZrP 500 nm	331
CS + α-ZrP 200 nm HC	437
CS + α-ZrP 200 nm IC	382
CS + α-ZrP Amorphous	530

5.5.4. Dust explosion tests in a 36 L vessel

To verify the effect of particle size and crystalline level in reducing the cornstarch explosion severity, dust explosion tests were carried out using mixtures of α-ZrP and cornstarch at the optimal cornstarch concentration (750 g/m^3). The experiments were performed using particles of α-ZrP having two different particle sizes (*i.e.,* 3 μm and 500 nm) and two crystalline levels (IC and HC). Amorphous α-ZrP was not considered for this analysis because it exhibited an exothermic decomposition in absence of cornstarch. The tested mixtures contained 27 g of cornstarch and 13.5 g of α-ZrP, which correspond to 50% of the total cornstarch weight. The obtained values of P_{max} and K_{St} for the mixtures were plotted for each inhibitor type (Figure 44).

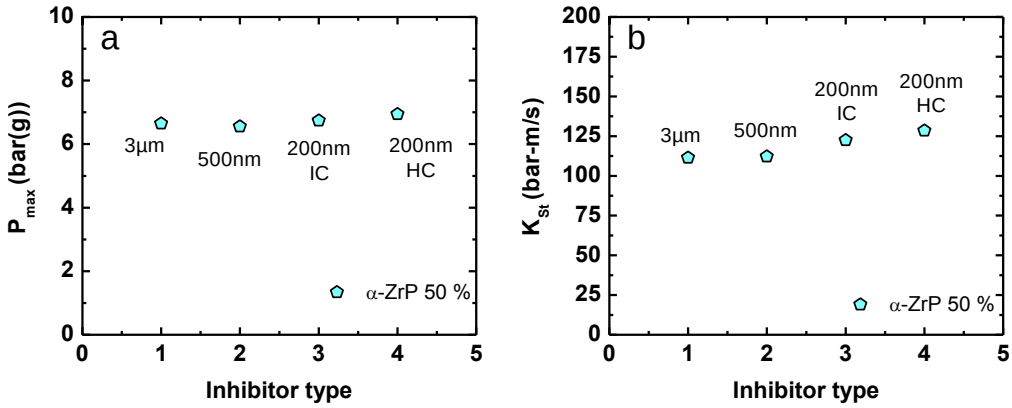

Figure 44. Effect of inhibitor crystalline level on cornstarch explosion characteristics. Mixtures contained cornstarch (750g/m^3) and 50 wt% addition of *α*-ZrP. (a) P_{max} and (b) K_{St}.

The values of P_{max} and K_{St} obtained from experiments in the 36 L explosion vessel (Figure 44) show a low dependency of the inhibitor efficiency at varying particle size and crystallinity. On average, the use *α*-ZrP as an inhibitor results in a reduction of P_{max} from 8.1 bar to 6.7 barg (*i.e.*, ~ 17% reduction) and a reduction of K_{St} values from 179 to 119 bar-m/s (*i.e.*, ~ 34% reduction). This reduction on explosion severity did not exceed the explosion protection offered by MAP or DAP (K_{St} values reduced by almost 45% percent). The lower efficiency of *α*-ZrP as explosion inhibitor in comparison to MAP and DAP is mainly attributed to a reduced rate of heat absorption. We consider that the special features of *α*-ZrP will exert a more pronounced effect in fire protection applications (*e.g.,* inhibitor used as nanocomposite), where the velocity of the combustion reaction is substantially lower compare with the explosion reaction.

5.6. Conclusions

The influence of size and crystallinity on the efficiency of dust explosion inhibitors was systematically studied. The experiments were conducted using cornstarch as a combustible dust and MAP, DAP and α-ZrP as dust explosion inhibitors. MAP and DAP were fractionated at different particle sizes (*i.e.,* 26, 54, 76.5, 98, 128, 165 and 240 μm) and α-ZrP was synthesized at varying sizes (*i.e.,* 3 μm and 500 nm) and crystalline levels (*i.e.,* low, intermediate and high). DSC and TGA were used to analyze the thermal stability and heat absorption capabilities of each type of inhibitor. Additionally, a 36 L dust explosion vessel was used to quantitatively compare the role played by inhibitor particle size on the reduction of cornstarch explosion severity.

DAP presented the highest efficiency as dust explosion inhibitor. The outstanding heat absorption capabilities of DAP were explained by the release of large amounts of ammonia (NH_3) during its endothermic decomposition. This process not only reduces the flame temperature but also lowers the concentration of flammable gases, which ultimately delays the explosion propagation. Compared to DAP, MAP released a lower amount of NH_3, which resulted in reduced inhibitor efficiency. Surprisingly, DSC thermograms revealed that MAP promoted the cornstarch combustion. From this observation, it is believed that MAP should be used to mitigate rather than to prevent dust explosions. In general, experimental results from dust explosion tests confirmed the crucial role of particle size on improving the inhibitor rate of heat absorption. As the particle size decreases below 128 μm, the inhibition mechanism evolves from a heat transfer to a mass transfer controlled process. A

simplified model was developed to identify the effects of particle size on the reduction of the dust explosion severity. The model provides insights of the limiting diameter required to enhance the inhibitor efficiency and the dominant effects of the nonflammable gases on the reduction of the flame temperature.

We also evaluated the α-ZrP inhibitor capability at varying particle size and crystalline level. As expected, α-ZrP provided the highest thermal stability of the mixtures. However, this material was characterized by a lower heat absorption in comparison with MAP and DAP. Intriguingly, it was observed that an intermediate crystalline level having a gradual release of water from its interlayer structure benefits the inhibitor efficiency. This study provides valuable guidance for the design of novel hybrid composites with dual applications in fire and dust explosion protection. For instance, taking advantage of the α-ZrP ion exchange and lamellar structure [229], α-ZrP can be intercalated with compounds of superior heat absorption such as DAP. The α-ZrP matrix would offer a strong thermal barrier in a fire event and permit a progressive release of intercalated DAP and water that would absorb energy during a dust explosion.

CHAPTER VI

SIMULATING DUST EXPLOSIONS VENTED THROUGH DUCTS*

6.1. Synopsis

The computational fluid dynamics (CFD) code DESC has been used to simulate a series of dust explosion experiments performed in an 18.5 m^3 vessel equipped with vent ducts of varying cross sections and lengths. The motivation behind the work is threefold: to validate the CFD code, to gain increased understanding of the parameters affecting dust explosion venting through ducts, and to investigate the validity of empirical correlations found in various standards and guidelines for design of explosion protection systems. Although the results from simulations agree reasonably well with experimental observations, DESC tends to underpredict the reduced explosion pressures for scenarios with vent ducts with diameters significantly larger than the vent openings. These discrepancies may be a result of inherent limitations in the model system, but poor repeatability and limited access to detailed experimental data complicates the analysis. Results from experiments and simulations are compared with predictions from various standards and guidelines for design of vent ducts in industry: EN 14491, VDI 3673, NFPA 68, and the methodology developed by FM Global. The correlations in NFPA 68, derived from the same set of experiments in the 18.5 m^3 vessel, yield the most accurate

---

* This Chapter contains material that has been reproduced with permission from: D. Castellanos, T. Skjold, K. van Wingerden, R. K. Eckhoff and M. S. Mannan. Validation of the DESC Code in Simulating the Effect of Vent Ducts on Dust Explosions. Industrial & Engineering Chemistry Research, 2013. 52(17): p. 6057-6067. Copyright (2013) American Chemical Society.

predictions. The FM Global method underestimates the reduced explosion pressure for the largest vent diameter and rear ignition, and yields conservative results for smaller duct diameters. Neither experiments nor simulations support the concept of a critical duct length prescribed in EN 14491 and VDI 3673.

6.2. Introduction

Accidental dust explosions continue causing severe losses in the process industry. For practical reasons, processing combustible powders takes place within closed units such as mills, dryers, filters, elevators, conveyors, and silos. In many situations it is not possible to achieve acceptable levels of safety through prevention and inherent safety alone, and it is necessary to implement suitable mitigating measures [1]. Explosion venting is a widely used mitigation method, where destructive overpressures are prevented by designing parts of the equipment to fail during early stages of the explosion, allowing unreacted mixture, flames, and combustion products to escape to the surroundings. Vent openings should not discharge into workrooms, so when process units are placed inside buildings it is common practice to convey explosions to safe areas by means of vent ducts [230-234]. However, a vent duct of significant length represents a restriction for the outflow from the vessel, and phenomena such as conservation of mass and momentum, wall friction, and enhanced rate of combustion due to turbulent flow conditions, and acoustic oscillations should be taken into account when designing the system. Flameless venting devices represent an alternative to vent ducts, but this solution is relatively expensive, the effective vent area is significantly reduced, hot

combustion products are still released to the surroundings, and this method is generally not suitable for metal dusts, flocculent particles, *etc.* [234-236].

Several parameters influence the reduced overpressure P_{red} in a vented dust explosion. The reactivity and energy content of the dust cloud are typically characterized by the size corrected maximum rate of pressure rise K_{St} and the maximum overpressure P_{max}, measured in constant volume explosion vessels. Relevant parameters characterizing the protected system include the volume V and aspect ratio L/D of the enclosure; the position, area A_v and opening pressure difference P_{stat} of the venting device; as well as the diameter D_d, length L_d, and presence of bends or obstructions in the vent duct. Finally, P_{red} also depends on initial and boundary conditions, such as the initial pressure P_0 and temperature T_0, the initial turbulent flow conditions, the initial concentration distribution inside the enclosure, the position and strength of the ignition source, the presence of accumulated dust layers or other dust deposits, as well as various factors influencing the transient flow and combustion phenomena that take place during vented explosions.

6.3. Previous experimental work on vent ducts

The effects of vent ducts on the reduced explosion pressure in vented dust explosions have been extensively studied in the past. Brown [237] investigated cork dust explosions in a 3 m long gallery with a diameter of 0.25 m. The explosion pressure increased significantly when the gallery was vented through ducts of increasing length and when extra dust was dispersed near the vent. Hartmann and Nagy [158] observed a near linear increase in P_{red} with increasing duct length for straight unobstructed ducts-

with 0.1 m square cross sections and connected to a 28.3 L gallery. With a diaphragm installed between the gallery and the duct, P_{red} significantly increased in comparison to the unobstructed duct for duct lengths up to about 1.5 m. However, no significant changes in P_{red} were observed in the range 1.5 m < L_d < 5.2 m. Similar results were found for cellulose acetate and maize starch. The effect of introducing bends in the vent duct was most pronounced for short ducts, and a uniform layer of dust in the duct increased P_{red} by 30-50%. Segalova and Resnik [238] investigated the effect of vent ducts on peat dust explosions using a 14 L vessel. They found that P_{red} steadily increased with increasing duct length up to a certain critical length beyond which negligible pressure change was obtained.

Hattwig [239, 240] conducted experiments in vessels of volume 0.25 and 1.0 m^3, vented through ducts with a diameter of 0.2 m and lengths up to 12 m, and observed a steady increase in P_{red} up to about 2-3 times the pressure obtained without a duct for duct lengths up to 5 m. The reduced explosion pressure remained nearly constant for longer duct lengths, bends in long ducts had no significant effect on P_{red}, and dust deposits in the duct had only modest effects. Hattwig [239] also reported results obtained by Scholl in a 30 m^3 vessel equipped with a 1.4 m diameter vent duct with lengths up to 5 m, where P_{red} reached a maximum value for L_d = 3 m and decreased slightly for longer ducts. Pineau [241-243] performed experiments with vent ducts fitted to vessels of volume 2.5, 10 and 100 m^3. However, the effect of varying the duct length was only investigated for a 0.7 m diameter duct fitted to a 0.6 m vent opening on the 10

m^3 vessel. The results indicate a steady increase in P_{red} for the entire range of duct lengths investigated: 3, 6, 9 and 12 m.

Bartknecht [17] reported results obtained in a 2.0 m^2 vessel fitted with 0.4 m diameter vent ducts for dusts with K_{St} values 150 or 300 bar-m s^{-1}, and pointed out that the most severe increase in P_{red} occurred when the discharge velocity reached or exceeded the speed of sound (expected to occur at L_d > 3 m). The results were not particularly sensitive to L_d for low and very high dust concentrations, whereas P_{red} typically increased by a factor of two when L_d was increased from 2.5 to 7.5 m for the most reactive concentrations. Aellig and Gramlich [244] investigated the effect of the shape of the entrance to the vent duct (D_d = 0.53 m), as well as the effect of introducing sharp or rounded bends in the duct, for vessels of volume 2.0 and 2.4 m^3.

Kordvlewski and Wach [245-247] investigated the effect of vent ducts on P_{red} for vented explosions in 20 and 22 L spherical vessels. The experiments covered duct diameters in the range of 21-76 mm and duct lengths up to about 15 m. It was found that P_{red} reached a plateau value for a certain duct length, and further increases in L_d had little effect. The UK Health and Safety Executive (HSE) [44, 248] obtained similar results in a 20 L spherical vessel fitted with vent ducts of diameter 76, 100 or 128 mm, and duct lengths up to 3.3 m. These results are consistent with the observations by Nagy and Hartmann [158]. Lunn *et al.,* [44] and Hey [249] reported results from extensive experimental campaigns where an 18.5 m^3 vessel was equipped with vent ducts of varying length and diameter. These experiments will be described in more detail in section 2.1.

Griesche [250, 251] reported results from experiments in two explosion vessels: a 1.2 m^3 vessel fitted with vent ducts of lengths 2, 4, 6, 8 and 10 m and diameters of 0.250, 0.315 and 0.400 m; and a 10 m^3 vessel fitted with vent ducts of lengths 1.0, 2.0, 3.0, 4.7, 5.15, 10.3 and 12.3 m and diameters of 0.21, 0.50 and 0.80 m. The measured P_{red} values steadily increased with increasing duct length [250, 251]. Unlike most of the experiments with vent ducts, where the duct is separated from the vessel by a bursting disc, vent doors were fitted at the end of the vent ducts.

The effect of vent ducts on P_{red} has been investigated for dust explosions in various process units under reasonably realistic conditions. Tonkin and Berlemont [252] explored the use of various vent duct configurations for corn dust explosions in a large-scale cyclone plant. The result showed a consistent increase in P_{red} with increasing duct length, and P_{red} also increased when a 45° bend was introduced in the duct. Radandt [253] investigated the effect of vent ducts and degrees of filling in a 20 m^3 horizontal silo (L/D = 6.26). For dust clouds that initially occupied 25 or 50% of the silo volume, P_{red} decreased significantly with a 1.5 m long vent duct, and remained more or less unchanged for a 9 m duct, compared to free venting without a duct. Complete filling resulted in a near linear increase in P_{red} with increasing duct length. Bartknecht [254] reported results from a series of vented dust explosions in a full-scale coal mill, including the effect of a 5 m long vent duct. Siwek [255-257] described a series of experiments in a 25 m^3 vessel equipped with vent ducts of lengths 3, 6 and 10 m and diameters of 0.2 or 0.3 m. Dust clouds were generated by pneumatic filling at a rate of 15 m^3 per minute, and the P_{red} values were found to increase linearly with increasing L_d.

Lunn *et al.,* [39] investigated the effect of vent ducts on vented dust explosions in two dust collectors. The effects of vent ducts on P_{red} was less than predicted by guidance for homogeneous dust clouds. The phenomena involved in vented dust and gas explosions are similar, and topical reviews should be consulted for the effects of vent ducts for systems involving gaseous fuels [41, 258, 259].

6.4. Guidelines for predicting overpressures in vented dust explosions

Various guidelines have been developed to predict the effects of vent ducts on reduced explosion pressure in dust explosions. Bartknecht [17] and Aellig and Gramlich [244] introduced nomographs where P_{red} was plotted against the reduced overpressure $P_{red,0}$ without the vent duct, with different curves for flow velocities below (L_d < 3 m) or above ($L_d \geq 3$ m) the speed of sound in air (about 330 m s^{-1}). These nomographs were included in the first versions of VDI 3673 [260, 261]. Based on the experiments described by Lunn *et al.,* [44] and Hey [249], HSE developed a set of graphs that can be used to estimate the effect of vent ducts on P_{red} [262]. Griesche [250, 251] found that P_{red} could be represented by a correlation on the form:

$$\frac{P_{red}}{P_{red,0}} = 1 + a\left(\frac{\frac{\pi}{4}D_d^2}{V^{2/3}}\right)^b\left(\frac{L_d}{D_d}\right)^c \qquad \textbf{(42)}$$

where a, b and c are empirical constants. Bartknecht [254] reviewed a series of vented dust explosion experiments with vent ducts, performed in vessels from 1 to 30 m^3 and dusts with K_{St} values from 100 to 320 bar-m s^{-1}. The results from the experiments were compared to the updated VDI 3673 guideline [160] and other published relationships [250], and alternative correlations were proposed. Current standards include NFPA 68

[161] in the US and EN 14491[263] in Europe, as well as the updated VDI 3673 standard, the HSE graphs [262], and the methodology developed by FM Global [46, 264-269].

Empirical correlations have been developed to take into account phenomena such as turbulence induced by the duct [265]; obstructions, such as bends and panels, in the duct [42, 44, 264]; the inertia of vent panels [270, 271]; enclosure aspect ratio L/D [272]; flame propagation through ducts; the volume fraction X_r of the enclosure initially filled with flammable mi ture (or "the nominal filled fraction") [273]; the duct skin friction [274]; and enhanced back pressure toward the vessel due to compression waves in the duct [42, 44] The complexity of the phenomena involved when a dust explosion is vented through a duct, and the numerous parameters that play a role, suggest that it is not straightforward to develop reliable and simple guidelines from a relatively limited number of large-scale explosion experiments. Hence, the development and validation of more advanced simulation tools, not limited to simple isolated scenarios, is crucial for improving the design of vent ducts in the process industry.

6.5. Methodology

The CFD code DESC [64, 81, 275] has been used to simulate a series of dust explosions performed by HSE in an 18.5 m^3 vented vessel [44, 249], and results from the simulations are compared with the experimental data and the predictions from existing guidelines for the design of venting systems. The following sections outline the experimental set up used by HSE, the modeling in DESC, and the calculation procedures in the respective guidelines.

6.5.1. Experiments

Figure 45 illustrates the 18.5 m^3 explosion vessel used in the HSE experiments reported by Hey [249] and Lunn *et al.,* [44] The vessel was equipped with a dispersion system consisting of three 16 L dust reservoirs, initially pressurized with air to 20 bar(g), and discharged through fast-acting valves and pepper pot nozzles. The dispersed dust clouds were ignited by 30 g of black powder and triggered 0.76 s after onset of dispersion. The ignition source was located in the rear (closed end), center, or front of the vessel and the vent area was varied by means of orifice plates, from 0.950 m^2 (D_v = 1.1 m) to 0.636 (0.9 m), 0.385 (0.7 m) and 0.196 m^2 (0.5 m). Vent ducts of equal or larger cross sectional areas than the vent openings, with lengths of 1, 6, 11 or 16 m, were attached to the vessel. Coal dust with K_{St} = 144 bar-m s^{-1} and P_{max} = 7.5 bar(g), and nominal dust concentration 500 g m^{-3}, were used in all experiments considered. The pressure was recorded with transducers inside the vessel and along the vent duct.

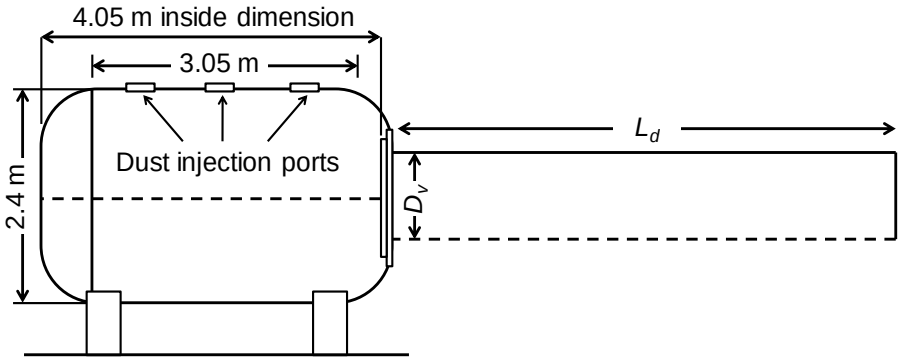

Figure 45. Schematic of the 18.5 m^3 vessel. Adapted from Hey [249].

6.5.2. Simulations

Models based on computational fluid dynamics (CFD) may overcome some of the inherent limitations associated with simplified guidelines for explosion protection in complex geometries [275]. However, the complexity of the phenomena involved in turbulent particle-laden flow and premixed combustion with non-premixed substructures [276], in large-scale industrial facilities, requires a pragmatic approach to modeling. The representation of the dust cloud in the CFD tool DESC assumes kinetic and thermal equilibrium between the continuous and dispersed phases, and flame propagation in dust clouds is represented by a turbulent burning velocity similar to the approach frequently adopted for gaseous fuels [81].

The laminar burning velocity S_L and the fraction of burnable fuel λ for coal dust used in the empirical combustion model in DESC were estimated from experiments in 20 L vessels [81]. Health and Safety Laboratory reported K_{St} and P_{max} values of 144 bar-m s^{-1} and 7.4 bar(g), respectively [44, 249], whereas Technical University of Delft and University of Bergen reported somewhat higher values for sieved (< 63 μm) and dried samples of the same dust: 180-190 bar-m s^{-1} and 8.5 bar(g) [81]. A corrected P_{max} value of 8.5 bar(g) corresponds to a measured value of about 8.0 bar(g) in the 20 L vessel [16]. The difference in explosion characteristics between the model dust and the coal dust used in the experiments is not significant relative to the inherent uncertainties in tests data from 20 L explosion vessels and the limited repeatability of large-scale dust explosion experiments. The same empirical model for coal dust has previously been used for simulating coal dust explosions in a vented connected vessel system with DESC

[81, 275]. The simulation results were quite sensitive to modest changes in ignition position and the reactivity of the fuel, but for a given set of simulation parameters DESC produced pressure-time histories that were in excellent agreement with experimental results.

Cubical grid cells of size 0.10 m were used in most simulations. The dispersion system was modeled as three transient fuel jets, impinging on porous panels in order to imitate the actual dispersion nozzles. Ignition was activated 0.76 s after onset of dispersion. Figure 46 illustrates the implemented geometry and the effect of adding a vent duct (L_d = 6 m) for a scenario with $D_v = D_d$ = 0.9 m. Adding the duct results in significant changes in pressure distribution and flow filed.

Previous studies indicate that the results obtained with DESC are sensitive to grid resolution and the reactivity of the mixture [81, 275]. The present study adopted the value 1.25 for the dimensionless factor C_L used for scaling the laminar burning velocity S_L derived from experiments in the 20 L vessel, in accordance with previous results obtained for the same grid resolution [81, 275]. Two ignition positions were explored for each of the three original positions, either along the center line of the vessel (z = 0 m) or 0.4 m below (z = -0.4 m). Ignition below the center line was included since combustion of 30 g of black powder in a transient flow field is likely to result in volumetric ignition, rather than point-like ignition. Table 18 summarizes the simulated scenarios.

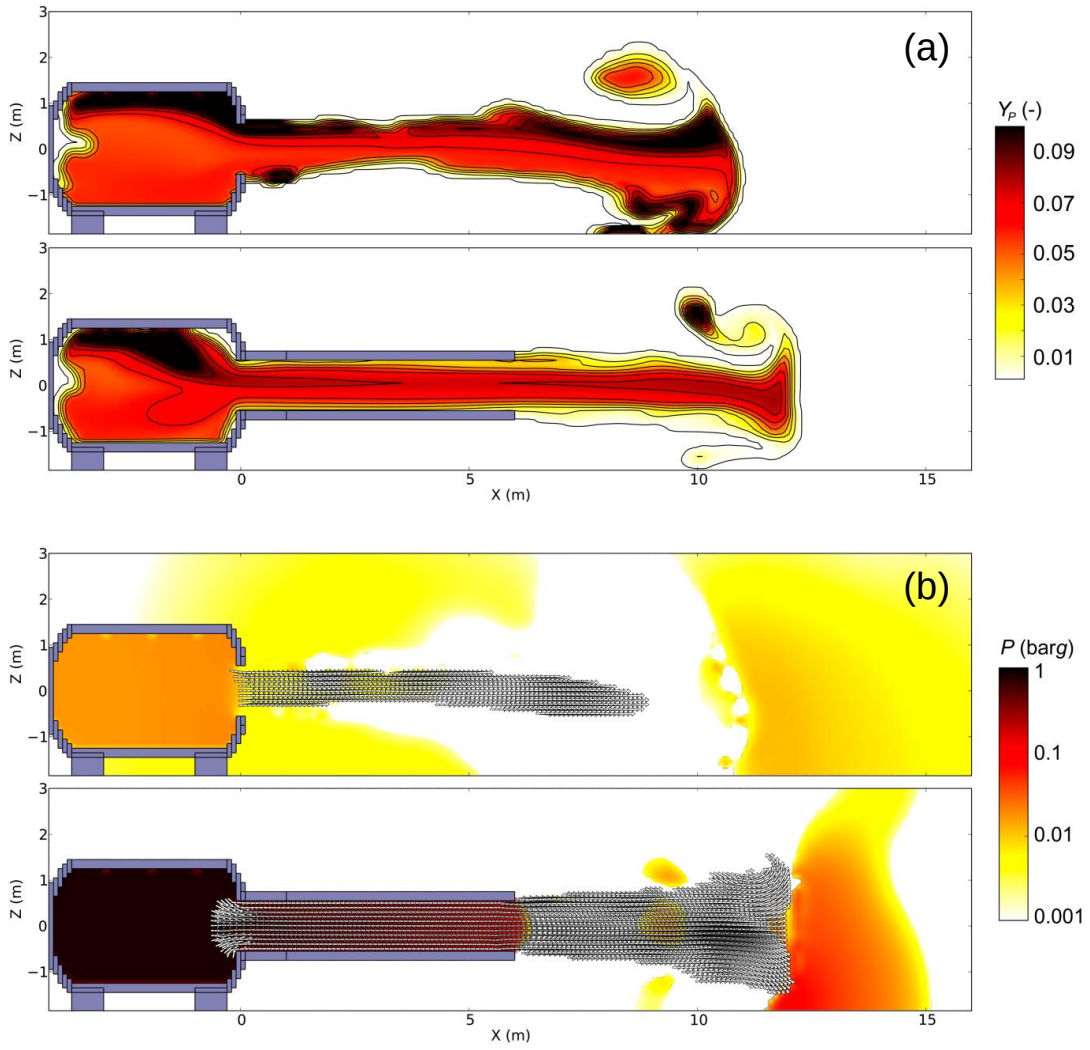

Figure 46. Vented dust explosions simulated with DESC ($D_v = D_d = 0.9$ m, $L_d = 0$ or 6 m): (a) flame represented by mass fraction of combustion products (Y_p), and (b) pressure and velocity vectors (> 100 m s-1), at a specific time step.

Table 18. Summary of the simulated scenarios for different combinations of duct and vent diameters; ignition positions: front (F), center (R) and rear (*R*); duct lengths: 0, 1, 6, 11, and 16 meters.

A_v (m^2)	D_v (m)	D_d (m)			
		0.5	0.7	0.9	1.1
0.196	0.5	*F C R*	*F C R*	*F C R*	*F C R*
0.385	0.7	–	*F C R*	–	*F C R*
0.636	0.9	–	–	*F C R*	*F C R*
0.950	1.1	–	–	–	*F C R*

6.6. Venting guidelines

Experimental and simulated results will be compared with predictions from four different vent guidelines: VDI 3673, EN 14491, NFPA 68 and FM Global. The predictions presented here are based on the following assumptions for the experiments with coal dust in the 18.5 m^3 vessel: K_{St} = 144 bar-m s^{-1}, $P_{\max}$ = 7.4 bar(g), P_{Stat} = 0.1 bar, and X_r = 1.

6.6.1. VDI 3673

The VDI 3673 guideline estimates P_{red} (bar) according to the expression [160]:

$$\frac{P_{red}}{P_{red,0}} = 1 + 17.3\left(\frac{\mathrm{A_v}}{\mathrm{V}^{0.753}}\right)^{1.6} L_d \qquad \textbf{(43)}$$

No further increase in P_{red} is predicted beyond a critical duct length L_c defined as:

$$L_c = 4.564\,(P_{red,0})^{-0.37} \qquad \textbf{(44)}$$

This approach is consistent with the observations from experiments where P_{red} was found to increase with increasing duct length up to a certain point, beyond which further increase in L_d did not influence P_{red} significantly.

6.6.2. EN 14491

The EN 14491 standard is based on the original VDI 3673 guideline [263] :

$$\frac{P_{red}}{P_{red,0}} = 1 + 17.3\left(\frac{\mathrm{A_v}}{\mathrm{V}^{0.753}}\right)^{1.6}\left(\frac{L_d}{D_d}\right) \quad \textbf{(45)}$$

No further increase in P_{red} is predicted beyond a critical duct length to duct diameter ratio defined by the expression [263]:

$$\left(L_d/D_d\right)_c = 4.564\,(P_{red,0})^{-0.37} \quad \textbf{(46)}$$

There is obviously an inherent contradiction between the EN and VDI guidelines, since the right-hand side of Equations 43 and 45 are identical, whereas the left-hand side of Equation 45 is equal to the left hand side of Equation 43 divided by D_d.

6.6.3. NFPA 68

The guideline for designing vent ducts for dust explosion protection in NFPA 68 is based on the work by Ural *et al.,* [42, 277, 278]. The procedure entails a reverse calculation where the vent area required for a system without a vent duct is estimated from the expression:

$$A_{v,0} = 1\times10^{-4}\left(1 + 1.54\,{P_{Stat}}^{4/3}\right)K_{St}V^{3/4}\sqrt{\left(\frac{P_{\max}}{P_{red}} - 1\right)} \quad \textbf{(47)}$$

The effective vent area required for a system with a vent duct is given as [277]:

$$A_v = A_{vo}\left(1+1.18\mathrm{E}_1^{0.8}E_2^{0.4}\right)\sqrt{\left(\frac{\mathrm{K_{fr}}}{k_0}\right)} \quad \textbf{(48)}$$

$$E_1 = (A_v L_d)/V \quad \textbf{(49)}$$

$$E_2 = \left(1\times10^{-4}A_v\right)/\left(1+1.54P_{Stat}{}^{4/3}\right)K_{St}V^{3/4} \quad \textbf{(50)}$$

$$K_{fr} = \frac{\Delta P}{0.5\rho u^2} = K_{inlet} + K_{df} + K_{elbows} + K_{outlet} \quad \textbf{(51)}$$

k_o is the nominal flow resistance coefficient corresponding to venting without duct (k_o = 1.5 for a discharge coefficient C_d = 0.8), and K_{fr} is the total flow resistance coefficient corresponding to a static pressure drop ΔP from the enclosure to the exit of the vent duct for a given flow velocity u and mixture density ρ. The value of K_{fr} is the sum of the local resistance coefficients for the inlet (K_{inlet} = 1.5), duct K_{df}, elbows (K_{elbows} = 0), and outlet (K_{exit} = 0.75). The duct friction component K_{df} is defined as:

$$K_{df} = f_D L_d / D_h \quad \textbf{(52)}$$

where D_h is the hydraulic diameter, and f_D is the duct friction factor:

$$f_D = \left\{1.14 - 2\log_{10}\left(\frac{\varepsilon}{D_h}\right)\right\}^{-2} \quad \textbf{(53)}$$

where ε is the effective roughness (assumed equal to 0.26).

6.6.4. FM Global

The procedure developed by Tamanini and colleagues [46, 264-267] is based on dimensional analysis. The calculation of P_{red} in the presence of a duct involves two steps. First, the vent area in the absence of a duct, $A_{v,0}$, is calculated from the expression [279]:

$$\Gamma = a_{cd} \frac{A_{v,0}}{V^{2/3}} \frac{P_{\max}}{K} X_r^{1/3} \tag{54}$$

where Γ is a dimensionless vent parameter, X_r is the nominal filled fraction [273], a_{cd} is a constant with dimensions of velocity (assumed equal to 232.5 m/s [266]), and K is the effective reactivity of the dust under venting conditions:

$$K = K_{st} \left(1 + 1.75 \frac{\Delta P_v}{P_0} \right) \left(\frac{V}{V_{ref}} \right)^{0.11} \tag{55}$$

where ΔP_v is the vent relief pressure (assumed equal to P_{Stat}), P_o is the absolute initial pressure, and V_{ref} is a reference volume. For cases with P_{Stat} equal to zero, K is assumed equal to K_{St}. The reduced pressure is obtained from the normalized pressure [273]:

$$\Pi = \frac{1}{X_r} \frac{\Delta P_{red}}{\Delta P_{\max}} \tag{56}$$

where Π is related to the dimensionless vent parameter, $\Pi = f(\Gamma)$ [267, 279, 280]:

$$\Pi = 0.05 \Gamma^{-2} \tag{57}$$

Finally, the vent area in the presence of a duct is obtained by taking into account the duct inertia parameter Φ_d and the friction loss parameter Ψ_d [279]:

$$\frac{A_{v,0} - A_v}{A_v} = 5 \Gamma^{1.5} \Phi_d \Psi_d^{0.25} \tag{58}$$

where Φ_d and Ψ_d are defined as [46, 279]:

$$\Phi_d = \frac{L_d V^{1/3}}{A_d} \frac{M}{R T_0} \left(\frac{K}{\Delta P_m} \right)^2 \tag{59}$$

$$\Psi_d = \frac{V}{L_d A_d}\left(c_f \frac{S_d L_d}{A_d} + c_\alpha \right) \quad \textbf{(60)}$$

where S_d is the duct perimeter, c_f is the friction factor (0.005), and c_α is the head loss factor which takes into account the presence of bends in the duct [46, 279]. Finally, the effective area, A_v, is inserted into the vent parameter equation (10) and the procedure is repeated to find P_{red} in the presence of a duct.

6.7. Results and discussion

This section compares results from DESC simulations with experimental data and predictions from venting guidelines. The discussion focuses on the degree of details required to yield reliable model predictions for the consequences of realistic dust explosion scenarios in the process industry.

6.7.1. Effects of duct length and duct diameter on P_{red}

Figure 47-35 summarize the results for configurations with D_v equal to D_d. Experimental and simulated results are in reasonable agreement, showing a systematic increase in P_{red} for increasing L_d. The highest pressures are found for the smallest vent diameter (0.5 m) and ignition at the rear end of the vessel, in accordance with results reported for gaseous explosions [281-284]. The simulation results are not particularly sensitive to moderate variations in the vertical position of the ignition source.

The comparison between simulation results and predictions from guidelines is not straightforward, since both VDI 3673 and EN 14491 require P_{stat} to be at least 0.1 bar. Predictions by VDI 3673 and EN 14491 are not included for D_v = 0.5 m because $P_{red,0}$ exceeds the valid range for these models ($P_{red,0}$ > 2 bar(g)). In agreement with

results reported by Tascon *et al.,* [285, 286], VDI 3673 and EN 14491 overpredict P_{red} values for scenarios with low $P_{red,0}$ when L_d is lower than L_c or $(L_d/D_d)_c$. However, both guidelines under-estimate P_{red} when L_d is larger than L_c. As summarized in section 1.1, these guidelines define a critical duct length L_c, or duct length to duct diameter ratio, beyond which a further increase in L_d has no influence on P_{red}. As outlined in section 1.1, this phenomenon has been observed in some experiments, including the ones reported by Bartknecht [254], and has been attributed to choked flow conditions in the duct. However, neither the experiments nor the simulations presented here support this assumption.

The FM Global methodology underestimates P_{red} for the largest vent diameter (1.1 m) and rear ignition. However, certain factors may affect the accuracy of these predictions. The effective reactivity (K) was assumed equal to the K_{st} value obtained from the standard 20 L vessel (K_{st} = 144 bar-m s^{-1} [44]), whereas it should have been obtained from direct measurements in the 18.5 m^3 vessel, without vent duct [46, 279], in order to properly represent the turbulence levels and the strength of the ignition source in the large-scale experiments [279, 280]. In the present work K was assumed constant because of the significant scatter in the available experimental data [280]. Due to the substantial disagreements between the data reported by Hey [249] and Lunn [44], for the same explosion scenarios performed at HSE, it is uncertain whether the K_{st} value used is representative for both data sets. Overall, the FM Global methodology yields conservative predictions for most of the scenarios presented in Figure 47-50.

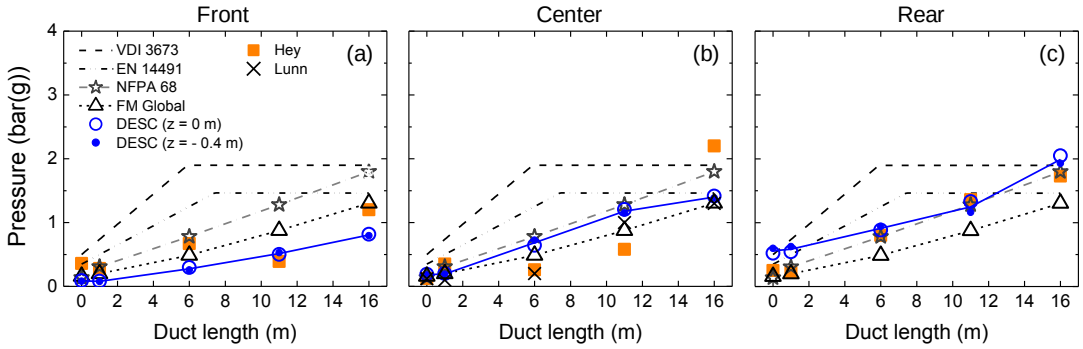

Figure 47. Effects of L_d on P_{red} for coal dust explosions in an 18.5 m^3 vessel at three different ignition positions. Configurations with $D_v = D_d = 1.1$ m. Ignition positions: (a) front, (b) center, and (b) rear.

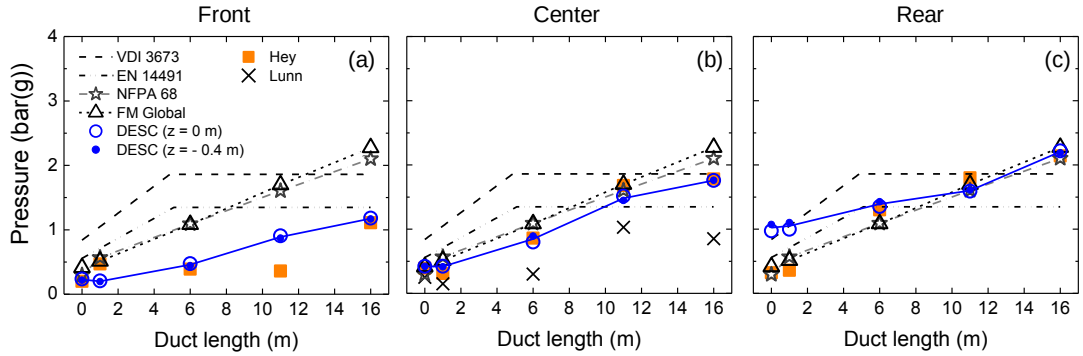

Figure 48. Effects of L_d on P_{red} for coal dust explosions in an 18.5 m^3 vessel. Configurations with $D_v = D_d = 0.9$ m. Ignition positions: (a) front, (b) center, and (b) rear.

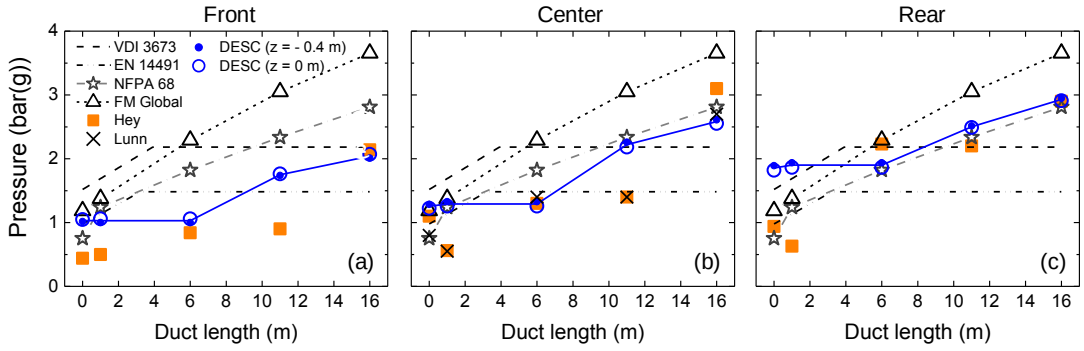

Figure 49. Effects of L_d on P_{red} for coal dust explosions in an 18.5 m^3 vessel. Configurations with $D_v = D_d = 0.7$ m. Ignition positions: (a) front, (b) center, and (b) rear.

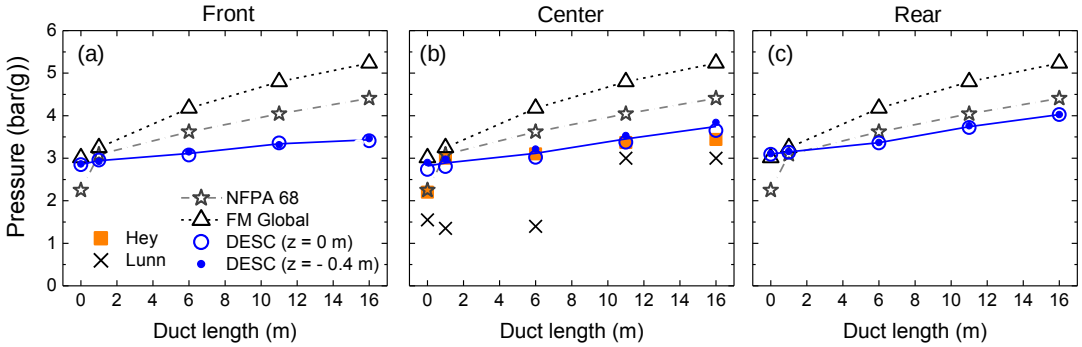

Figure 50. Effects of L_d on P_{red} for coal dust explosions in a 18.5 m^3 vessel. Configurations with $D_v = D_d = 0.5$ m. Ignition positions: (a) front, (b) center, and (b) rear.

Between the guidelines, NFPA 68 yields the most accurate predictions for the effects of L_d on P_{red}. The influence of L_d increases in a similar manner as the experimental results, indicating a reasonable selection of scaling parameters. It should however be emphasized that the empirical correlations in this guideline are derived from the same set of experiments in the 18.5 m^3 vessel [42].

Additionally analysis of the simulation results confirms the effects of vent area and duct length. Figure 51 shows the mass fraction of combustion products as a function of distance a given time for four different scenarios: $D_v = D_d$ equal to 0.5 and 0.9 m with and without duct, respectively. For instance, the scenario with $D_v = D_d = 0.5$ m and $L_d =$ 6m (Figure 51c), shows that a significant fraction of combustion products reach a distance of 20 m, whereas the scenario with $D_v = D_d = 0.9$ m and $L_d = 6$m (Figure 51a), shows only a small fraction of combustion products at 20 m. Hence, a more severe explosion propagation is obtained as the vent area decreases and duct length increases.

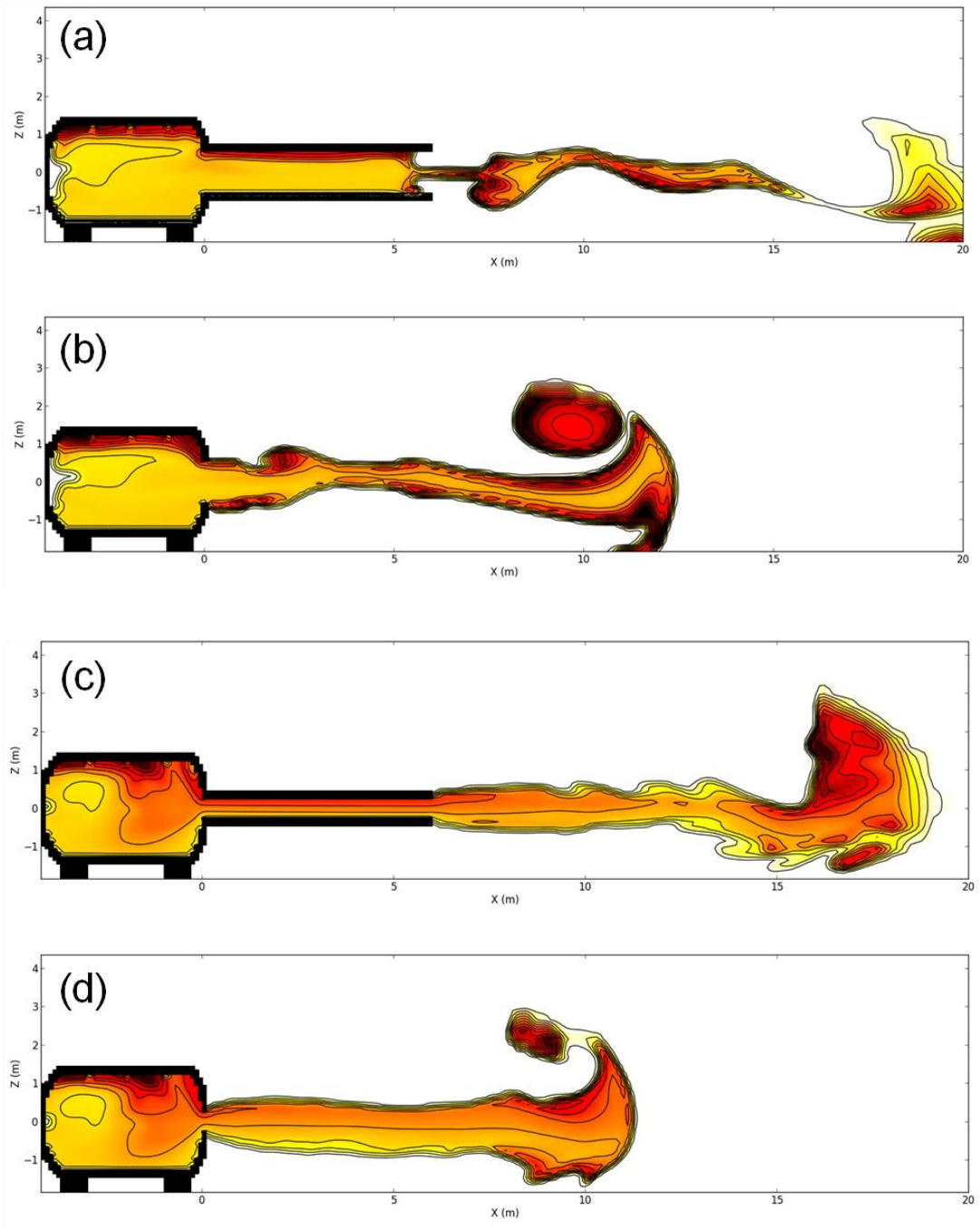

Figure 51. Vented dust explosions simulated with DESC, flame represented by mass fraction of combustion products (a) and (b) $D_v = D_d = 0.9$ m, $L_d = 0$ or 6 m, respectively. (c) and (d) $D_v = D_d = 0.5$ m, $L_d = 0$ or 6 m, respectively.

6.7.2. *Effects of ignition position on P_{red}*

The effect of the ignition position on P_{red} was analyzed by changing the ignition position in steps of 0.5m along the center line of the vessel (x axis) for a single scenario: $D_v = D_d = 1.1$ m and $L_d = 16$ m. Figure 52 shows how P_{red} is reduced as the ignition position is moved toward the vent opening. These results indicate a limitation in current prediction methods that do not account for the effect of ignition position, and generally consider center ignition the worst-case scenario.

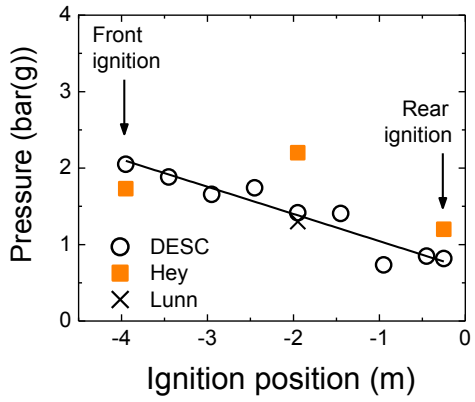

Figure 52. Influence of ignition location on P_{red} for coal dust explosions in an 18.5 m^3 vessel. Ignition position relative to position of burst disc. Configurations with $L_d = 16$ m and $D_v = D_d = 1.1$ m.

6.7.3. *Effects of dust cloud reactivity and homogeneity on P_{red}*

Figure 53a illustrates the effect of varying the reactivity of the mixture, for three values of the correction factor C_L, as well as the effect of igniting homogeneous *vs.*

dispersed dust cloud. The more reactive mixture, C_L = 1.5, or homogeneous dust clouds, led to an overestimation of P_{red} relative to experimental values, whereas C_L = 1.0 led to an underestimation. In accordance with previous studies [81, 275], the recommended value for the correction factor C_L is approximately 1.25 for 0.1 m grid cells.

6.7.4. Effects of grid resolution on P_{red}

Figure 53b illustrates how increased spatial resolution yield more conservative results for longer vent ducts. For D_d = 1.1 m the 0.1 m grid resolution should in principle be sufficient according to current grid guidelines for DESC, but the results indicate that finer resolution is required to capture phenomena such as secondary explosions in the duct. However, it is not obvious that the moderate increase in P_{red} for the finer grid resolution justifies the significant increase in computational cost.

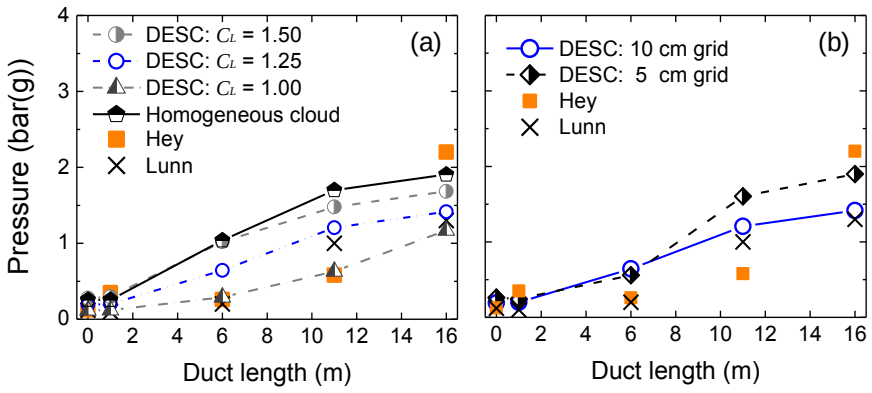

Figure 53. Effects of L_d on P_{red} for coal dust explosions in an 18.5 m^3 vessel, $D_v = D_d$ = *1.1* m and center ignition: (a) influence of cloud reactivity and homogeneity and (b) grid resolution.

6.7.5. *Effects of duct geometry configuration on P_{red}*

Figure 54 and 55 illustrate the effects of L_d on P_{red} when $D_d > D_v$. Although three of the guidelines, FM Global, VDI 3673 and EN 14491, assume $D_v = D_d$ for such configurations, the experimental results show appreciable differences in P_{red}. Figure 54 shows that experimental and simulated P_{red} values for scenarios with $A_d/A_v < 2$ are lower than the values for scenarios with $A_d/A_v = 1$. Thus, D_d should be slightly larger than D_v for optimal protection of the equipment. On the other hand, when D_d is significantly larger than D_v, *i.e.*, $A_d/A_v > 2$, the simulations do not capture the effect of the vent duct on the reduced pressure. As shown in Figure 55, the value of P_{red} predicted by DESC is not significantly influenced by L_d, leading to an underestimation relative to experimental data. Unfortunately, the experimental results are not very conclusive, since there is no clear trend between P_{red} and L_d [249].

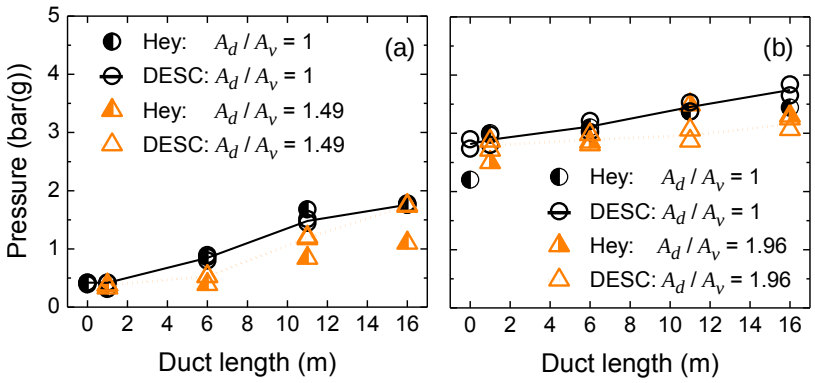

Figure 54. Effect D_d and L_d on P_{red} for coal dust explosions ($A_d/A_v \leq 2$).

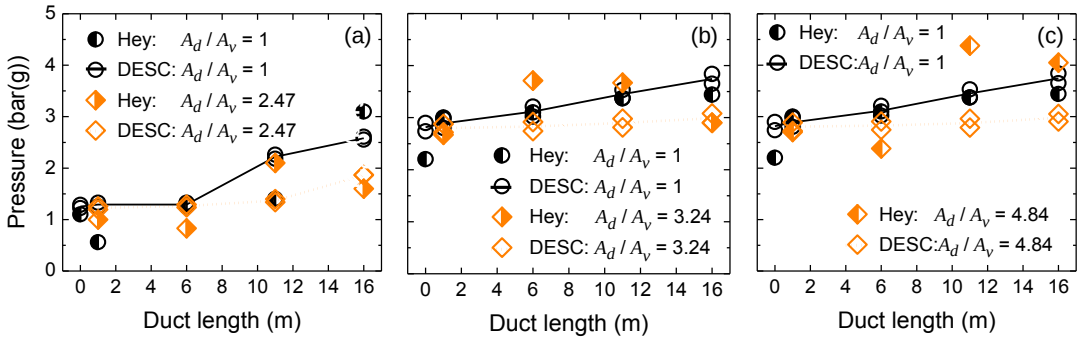

Figure 55. Effect D_d and L_d on P_{red} for coal dust explosions ($A_d/A_v > 2$).

Previous research on both gas and dust explosions have shown that the pressure developed during vented explosions depend more strongly on A_v than A_d [287]. This explains the conservative results obtained by the guidelines when assuming D_d is no larger than D_v. It is therefore recommended to perform P_{red} predictions assuming $D_v = D_d$ when $A_d/A_v > 2$.

6.7.6. Effects of obstructions in the duct on P_{red}

Figure 56 illustrate the effect of introducing obstructions in the duct, such as a bend or a pressure panel. Figure 56 shows good agreement between P_{red} predictions obtained with DESC and experimental results for scenarios with $D_v = D_d = 1.1$ m. The reduced explosion pressure obtained without duct ($P_{red,0}$) is higher for scenarios with D_v and D_d equal to 0.5 m, compared to scenarios with D_v and D_d equal to 1.1 m. Figure 57 shows that L_d has a moderate effect on P_{red} when $P_{red,0}$ is higher than 3 bar(g). This may be explained by the reduction in combustible material inside the vessel by the time the vent opens [288].

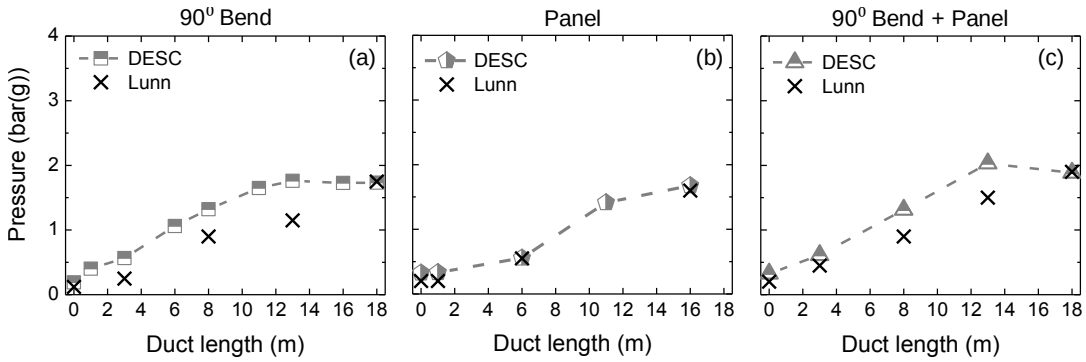

Figure 56. Effect on P_{red} for coal dust explosions vented through obstructed ducts. Scenarios with center ignition and $D_v = D_d = 1.1$ m. (a) Effect of one 90º bend at 1 m before the exit, (b) one panel ($P_{Stat} = 0.2$ bar) and (c) combined effect of bend and panel.

Figure 57 summarizes results from scenarios with $D_v = D_d = 0.5$ m. The increase in P_{red} when introducing a bend in the vent duct is well predicted, while the increment in P_{red} given by the panel ($P_{Stat} = 0.5$ bar) is underpredicted. In order to verify the effect of the inertia given by the panel weight, two simulations ($D_v = D_d = 0.5$ m, $L_d = 1$ m, $P_{Stat} = 0.5$ bar) were performed with a panel of negligible weight and a panel with specific mass 10 kg/m^2. However, P_{red} was not affected. Similar results have been observed in gas explosions [271]. Although the opening time is increased for the heavier panel, P_{red} seems to be dominated by other parameters, such as the cloud turbulence [271]. Figure 57 also shows that the combined effect of a vent panel ($P_{Stat} = 0.5$ bar) and a bend is underestimated by DESC for the smallest duct diameter ($D_d = 0.5$ m).

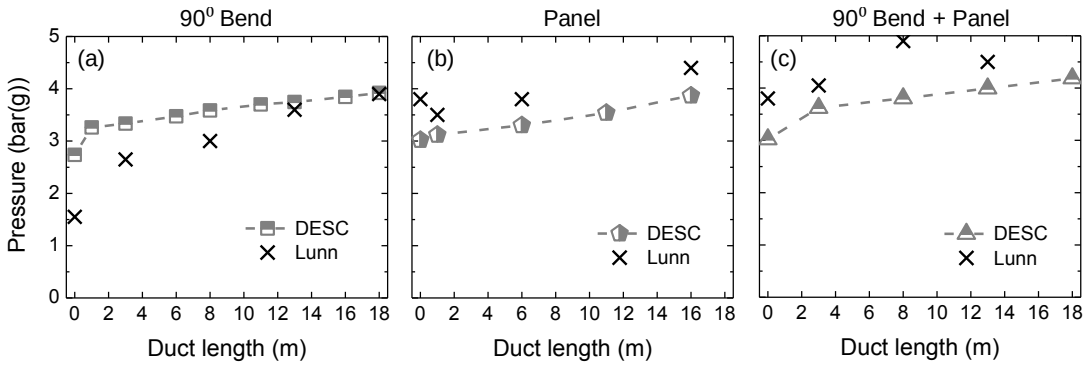

Figure 57. Effect on P_{red} for coal dust explosions vented through obstructed ducts. Scenarios with center ignition and $D_v = D_d = 0.5$ m. (a) Effect of one 90⁰ bend at 1 m before the exit, (b) one panel ($P_{Stat} = 0.2$ bar) and (c) combined effect of bend and panel.

6.8. DESC model evaluation

Figure 58 summarizes the simulated results from all the scenarios presented in Figure 47-50 and Figure 54-55. Although the CFD simulations tend to overpredict P_{red} compared to data from Lunn for certain scenarios (*i.e.,* C*: $D_v = D_d = 0.5$ m), the predictions obtained with DESC are generally in good agreement with experimental data for most ignition locations and duct sizes. The simulated results are quite similar to the results obtained by Hey [249], but up to a factor of two higher than data reported by Lunn for the same experimental conditions [44]. Hey reported typical variations in measured P_{red} values of about 0.3 bar(g) for a given scenario, whereas results from Hey and Lunn may differ with more than one bar for the same experimental configuration.

The relatively poor repeatability of the experimental series may have several explanations, such as delayed opening of valves, differences in dispersion nozzles or ignition sources, variations in particle size distribution, humidity or volatile content of the coal dust samples, and jet ignition or quenching effects taking place in the duct. Future experimental campaigns should therefore aim at more detailed documentation of the experimental procedures, and measurements of other variables than pressure, such as flame arrival times, dust concentrations, and turbulence parameters [275].

The simulations underpredict P_{red} for some scenarios with an area ratio larger than two, $A_d / A_v > 2$. As discussed in section 3.4, it is likely that the 0.1 m grid resolution is too coarse to capture the effect of secondary explosions in the duct. Clark *et al.,* [289] proposed a model for coal flame acceleration where an increase in duct diameter increases the turbulent Reynolds number and leads to enhanced flame accelerations. Kasmani *et al.,* [290] applied this explanation to justify a significant increase in pressure for certain vented gas explosions with rear ignition and $A_d / A_v = 3.8$.

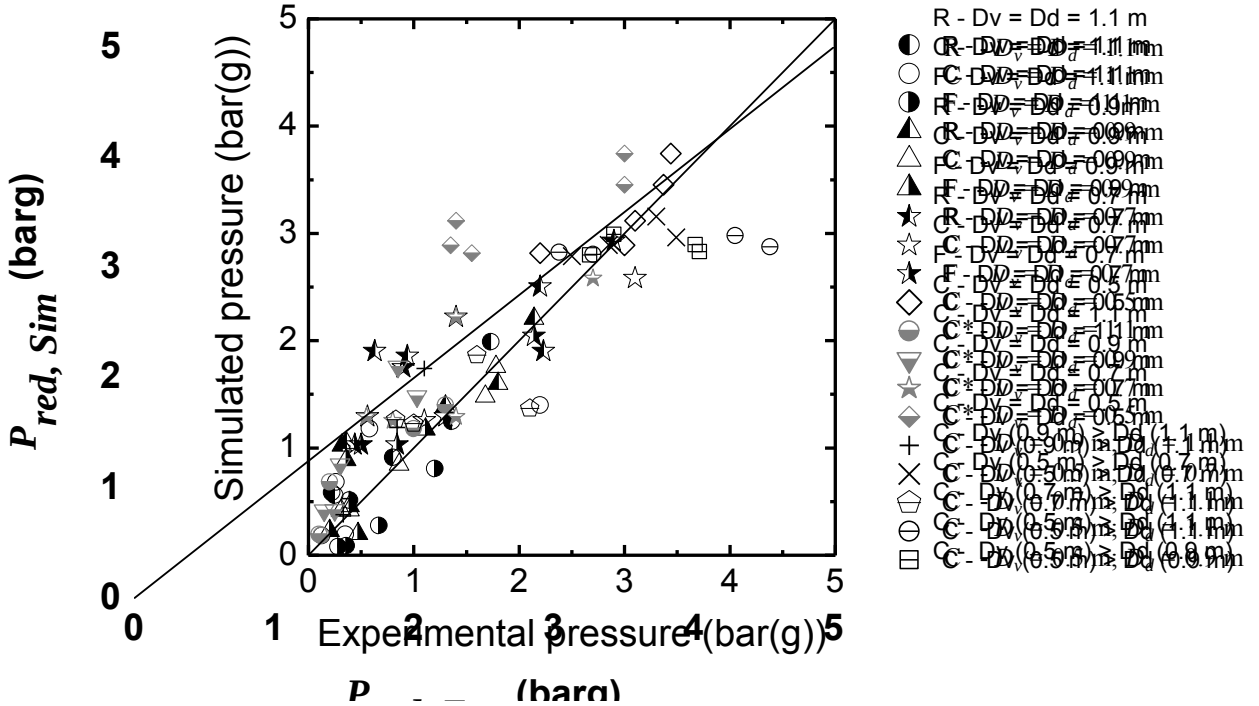

Figure 58. Comparison of simulated and experimental results for experiments reported by Hey [249] for rear (R), center (C) and front (F) ignition, and by Lunn [44] for center (C*) ignition.

It is also possible that inherent limitations in the modeling of particle-laden flows result in an improper representation of the turbulent dust cloud inside the vent duct at the time the turbulent flame from the vessel enters the duct. However, the experimental data does not provide the necessary information required to pursue this analysis further. Although a more realistic representation of particle-laden flow and turbulent flame propagation in dust clouds may improve the results, the poor repeatability of large-scale dust explosion experiments represents an inherent limitation with respect to further validation. Access to measured pressure-time histories would also be useful, since it is

not straightforward to draw unambiguous conclusions based on single-point data, such as P_{red} values for selected scenarios. Recent experiments in a specially designed flame acceleration tube for dust explosions may prove useful for identifying future model improvement [79].

6.9. Conclusions

Vented dust explosions in an 18.5 m^3 vessel equipped with vent ducts of varying length and diameter were simulated with the CFD code DESC. Most of the simulated results are in good agreement with experimental data. The reduced overpressure P_{red} increases systematically with increasing duct length L_d, and closed-end ignition represents the worst case scenario. DESC underpredicts P_{red} when the cross section of the duct A_d is more than twice the cross section A_v of the vent, and increased grid resolution is required for resolving secondary explosions in the duct. The simulations capture the effect of obstructions in the duct, such as bends or pressure panels.

The correlations in the guidelines tend to underestimate the effect of L_d on P_{red} when the ignition source is located in the closed end of the vessel. Both VDI 3673 and EN 14491 overestimate P_{red} in configurations with large vent diameters. The same correlations are less conservative for smaller vent areas, especially when L_d exceeds a critical length L_c. The significant spread in experimental results poses a challenge for the development of empirical correlations for use in standards and guidelines, and knowledge about the approach adopted for addressing this uncertainty is crucial when selecting appropriate safety factors for design of explosion protection systems.

Neither experiments nor simulations support the concept of a critical duct length, as prescribed in EN 14491 and VDI 3673. There is a definite need for further research in this area, and it is foreseen that the most fruitful approach entails a combination of detailed experiments at laboratory scale to characterize fundamental combustion properties for dust-air suspensions, CFD simulations that utilize empirically determined combustion parameters, and repeated large-scale experiments of high quality for model validation.

.

CHAPTER VII

CONCLUSIONS AND FUTURE WORK

7.1. Conclusions

This dissertation reports the effect of particle size and crystalline level on the combustion behavior of particulated solids. Two components were the main focus of this investigation: combustible dusts and explosion inhibitor agents. In **Chapter I**, the problem statement introduced some flaws and possible alternatives to overcome problems in process safety for dust handling industries. **Chapter II** provides background on the parameters affecting the initiation and propagation of dust explosions.

Chapter III describes the design, assembly and automatization of a 36 L dust explosion vessel useful to perform controlled dust explosion experiments. Significant efforts were devoted to ensure reliable data and safe operation. During the equipment calibration, the pre-ignition turbulence was manipulated to reproduce the K_{St} results from calibrated equipment (*i.e.,* 20 L and 1 m^3 vessel). A 2^k experimental design approach was employed to select the equipment operation conditions. In order to obtain an estimate of the turbulence decay inside the 36 L vessel, computational fluid dynamic (CFD) simulations were utilized. Despite the differences in size, shape, dispersion system, and operating conditions, the 36 L vessel was able to reproduce results from calibrated equipment. Furthermore, the estimations of the laminar burning velocity

using experimental results obtained from the 20 L and 36 L vessels were in very good agreement.

Chapter IV is devoted to investigating the effect of size polydispersity (σ_D) on the explosion severity and ignition sensitivity of aluminum dust. Series of dust samples of varying σ_D at a fixed D_{50} were systematically prepared. Experimental results from the 36 L vessel and a MIKE3 demonstrated that broader particle size distributions (*i.e.,* higher σ_D) exhibited a considerably higher explosion risk. It was experimentally confirmed that D_{50} is inadequately related to the real hazard potential of aluminum dust. In contrast, the Sauter mean diameter ($D_{3,2}$) provided a better correlation between particle size and the explosion parameters.

In **Chapter V**, the effect of particle size and crystallinity on the effectiveness of different inhibitors was explored. Two compounds were proposed as potential explosion inhibitors: ammonium phosphate dibasic (DPA, $(NH_4)_2HPO_4$) and zirconium phosphate (α-ZrP, $Zr(HPO_4)_2 \cdot H_2O$). Ammonium phosphate monobasic (MAP, $NH_4H_2PO_4$) was utilized as reference. MAP and DAP were fractionated at different sizes, and α-ZrP was synthesized at varying size and crystallinity. Mixtures containing cornstarch and each inhibitor were analyzed using DSC, TGA and the 36 L dust explosion vessel. Experimental results confirmed the crucial role of particle size on improving the inhibitor rate of heat absorption. As observed, an intermediate α-ZrP crystalline level having a gradual water release benefits the inhibitor performance. DAP presented the highest inhibition efficiency due to the release of large amount of ammonia during its endothermic decomposition. On the other hand, MAP presented a reduced inhibition

efficiency due to the lower amount of ammonia released. Surprisingly, MAP switches the onset of the exothermic reaction to a lower temperature, suggesting that this material accelerates the initial decomposition of the combustible dust. In agreement with the experimental results, a simplified model revealed a critical diameter below which the inhibitor efficiency is significantly improved.

Finally, **Chapter VI** reports the application of computational fluid dynamics (CFD) simulations for the prediction of overpressures caused from coal dust explosions vented through ducts. Existing standards and guidelines for the design of explosion protection systems compile empirical correlations that are usually limited to simple isolated scenarios. This work demonstrates that the Dust Explosion Simulation Code (DESC) is useful to simulate complex geometries commonly found in dust handling industries. By extrapolating the data obtained in a 20 L vessel, the evolution of vented dust explosions through ducts was successfully predicted. The analysis was particularly focused on the adverse effects caused by flow restrictions in vent ducts. Critical parameters, including ignition position, geometric configuration of the vent duct, and obstructions of outflow such as bends and panels were investigated. Comparison between simulated and experimental results was also useful to identify potential improvements in available guidelines.

7.2. Future work

The methodology used to study the effect of size polydispersity on explosion characteristics can be extended to different median particle size, polydispersity values, surface chemistry, and chemical composition. For instance, in Figure 25, (Chapter IV),

the y-intercept of the correlations between $(dP/dt)_{ex}V^{1/3}$ and σ_D may increase with particle size. Additionally, the reported trends can change as the correlations are extrapolated for mixtures outside the stated polydispersity range. The $(dP/dt)_{ex}V^{1/3}$ values of aluminum samples with high σ_D may exhibit a plateau region with minor dependency with σ_D.

The characterization of aluminum dust samples having bimodal distributions can quantitatively demonstrate the contribution of fine particles during a dust explosion. Bimodal distribution samples can be prepared by systematically mixing powders having a particle size of 1 and 15 μm. Experimental K_{St} and *MIE* values will allow reveal when the fine particles will possess a dominant effect during a dust explosion.

The understanding of the parameters affecting the evolution of dust layers into dust clouds is essential to improve current models used to predict the likelihood of secondary dust explosions [291-293]. As mentioned in section 2.5.4, inter-particle forces play an important role on the formation of dust clouds. Therefore, the systematic study of parameters affecting the these inter-particle forces (*e.g.,* inter-particles contact area, roughness and surface chemistry [8]) will elucidate alternatives to increase the energy required to lift a set of particles from a dust deposit and reduce the probability of dust cloud formation.

The morphology of the particles affects flowability [7], effective surface area and consequently material explosiveness [294]. Thomas *et al.,* [294] reported differences in ignition sensitivity of lycopodium particles having similar particle size but different morphology, reticulated and rugulose. The increased ignition frequency in reticulated

particles was attributed to increments on particles' surface area [294]. The relation between the particle morphology and the explosion characteristics can be explored by using combustible dusts with same chemical structure but different shape and surface area. For instance, the morphology of pharmaceutical products such as ibuprofen (iso-butyl-propanoic-phenolic acid), and niacin (nicotinic acid, pyridine-3-carboxylic acid) can be manipulated to forge their shape in a reproducible way [295]. Ibuprofen [296] and niacin [297] dusts can be re-crystallized into rod and plate-like shapes, using different solvents. Depending on the effective surface area, different explosion behavior would be expected. These experimental results can provide guidance to moderate the dust explosion risks by processing the dusts in their less hazardous forms.

Chapter V reveals the parameters affecting the efficiency of DAP ($(NH_4)_2HPO_4$) and α-ZrP as dust explosion inhibitors. These results provide guidance for the synthesis of more efficient inhibitors. For instance, α-ZrP can be intercalated with compounds of superior heat absorption such as DAP. The increased surface area would improve DAP rate of heat absorption during a dust explosion event, while the α-ZrP matrix would offer elevated thermal stability in a fire event.

REFERENCES

[1] R.K. Eckhoff, Dust explosions in the process industries, Third ed., Gulf Professional Publishing, Amsterdam, 2003.

[2] CSB, Investigation Report. Combustible Dust Hazard Study, U.S Chemical Safety and Hazard Investigation Board, 2006, pp. 1-108.

[3] United States. Dept. of Agriculture. Office of the Special Coordinator for Grain Elevator Safety, and Security. Prevention of dust explosions in grain elevators: an achievable goal: a task force report, Office of the Special Coordinator for Grain Elevator Safety and Security, Department of Agriculture, 1980.

[4] P.R. Amyotte, M.J. Pegg, F.I. Khan, M. Nifuku, T. Yingxin, Moderation of dust explosions, Journal of Loss Prevention in the Process Industries, 20 (2007) 675-687.

[5] F.S. Lai, D.W. Garrett, L.T. Fan, Study of mechanisms of grain dust explosion as affected by particle size and composition. I. Review of literature, Powder Technology, 32 (1984) 193-202.

[6] L.J. Jallo, M. Schoenitz, E.L. Dreizin, R.N. Dave, C.E. Johnson, The effect of surface modification of aluminum powder on its flowability, combustion and reactivity, Powder Technology, 204 (2010) 63-70.

[7] L.X. Liu, I. Marziano, A.C. Bentham, J.D. Litster, E.T.White, T. Howes, Effect of particle properties on the flowability of ibuprofen powders, International Journal of Pharmaceutics, 362 (2008) 109-117.

[8] Q. Li, V. Rudolph, B. Weigl, A. Earl, Interparticle van der Waals force in powder flowability and compactibility, International Journal of Pharmaceutics, 280 (2004) 77-93.

[9] N.S. Berchane, K.H. Carson, A.C. Rice-Ficht, M.J. Andrews, Effect of mean diameter and polydispersity of PLG microspheres on drug release: Experiment and theory, International Journal of Pharmaceutics, 337 (2007) 118-126.

[10] M.J. Andrews, N.S. Berchane, K.H. Carson, A.C. Rice-Ficht, Investigation of drug release from biodegradable PLG microspheres: experiments and theory, Report No. LA-UR-07-0642., Los Alamos National Laboratory (LANL), 2007.

[11] X. Han, C. Ghoroi, D. To, Y. Chen, R. Davé, Simultaneous micronization and surface modification for improvement of flow and dissolution of drug particles, International Journal of Pharmaceutics, 415 (2011) 185-195.

[12] F.J. Maile, G. Pfaff, P. Reynders, Effect pigments—past, present and future, Progress in Organic Coatings, 54 (2005) 150-163.

[13] B. Innes, T. Tsuzuki, H. Dawkins, J. Dunlop, G. Trotter, M.R. Nearn, P.G. McCormick, Nanotechnology and the cosmetic chemist, Cosmetics, Aerosols and Toiletries in Australia, 15 (2002) 10-24.

[14] K. Jayaraman, S. Chakravarthy, R. Sarathi, Accumulation of nano-aluminium during combustion of composite solid propellant mixtures, Combustion, Explosion, and Shock Waves, 46 (2010) 21-29.

[15] J. Yang, A. Sliva, A. Banerjee, R.N. Dave, R. Pfeffer, Dry particle coating for improving the flowability of cohesive powders, Powder Technology, 158 (2005) 21-33.

[16] C. Cesana, R. Siwek, Operating Instruction 20 L apparatous 6.0, Adolf Kuhner AG, CH-4127 Birsfelden, Switzerland, 2011.

[17] W. Bartknecht, Dust explosions, course, prevention, protection, Springer-Verlag, Berlin, 1981.

[18] R.K. Eckhoff, Dust Explosions in the Process Industries (Third Edition), Gulf Professional Publishing, Burlington, 2003.

[19] A. Di Benedetto, P. Russo, P. Amyotte, N. Marchand, Modelling the effect of particle size on dust explosions, Chemical Engineering Science, 65 (2010) 772-779.

[20] T. Skjold, Review of the DESC project, Journal of Loss Prevention in the Process Industries, 20 (2007) 291-302.

[21] O.L. T Skjold, and O Hansen, Possibilities, limitations and the way ahead for dust explosion modelling, IChemE, symposium Series No. 151 (2006).

[22] M. Alderliesten, Mean Particle Diameters. Part III: An Empirical Evaluation of Integration and Summation Methods for Estimating Mean Particle Diameters from Histogram Data, Particle & Particle Systems Characterization, 19 (2002) 373-373.

[23] G. Baudry, S. Bernard, P. Gillard, Influence of the oxide content on the ignition energies of aluminium powders, Journal of Loss Prevention in the Process Industries, 20 (2007) 330-336.

[24] K.L. Cashdollar, Coal dust explosibility, Journal of Loss Prevention in the Process Industries, 9 (1996) 65-76.

[25] K. Chatrathi, J. Going, Dust deflagration extinction, Process Safety Progress, 19 (2000) 146-153.

[26] A.G. Dastidar, P.R. Amyotte, J. Going, K. Chatrathi, Flammability limits of dusts: Minimum inerting concentrations, Process Safety Progress, 18 (1999) 56-63.

[27] A. Dastidar, P. Amyotte, Determination of Minimum Inerting Concentrations for Combustible Dusts in a Laboratory-Scale Chamber, Process Safety and Environmental Protection, 80 (2002) 287-297.

[28] P.R. Amyotte, Solid inertants and their use in dust explosion prevention and mitigation, Journal of Loss Prevention in the Process Industries, 19 (2006) 161-173.

[29] F. Tamanini, Explosion suppression for Industrial applications, Solid Propellant Gas Generator Workshop, Gaithersburg, MD, 1995.

[30] P.E. Moore, Suppressants for the control of industrial explosions, Journal of Loss Prevention in the Process Industries, 9 (1996) 119-123.

[31] Q.H. Wang, H. Wen, Q.S. Wang, J.H. Sun, Inhibiting effect of Al(OH)(3) and Mg(OH)(2) dust on the explosions of methane-air mixtures in closed vessel, Science China Technological Sciences, 55 (2012) 1371-1375.

[32] T. Choi, S. Rahimian, R.H. Essenhigh, Studies in coal dust explosions: Influence of additives on extinction of high intensity coal dust flames, Symposium (International) on Combustion, 21 (1988) 345-355.

[33] C. Liu, Y. Yang, Effects of [alpha]-zirconium phosphate aspect ratio on the properties of polyvinyl alcohol nanocomposites, Polymer Testing, 28 (2009) 801-807.

[34] J. Alongi, A. Frache, Flame retardancy properties of [alpha]-zirconium phosphate based composites, Polymer Degradation and Stability, 95 (2010) 1928-1933.

[35] H. Lu, C.A. Wilkie, M. Ding, L. Song, Thermal properties and flammability performance of poly (vinyl alcohol)/[alpha]-zirconium phosphate nanocomposites, Polymer Degradation and Stability, 96 (2011) 885-891.

[36] J. Jiang, J. Li, J. Hu, D. Fan, Effect of nitrogen phosphorus flame retardants on thermal degradation of wood, Construction and Building Materials, 24 (2010) 2633-2637.

[37] P.J. Davies, A.R. Horrocks, A. Alderson, The sensitisation of thermal decomposition of ammonium polyphosphate by selected metal ions and their potential for improved cotton fabric flame retardancy, Polymer Degradation and Stability, 88 (2005) 114-122.

[38] G. Camino, L. Costa, L. Trossarelli, Study of the mechanism of intumescence in fire retardant polymers: Part V - Mechanism of formation of gaseous products in

the thermal degradation of ammonium polyphosphate, Polymer Degradation and Stability, 12 (1985) 203-211.

[39] G.A. Lunn, A.M. Nicol, P.D. Collins, N.R. Hubbard, Effects of vent ducts on the reduced pressures from explosions in dust collectors, Journal of Loss Prevention in the Process Industries, 11 (1998) 109-121.

[40] K.N. Palmer, Recent advances in the relief venting of dust explosions Journal of Hazardous Materials, 1 (1975) 97-111.

[41] P. Russo, A. Di Benedetto, Effects of a Duct on the Venting of Explosions - Critical Review, Process Safety and Environmental Protection, 85 (2007) 9-22.

[42] Ural, Dust Explosion Venting through Ducts, in: 39th Annual Loss Prevention Symposium, Atlanta, USA, 2005.

[43] R. Siwek, K. van Wingerden, Dust explosion venting: EN Standard 14491 vs VDI guideline 3673, Chemical Engineering Transactions, 9 (2006) 71-76.

[44] G. Lunn, D. Crowhurst, M. Hey, The effect of vent ducts on the reduced explosion pressures of vented dust explosions, Journal of Loss Prevention in the Process Industries, 1 (1988) 182-196.

[45] K. van Wingerden, T. Skjold, Vented dust explosions: a review of the effect of vent ducts, supported by CFD calculations, in: 8th International Symposium on Hazards, Prevention and Mitigation of Industrial Explosions (ISHPMIE), Yokohama, Japan, 2010

[46] F. Tamanini, J.V. Valiulis, Improved guidelines for the sizing of vents in dust explosions, Journal of Loss Prevention in the Process Industries, 9 (1996) 105-118.

[47] R.K. Eckhoff, Dust explosion research. State-of-the-art and outstanding problems, Journal of Hazardous Materials, 35 (1993) 103-117.

[48] S. Mannan, and Frank P. Lees, Lee's loss prevention in the process industries: hazard identification, assessment, and control, 2005.

[49] P.R. Amyotte, R.K. Eckhoff, Dust explosion causation, prevention and mitigation: An overview, Journal of Chemical Health and Safety, 17 (2009) 15-28.

[50] P. van der Wel, Ignition and propagation of dust explosions, Delft University Doctoral Thesis, Netherlands, 1993.

[51] I. Glassman, R. Yetter, Combustion, Fourth ed., Elsevier, 2008.

[52] P. van der Wel, S. Lemkowitz, B. Scarlett, K. van Wingerden, A Study of Particle Factors Affecting Dust Explosions, Particle & Particle Systems Characterization, 8 (1991) 90-94.

[53] N.M. Paul Amyotte, Almerinda Di Benedetto, Paola Russo Influence of particles size and ethylene admixture on polyethylene dust explosions, in: 7th International Symposium Hazard Prevention Mitigation of Industrial Explosion, St. Petersburgh, 2008, pp. 103–113.

[54] S. Long, F. Cao, S. Wang, L. Sun, J. Pang, Y.-p. Sun, Combustion Characteristics of Polyethylene and Coal Powder at High Temperature, Journal of Iron and Steel Research, International, 15 (2008) 6-9.

[55] ISO-6184/1, Explosion protection systems - part 1: Determination of explosion indices of combustible dusts in air, International Standards Organization, 1985.

[56] A.E. Dahoe, J.F. Zevenbergen, S.M. Lemkowitz, B. Scarlett, Dust explosions in spherical vessels: The role of flame thickness in the validity of the 'cube-root law', Journal of Loss Prevention in the Process Industries, 9 (1996) 33-44.

[57] ASTM, E1226-10, Standard Test Method for Explosibility of Dust Clouds, ASTM International, 2010.

[58] ASTM, E1226-00, Standard Test Method for Pressure and Rate of Pressure Rise for Combustible Dusts, ASTM International, 2005.

[59] ASTM, E2019-03, Standard Test Method for Minimum Ignition Energy of a Dust Cloud in Air, ASTM International, 2007.

[60] ASTM, E1515-07, Standard Test Method for Minimum Explosible Concentration of Combustible Dusts, ASTM International, 2007.

[61] ASTM, E1491-06, Standard Test Method for Minimum Autoignition Temperature of Dust Clouds, ASTM International, 2006.

[62] ASTM, E2021-09, Standard Test Method for Hot-Surface Ignition Temperature of Dust Layers, ASTM International, 2009.

[63] R.G. Abdel-Gayed, D. Bradley, M. Lawes, Turbulent Burning Velocities: A General Correlation in Terms of Straining Rates, Proceedings of the Royal Society of London. Series A, Mathematical and Physical Sciences, 414 (1987) 389-413.

[64] T. Skjold, B.J. Arntzen, O.R. Hansen, O.J. Taraldset, I.E. Storvik, R.K. Eckhoff, Simulating Dust Explosions with the First Version of DESC, Process Safety and Environmental Protection, 83 (2005) 151-160.

[65] A.E. Dahoe, Dust Explosions: a Study of Flame Propagation, Delft University Doctoral Thesis, Netherlands, 2000.

[66] C.J. Ralls, G.E.B. Tremeer, Equations for the determination of burning velocity in a spherical constant volume vessel, Combustion and Flame, 7 (1963) 51-61.

[67] P.R. Santhanam, V.K. Hoffmann, M.A. Trunov, E.L. Dreizin, Characteristics of Aluminum Combustion Obtained from Constant-Volume Explosion Experiments, Combustion Science and Technology, 182 (2010) 904-921.

[68] D. Bradley, Z. Chen, J.R. Swithenbank, Burning rates in turbulent fine dust-air explosions, Symposium (International) on Combustion, 22 (1989) 1767-1775.

[69] D. Bradley, A. Mitcheson, Mathematical solutions for explosions in spherical vessels, Combustion and Flame, 26 (1976) 201-217.

[70] T. Skjold, Selected aspects of turbulence and combustion in 20-litre explosion vessels, University of Bergen Master Thesis, Bergen, 2003.

[71] A.E. Dahoe, L.P.H. de Goey, On the determination of the laminar burning velocity from closed vessel gas explosions, Journal of Loss Prevention in the Process Industries, 16 (2003) 457-478.

[72] M. Silvestrini, B. Genova, F.J. Leon Trujillo, Correlations for flame speed and explosion overpressure of dust clouds inside industrial enclosures, Journal of Loss Prevention in the Process Industries, 21 (2008) 374-392.

[73] A.A. Pekalski, Theoretical and experimental study on explosion safety of hydrocarbons oxidation at elevated conditions: Relevance for safe design and operation of industrial processes, Delft University Doctoral Thesis, Netherlands, 2004.

[74] C.M. Luijten, E. Doosje, J.A. van Oijen, L.P.H. de Goey, Impact of dissociation and end pressure on determination of laminar burning velocities in constant volume combustion, International Journal of Thermal Sciences, 48 (2009) 1206-1212.

[75] A.E. Dahoe, Laminar burning velocities of hydrogen–air mixtures from closed vessel gas explosions, Journal of Loss Prevention in the Process Industries, 18 (2005) 152-166.

[76] M. Kolbe, Laminar burning velocity measurements of stabilized aluminum dust flames, in: Concordia University, Quebec, Canada, 2001.

[77] S. Goroshin, I. Fomenko, J.H.S. Lee, Burning velocities in fuel-rich aluminum dust clouds, Symposium (International) on Combustion, 26 (1996) 1961-1967.

[78] Y.K. Pu, J. Jarosinski, V.G. Johnson, C.W. Kauffman, Turbulence effects on dust explosions in the 20-liter spherical vessel, Symposium (International) on Combustion, 23 (1991) 843-849.

[79] T. Skjold, K. Olsen, D. Castellanos, R.K. Eckhoff, Experimental and Numerical Investigation of Constant Volume Dust and Gas Explosions in a 3.6 meter Flame

Acceleration Tube, in: IX International Symposium on Hazard, Prevention and Mitigation of Industrial Explosions, Cracow, Poland, 2012.

[80] A. Garcia, Study of hybrid mixture explosions, University Degri Studi di Napoli Federico II, Doctoral Thesis, Italy, 2010.

[81] T. Skjold, Review of the DESC project, Journal of Loss Prevention in the Process Industries, 20 (2007) 291-302.

[82] B.J. Arntzen, Modelling of turbulence and combustion for simulation of gas explosions in complex geometries, in: Applied mechanics, thermodynamics and fluid dynamics, Norwegian University of Science and Technology, Trondheim, 1998.

[83] A.E. Dahoe, R.S. Cant, B. Scarlett, On the Decay of Turbulence in the 20-liter Explosion Sphere, Flow, Turbulence and Combustion, 67 (2001) 159-184.

[84] A.E. Dahoe, R.S. Cant, M.J. Pegg, B. Scarlett, On the transient flow in the 20-liter explosion sphere, Journal of Loss Prevention in the Process Industries, 14 (2001) 475-487.

[85] A.E. Dahoe, K. van del Nat, M. Braithwaite, B. Scarlett, On the sensitivity of the maximum explosion pressure of a dust deflagration to turbulence, KONA, 19, (2001) 178-195.

[86] R.K. Eckhoff, Influence of initial and explosion-induced turbulence on dust explosions in closed and vented vessels research at CMI, Powder Technology, 71 (1992) 181-187.

[87] W.B.C. Heij, On the application of Laser Doppler Anemometry to the Transient Flow inside the Standard 20-litre Explosion Sphere, Delft University Master Thesis, Netherlands, 1998.

[88] R.K. Eckhoff, Influence of initial and explosion-induced turbulence on dust explosions in large vented silo cells, Safety Science, 16 (1993) 511-525.

[89] A. Di Benedetto, A. Garcia-Agreda, P. Russo, R. Sanchirico, Combined Effect of Ignition Energy and Initial Turbulence on the Explosion Behavior of Lean Gas/Dust-Air Mixtures, Industrial & Engineering Chemistry Research, 51 (2011) 7663-7670.

[90] G. Zhen, W. Leuckel, Influence of transient injection induced turbulence flow on gas and dust explosions in a closed vessel, in: J.J. Mewis, H.J. Pasman, E.E.D. Rademaeker (Eds.) Loss Prevention and Safety Promotion in Process Industries, 1995 a.

[91] G. Zhen, W. Leuckel, Determination of Dust Dispersion Induced Turbulence and its Influence on Dust Explosions, Combustion Science, 113-114 (1996) 629-639.

[92] G. Zhen, W. Leuckel, Effects of ignitors and turbulence on dust explosions, Journal of Loss Prevention in the Process Industries, 10 (1997) 317-324.

[93] P.R. Amyotte, S. Chippett, M.J. Pegg, Effects of turbulence on dust explosions, Progress in Energy and Combustion Science, 14 (1988) 293-310.

[94] P.R. Amyotte, M.J. Pegg, Lycopodium dust explosions in a Hartmann bomb: effects of turbulence, Journal of Loss Prevention in the Process Industries, 2 (1989) 87-94.

[95] D.B. Mercer, P.R. Amyotte, D.J. Dupuis, M.J. Pegg, A. Dahoe, W.B.C. de Heij, J.F. Zevenbergen, B. Scarlett, The influence of injector design on the decay of pre-ignition turbulence in a spherical explosion chamber, Journal of Loss Prevention in the Process Industries, 14 (2001) 269-282.

[96] Y. Kang Pu, J. Jarosinski, C. Sheng Tai, C. William Kauffman, M. Sichel, The investigation of the feature of dispersion induced turbulence and its effects on dust explosions in closed vessels, Symposium (International) on Combustion, 22 (1989) 1777-1787.

[97] F. Hauert, A. Vogl, S. Radandt, Dust cloud characterization and its influence on the pressure-time-history in silos, Process Safety Progress, 15 (1996) 178-184.

[98] Y. Pu, J. Podfilipski, J. Jarosiński, Constant Volume Combustion of Aluminum and Cornstarch Dust in Microgravity, Combustion Science and Technology, 135 (1998) 255-267.

[99] P. van der Wel, J. van Veen, S. Lemkowitz, B. Scarlett, C.. van Wingerden, An interpretation of dust explosion phenomena on the basis of time scales, Powder Technology, 71 (1992) 207-215.

[100] C.W. Kauffman, S.R. Srinath, F.I. Tezok, J.A. Nicholls, M. Sichel, Turbulent and accelerating dust flames, Symposium (International) on Combustion, 20 (1985) 1701-1708.

[101] C.T. Cloney, R.C. Ripley, P.R. Amyotte, F.I. Khan, Quantifying the Effect of Strong Ignition Sources on Particle Preconditioning and Distribution in the 20 L Chamber, in: 9th International Symposium on Hazard, Prevention and Mitigation of Industrial Explosions (ISHPMIE), Cracow, Poland, 2012.

[102] J.E. Going, K. Chatrathi, K.L. Cashdollar, Flammability limit measurements for dusts in 20 L and 1 m^3 vessels, Journal of Loss Prevention in the Process Industries, 13 (2000) 209-219.

[103] M. Hertzberg, K.L. Cashdollar, C.P. Lazzara, The limits of flammability of pulverized coals and other dusts, Symposium (International) on Combustion, 18 (1981) 717-729.

[104] M. Hertzberg, K.L. Cashdollar, I.A. Zlochower, Flammability limits measurements for dusts and gases: Ignition energy requirements and pressure dependences, in: 21st Symposium (International) on Combustion, Pittsburgh, PA, 1986, pp. 303-313.

[105] K.L. Cashdollar, K. Chatrathi, Minimum Explosible Dust Concentrations Measured in 20 L and 1 m^3 Chambers, Combustion Science and Technology, 87 (1993) 157-171.

[106] K.L. Cashdollar, E.S. Weiss, N.B. Greninger, K. Chatrathi, Laboratory and large-scale dust explosion research, Plant/Operations Progress, 11 (1992) 247-255.

[107] C. Proust, A. Accorsi, L. Dupont, Measuring the violence of dust explosions with the "20 l sphere" and with the standard "ISO 1 m^3 vessel": Systematic comparison and analysis of the discrepancies, Journal of Loss Prevention in the Process Industries, 20 599-606.

[108] A.S. Parker, H.C. Hottel, Industrial & Engineering Chemistry, 28 (1936).

[109] R. Mitsui, T. Tanaka, Simple Models of Dust Explosion. Predicting Ignition Temperature and Minimum Explosive Limit in Terms of Particle Size, Industrial & Engineering Chemistry Process Design and Development, 12 (1973) 384-389.

[110] A.L. Kuhl, M. Boiko, Ignition of Aluminum Particles and Clouds, in: Energetic Materials: High Performance, Insensitive Munitions and Zero Pollution, 2010, pp. 29.21–29.11.

[111] R.S. Lee, D.F. Aldis, D.W. Garrett, F.S. Lai, Improved diagnostics for determination of minimum explosive concentration, ignition energy and ignition temperature of dusts, Powder Technology, 31 (1982) 51-62.

[112] F.-D. Tang, A.J. Higgins, S. Goroshin, Effect of discreteness on heterogeneous flames: Propagation limits in regular and random particle arrays, Combustion Theory and Modelling, 13 (2009) 319-341.

[113] C.V. Mashuga, D.A. Crowl, Flammability zone prediction using calculated adiabatic flame temperatures, Process Safety Progress, 18 (1999) 127-134.

[114] C.V. Mashuga, D.A. Crowl, Problems with identifiying a standard procedure for determining K_G values for flammable vapors, Journal of Loss Prevention in the Process Industries, 13 (2000) 369-376.

[115] D. Razus, V. Brinzea, M. Mitu, C. Movileanu, D. Oancea, Temperature and pressure influence on maximum rates of pressure rise during explosions of propane–air mixtures in a spherical vessel, Journal of Hazardous Materials, 190 (2011) 891-896.

[116] M.I. Hassan, K.T. Aung, G.M. Faeth, Measured and predicted properties of laminar premixed methane/air flames at various pressures, Combustion and Flame, 115 (1998) 539-550.

[117] A. Van Maaren, D.S. Thung, L.R.H. De Goey, Measurement of Flame Temperature and Adiabatic Burning Velocity of Methane/Air Mixtures, Combustion Science and Technology, 96 (1994) 327-344.

[118] C.K. Law, Combustion physics, Cambridge University Press, 2006.

[119] K.L. Cashdollar, I. A. Zlochower, G.M. Green, R.A. Thomas, M. Hertzberg, Flammability of methane, propane, and hydrogen gases, Journal of Loss Prevention in the Process Industries, 13 (2000) 327-340.

[120] D. Razus, V. Brinzea, M. Mitu, D. Oancea, Temperature and pressure influence on explosion pressures of closed vessel propane–air deflagrations, Journal of Hazardous Materials, 174 (2010) 548-555.

[121] S. Callé, L. Klaba, D. Thomas, L. Perrin, O. Dufaud, Influence of the size distribution and concentration on wood dust explosion: Experiments and reaction modelling, Powder Technology, 157 (2005) 144-148.

[122] M. Hertzberg, I.A. Zlochower, K.L. Cashdollar, Volatility model for coal dust flame propagation and extinguishment, Symposium (International) on Combustion, 21 (1988) 325-333.

[123] R. Soundararajan, P.R. Amyotte, M.J. Pegg, Explosibility hazard of iron sulphide dusts as a function of particle size, Journal of Hazardous Materials, 51 (1996) 225-239.

[124] O. Dufaud, M. Traoré, L. Perrin, S. Chazelet, D. Thomas, Experimental investigation and modelling of aluminum dusts explosions in the 20 L sphere, Journal of Loss Prevention in the Process Industries, 23 (2010) 226-236.

[125] M. Nifuku, S. Koyanaka, H. Ohya, C. Barre, M. Hatori, S. Fujiwara, S. Horiguchi, I. Sochet, Ignitability characteristics of aluminium and magnesium dusts that are generated during the shredding of post-consumer wastes, Journal of Loss Prevention in the Process Industries, 20 (2007) 322-329.

[126] A. Di Benedetto, P. Russo, Thermo-kinetic modelling of dust explosions, Journal of Loss Prevention in the Process Industries, 20 (2007) 303-309.

[127] W. Peukert, Trends in solids process engineering (in German), Chemie Ingenieur Technik 66(10), (1996) 1254-1263

[128] Q. Li, B. Lin, W. Li, C. Zhai, C. Zhu, Explosion characteristics of nano-aluminum powder-air mixtures in 20 L spherical vessels, Powder Technology, 212 (2011) 303-309.

[129] O. Dufaud, et al., Ignition and explosion of nanopowders: something new under the dust, Journal of Physics: Conference Series, 304 (2011) 012076.

[130] P. Escot Bocanegra, D. Davidenko, V. Sarou-Kanian, C. Chauveau, I. Gökalp, Experimental and numerical studies on the burning of aluminum micro and nanoparticle clouds in air, Experimental Thermal and Fluid Science, 34 (2010) 299-307.

[131] Y. Huang, G.A. Risha, V. Yang, R.A. Yetter, Combustion of bimodal nano/micron-sized aluminum particle dust in air, Proceedings of the Combustion Institute, 31 (2007) 2001-2009.

[132] S.P. Mokkapati, Simulation of particle agglomeration using dissipative particle dynamics, Texas A&M University Doctoral Thesis, College Station, 2006.

[133] R. Zeng, B. Rand, Particle size distribution, powder agglomerates and their effects on sinterability of ultrafine alumina powders, Journal of Materials Science Technology, 16 (2000) 393-396

[134] H. Yamamoto, A. Suganuma, Dispersion of airborne aggregated dust by an orifice, International Chemical Engineering, 24 (1984) 338–345.

[135] R.K. Eckhoff, Influence of dispersibility and coagulation on the dust explosion risk presented by powders consisting of nm-particles, Powder Technology, 239 (2013) 223-230.

[136] H.-C. Wu, H.-J. Ou, D.-J. Peng, H.-C. Hsiao, C.-Y. Gau, T.-S. Shih, Dust E plosion Characteristics of Agglomerated 35 nm and 100 nm Aluminum Particles, International Journal of Chemical Engineering, 2010 (2010) 1-6.

[137] J. Bouillard, A. Vignes, O. Dufaud, L. Perrin, D. Thomas, Ignition and explosion risks of nanopowders, Journal of Hazardous Materials, 181 (2010) 873-880.

[138] R.K. Eckhoff, Does the dust e plosion risk increase when moving from μm-particle powders to powders of nm-particles?, Journal of Loss Prevention in the Process Industries, 25 (2012) 448-459.

[139] T. Köhler, H. Schubert, Influence of the Particle Size Distribution on the flow behaviour of fine powders, Particle & Particle Systems Characterization, 8 (1991) 101-104.

[140] M. Traoré, O. Dufaud, L. Perrin, S. Chazelet, D. Thomas, Dust explosions: How should the influence of humidity be taken into account?, Process Safety and Environmental Protection, 87 (2009) 14-20.

[141] L. Perrin, A. Laurent, V. Falk, O. Dufaud, M. Traore, Dust and electrostatic hazards, could we improve the current standards?, Journal of Loss Prevention in the Process Industries 20 (2007) 207–217.

[142] A. Dastidar, P. Amyotte, J. Going, K. Chatrathi, Inerting of coal dust explosions in laboratory- and intermediate-scale chambers, Fuel, 80 (2001) 1593-1602.

[143] K.L. Cashdollar, M. Hertzberg, I.A. Zlochower, Effect of volatility on dust flammability limits for coals, gilsonite, and polyethylene, Symposium (International) on Combustion, 22 (1989) 1757-1765.

[144] A.D. Craven, M.G. Foster, Dust explosion prevention. Determination of critical oxygen concentration by vertical tube method, Combustion and Flame, 11 (1967) 408-414.

[145] E. Rolf K, Partial inerting: an additional degree of freedom in dust explosion protection, Journal of Loss Prevention in the Process Industries, 17 (2004) 187-193.

[146] G. Ackroyd, M. Bailey, R. Mullins, The effect of reduced oxygen levels on the electrostatic ignition sensitivity of dusts, Journal of Physics: Conference Series, 301 (2011) 012034.

[147] F.K. Sweis, C.G. Sinclair, The effect of particle size on the maximum permissible oxygen concentration to prevent dust explosions, Journal of Hazardous Materials, 10 (1985) 59-71.

[148] R.K. Eckhoff, Dust Explosion Prevention and Mitigation, Status and Developments in Basic Knowledge and in Practical Application, International Journal of Chemical Engineering, 2009 (2009).

[149] M. Glor, Electrostatic ignition hazards in the process industry, Journal of Electrostatics, 63 (2005) 447-453.

[150] Ø. Larsen, J.H. Hagen, K. van Wingerden, Ignition of dust clouds by brush discharges in oxygen enriched atmospheres, Journal of Loss Prevention in the Process Industries, 14 (2001) 111-122.

[151] J. Gummer, G.A. Lunn, Ignitions of explosive dust clouds by smouldering and flaming agglomerates, Journal of Loss Prevention in the Process Industries, 16 (2003) 27-32.

[152] T. Abbasi, S.A. Abbasi, Dust explosions-Cases, causes, consequences, and control, Journal of Hazardous Materials, 140 (2007) 7-44.

[153] P. Holbrow, S. Andrews, G.A. Lunn, Dust explosions in interconnected vented vessels, Journal of Loss Prevention in the Process Industries, 9 (1996) 91-103.

[154] P. Holbrow, G.A. Lunn, A. Tyldesley, Dust explosion protection in linked vessels: guidance for containment and venting, Journal of Loss Prevention in the Process Industries, 12 (1999) 227-234.

[155] G.A. Lunn, P. Holbrow, S. Andrews, J. Gummer, Dust explosions in totally enclosed interconnected vessel systems, Journal of Loss Prevention in the Process Industries, 9 (1996) 45-58.

[156] J. Amrogowicz, W. Kordylewski, Effectiveness of dust explosion suppression by carbonates and phosphates, Combustion and Flame, 85 (1991) 520-522.

[157] A.G. Dastidar, P.R. Amyotte, M.J. Pegg, Factors influencing the suppression of coal dust explosions, Fuel, 76 (1997) 663-670.

[158] I. Hartmann, J. Nagy, Venting dust explosions, Industrial and Engineering Chemistry, 49 (1957) 1734-1740.

[159] R.K. Eckhoff, Sizing of dust explosion vents in the process industries: Advances made during the 1980s, Journal of Loss Prevention in the Process Industries, 3 (1990) 268-279.

[160] VDI 3673, Pressure Release of Explosions. Verein Deutcher Ingenieure, 2002.

[161] NFPA 68, Standard on Explosion Protection by Deflagration Venting, National Fire Protection Association, 2007.

[162] R. Siwek, 20 L laborapparatur fur die bestimmung der explosionskenngrossen brennbarer staube, Technical University of Winterthur, Winterthur, Switzerland, 1977.

[163] G. Zhen, W. Leuckel, Influence of transient injection induced turbulence flow on gas and dust explosions in a closed vessel, J.J. Mewis, H.J. Pasman, E.E.D. Rademaeker (Eds.) Loss Prevention and Safety Promotion in the Process Industries, Elsevier Science B.V, 1995.

[164] G. Zhen, W. Leuckel, The dynamic flow condition of dust dispersion induced turbulence, in: Proceedings of 10th Symposium of Turbulent Shear Flows, 1995, pp. 7-12.

[165] P. Middha, O.R. Hansen, J. Grune, A. Kotchourko, CFD calculations of gas leak dispersion and subsequent gas explosions: Validation against ignited impinging hydrogen jet experiments, Journal of Hazardous Materials, 179 (2010) 84-94.

[166] S.R. Hanna, O.R. Hansen, S. Dharmavaram, FLACS CFD air quality model performance evaluation with Kit Fox, MUST, Prairie Grass, and EMU observations, Atmospheric Environment, 38 (2004) 4675-4687.

[167] D. Montgomery, Design and Analysis of Experiments, Fifth ed., Arizona State University, New York, 1997.

[168] G.E.P. Box, J.S. Hunter, The 2k-p Fractional Factorial Designs Part I, Technometrics, 3 (1961) 311-351.

[169] P.R. Amyotte, K.J. Mintz, M.J. Pegg, Y.-H. Sun, K.I. Wilkie, Effects of methane admixture, particle size and volatile content on the dolomite inerting requirements of coal dust, Journal of Hazardous Materials, 27 (1991) 187-203.

[170] A. Kühner, Final Report. Calibration-Round-Robin (CaRo 00/01), Switzerland, 2001.

[171] A. Garcia-Agreda, A. Di Benedetto, P. Russo, E. Salzano, R. Sanchirico, Dust/gas mixtures explosion regimes, Powder Technology, 205 (2011) 81-86.

[172] O. Kalejaiye, P.R. Amyotte, M.J. Pegg, K.L. Cashdollar, Effectiveness of dust dispersion in the 20 L Siwek chamber, Journal of Loss Prevention in the Process Industries, 23 (2010) 46-59.

[173] T. Skjold, B.J. Arntzen, O.R. Hansen, I.E. Storvik, R.K. Eckhoff, Simulation of dust explosions in complex geometries with experimental input from standardized tests, Journal of Loss Prevention in the Process Industries, 19 (2006) 210-217.

[174] M. Kearns, Development and applications of ultrafine aluminium powders, Materials Science and Engineering A, 375-377 (2004) 120-126.

[175] Y. Zhang, H. Ye, H. Liu, K. Han, Preparation and characterisation of aluminium pigments coated with silica for corrosion protection, Corrosion Science, 53 (2011) 1694-1699.

[176] R.J. Gill, C. Badiola, E.L. Dreizin, Combustion times and emission profiles of micron-sized aluminum particles burning in different environments, Combustion and Flame, 157 (2010) 2015-2023.

[177] Y. Huang, G.A. Risha, V. Yang, R.A. Yetter, Effect of particle size on combustion of aluminum particle dust in air, Combustion and Flame, 156 (2009) 5-13.

[178] M. Beckstead, Correlating Aluminum Burning Times, Combustion, Explosion, and Shock Waves, 41 (2005) 533-546.

[179] R. Friedman, A. Maček, Ignition and combustion of aluminium particles in hot ambient gases, Combustion and Flame, 6 (1962) 9-19.

[180] D.C. May, D.L. Berard, Fires and explosions associated with aluminum dust from finishing operations, Journal of Hazardous Materials, 17 (1987) 81-88.

[181] CSB, Investigation Report. Aluminum Dust Explosion, Hayes Lemmerz International-Huntington, Inc., U.S Chemical Safety and Hazard Investigation Board, 2005.

[182] N. Kalkert, H.G. Schecker, Theoretische Überlegungen zum Einfluß der Teilchengröße auf die Mindestzündenergie von Stäuben, Chemie Ingenieur Technik, 51 (1979) 1248-1249.

[183] R. Siwek, C. Cesana, Ignition behavior of dusts: Meaning and interpretation, Process Safety Progress, 14 (1995) 107-119.

[184] T. Matsuda, M. Yashima, M. Nifuku, H. Enomoto, Some aspects in testing and assessment of metal dust explosions, Journal of Loss Prevention in the Process Industries, 14 (2001) 449-453.

[185] C. Cesana, R. Siwe, Operating Manual MIKE 3, Kuhner AG, CH-4127 Birsfelden, Switzerland, 2010.

[186] A. Janes, J. Chaineaux, D. Carson, P.A. Le Lore, MIKE 3 versus HARTMANN apparatus: Comparison of measured minimum ignition energy (MIE), Journal of Hazardous Materials, 152 (2008) 32-39.

[187] O. Dufaud, A. Vignes, F. Henry, L. Perrin, J. Bouillard, Ignition and Explosion of nanopowders: something new under the dust, in: Nanosafe 2010, International Conference on Safe Production and Use of Nanomaterials, Journal of Physics: Conference Series 304, 2011.

[188] R.A. Ogle, L.D. Chen, J.K. Beddow, P.B. Butler, An Investigation of Aluminum Dust Explosions, Combustion Science and Technology, 61 (1988) 75-99.

[189] M.A. Trunov, M. Schoenitz, E.L. Dreizin, Ignition of Aluminum Powders Under Different Experimental Conditions, Propellants, Explosives, Pyrotechnics, 30 (2005) 36-43.

[190] M. Bidabadi, N. Moalleni, A. Shabani, M. Abdous, Analysis of size distribution and ignition temperature effects on flame speeds in aluminium dust clouds, in: Proceedings of the Institution of Mechanical Engineers, Part G. Journal of Aerospace Engineering, 2010.

[191] J.H.S. Lee, F. Zhang, R. Knystautas, Propagation mechanisms of combustion waves in dust-air mixtures, Powder Technology, 71 (1992) 153-162.

[192] L.V. Boichuk, V.G. Shevchuk, A.I. Shvets, Flame Propagation in Two-Component Aluminum–Boron Gas Suspensions, Combustion, Explosion, and Shock Waves, 38 (2002) 651-654.

[193] A. Clearfield, R.H. Blessing, J.A. Stynes, New crystalline phases of zirconium phosphate possessing ion-exchange properties, Journal of Inorganic and Nuclear Chemistry, 30 (1968) 2249-2258.

[194] L. Sun, W.J. Boo, H.-J. Sue, A. Clearfield, Preparation of [small alpha]-zirconium phosphate nanoplatelets with wide variations in aspect ratios, New Journal of Chemistry, 31 (2007) 39-43.

[195] P. Oleszczak, R. Klemens, Mathematical modelling of dust-air mixture explosion suppression, Journal of Loss Prevention in the Process Industries, 19 (2006) 187-193.

[196] K. Van Wingerden, T. Skjold, Simulation of Explosion Suppression Systems and Extinguishing Barriers Using the CFD Code Desc, in: AIChe Procedings, 2008.

[197] P. Kosinski, Numerical investigation of explosion suppression by inert particles in straight ducts, Journal of Hazardous Materials, 154 (2008) 981-991.

[198] T. Mitani, A flame inhibition theory by inert dust and spray, Combustion and Flame, 43 (1981) 243-253.

[199] K. Kuang, W.K. Chow, X. Ni, D. Yang, W. Zeng, G. Liao, Fire suppressing performance of superfine potassium bicarbonate powder, Fire and Materials, (2010).

[200] A.G. Dastidar, P.R. Amyotte, Using Calculated Adiabatic Flame Temperatures to Determine Dust Explosion Inerting Requirements, Process Safety and Environmental Protection, 82 (2004) 142-155.

[201] N. Kuai, J. Li, Z. Chen, W. Huang, J. Yuan, W. Xu, Experiment-based investigations of magnesium dust explosion characteristics, Journal of Loss Prevention in the Process Industries, 24 (2011) 302-313.

[202] J.E. Dolan, P.B. Dempster, The suppression of methane–air ignitions by fine powders, Journal of Applied Chemistry, 5 (1955) 510-517.

[203] M. Krasnyansky, Prevention and suppression of explosions in gas-air and dust-air mixtures using powder aerosol-inhibitor, Journal of Loss Prevention in the Process Industries, 19 (2006) 729-735.

[204] Q. Liu, Y. Hu, C. Bai, M. Chen, Methane/coal dust/air explosions and their suppression by solid particle suppressing agents in a large-scale experimental tube, Journal of Loss Prevention in the Process Industries, 26 (2011) 310-316.

[205] Z. Chen, B. Fan, X. Jiang, Suppression effects of powder suppressants on the explosions of oxyhydrogen gas, Journal of Loss Prevention in the Process Industries, 19 (2006) 648-655.

[206] K.-S. Huang, K.-C. Pan, C.-N. Perng, Pyrolysis of cellulose-Effect of Diammonium phosphate on fire retardation, J. Chinese Chem. Soc. , 22 (1975) 57-68.

[207] M.R. Ricciardi, V. Antonucci, M. Zarrelli, M. Giordano, Fire behavior and smoke emission of phosphate - based inorganic fire-retarded polyester resin, Fire and Materials, 36 (2012) 203-215.

[208] R. Zhang, Y. Hu, Solvothermal synthesis of organically modified α-zirconium phosphate-based polystyrene nanocomposites and thermal stability, Journal of Applied Polymer Science, 122 (2011) 593-598.

[209] D. Yang, Y. Hu, L. Song, S. Nie, S. He, Y. Cai, Catalyzing carbonization function of [alpha]-ZrP based intumescent fire retardant polypropylene nanocomposites, Polymer Degradation and Stability, 93 (2008) 2014-2018.

[210] D.-Y. Wang, X.-Q. Liu, J.-S. Wang, Y.-Z. Wang, A.A. Stec, T.R. Hull, Preparation and characterisation of a novel fire retardant PET/[alpha]-zirconium phosphate nanocomposite, Polymer Degradation and Stability, 94 (2009) 544-549.

[211] R. Zhang, Y. Hu, B. Li, Z. Chen, W. Fan, Studies on the preparation and structure of polyacrylamide/α-zirconium phosphate nanocomposites, Journal of Materials Science, 42 (2007) 5641-5646.

[212] C. Di Blasi, C. Branca, A. Galgano, Effects of Diammonium Phosphate on the Yields and Composition of Products from Wood Pyrolysis, Industrial & Engineering Chemistry Research, 46 (2006) 430-438.

[213] M.d.C.C. Lucena, A.E. V. de Alencar, S.E. Mazzeto, S.d.A. Soares, The effect of additives on the thermal degradation of cellulose acetate, Polymer Degradation and Stability, 80 (2003) 149-155.

[214] T. Hirata, K.E. Werner, Thermal analysis of cellulose treated with boric acid or ammonium phosphate in varied oxygen atmospheres, Journal of Applied Polymer Science, 33 (1987) 1533-1556.

[215] K. Kishore, K. Mohandas, Mechanistic studies on the action of ammonium phosphate on polymer fire retardancy, Combustion and Flame, 43 (1981) 145-153.

[216] F. Laoutid, L. Bonnaud, M. Alexandre, J.M. Lopez-Cuesta, P. Dubois, New prospects in flame retardant polymer materials: From fundamentals to nanocomposites, Materials Science and Engineering: Reports, 63 (2009) 100-125.

[217] T. Kashiwagi, F. Du, J.F. Douglas, K.I. Winey, R.H. Harris, J.R. Shields, Nanoparticle networks reduce the flammability of polymer nanocomposites, Nature Materials, 4 (2005) 928 - 933.

[218] D.J. Frurip, T. Elwell, Effective use of differential scanning calorimetry in reactive chemicals hazard evaluation, Process Safety Progress, 26 (2007) 51-58.

[219] L.F. Whiting, M.S. Labean, S.S. Eadie, Evaluation of a capillary tube sample container for differential scanning calorimetry, Thermochimica Acta, 136 (1988) 231-245.

[220] J. Pandey, N.K. Mohalik, R.K. Mishra, A. Khalkho, D. Kumar, V.K. Singh, Investigation of the Role of Fire Retardants in Preventing Spontaneous Heating of Coal and Controlling Coal Mine Fires, Fire Technology, (2012) 1-19.

[221] V. Babushok, W. Tsang, Influence of Phosphorus-Containing Fire Suppressants on Flame Propagation, in: International Conference on fire Research and Engineering (ICFRE3), 1999, pp. 257-267.

[222] H. Horacek, R. Grabner, Advantages of flame retardants based on nitrogen compounds, Polymer Degradation and Stability, 54 (1996) 205-215.

[223] C.C. Stephenson, A.C. Zettlemoyer, The Heat Capacity of Ammonium Dihydrogen Phosphate from 15 to 300°K. The Anomaly at the Curie Temperature, Journal of the American Chemical Society, 66 (1944) 1405-1408.

[224] J. Utomo, Y. Asakuma, N. Maynard, K. Maeda, K. Fukui, M.O. Tadé, Semi-batch reactive crystallisation of mono-ammonium phosphate: An experimental study, Chemical Engineering Journal, 156 (2010) 594-600.

[225] B.B. Luff, R.B. Reed, R.H. Nash, Low-temperature heat capacity and entropy of diammonium orthophosphate, Journal of Chemical & Engineering Data, 21 (1976) 418-419.

[226] A.F. Mejia, A. Diaz, S. Pullela, Y.-W. Chang, M. Simonetty, C. Carpenter, J.D. Batteas, M.S. Mannan, A. Clearfield, Z. Cheng, Pickering emulsions stabilized by amphiphilic nano-sheets, Soft Matter, 8 (2012) 10245-10253.

[227] W.D. Callister, D.G. Rethwisch, Materials science and engineering: an introduction, (2007) 571-619.

[228] D. Yang, Y. Hu, L. Song, S. Nie, S. He, Y. Cai, Catalyzing carbonization function of a-ZrP based intumescent fire retardant polypropylene nanocomposites, Polymer Degradation and Stability, 93 (2008) 2014-2018.

[229] A.A. Martí, J.L. Colón, Direct Ion E change of Tris(2,2‘-bipyridine)ruthenium(II) into an α-Zirconium Phosphate Framework, Inorganic Chemistry, 42 (2003) 2830-2832.

[230] J. Hexamer, Prevention of Dust Explosions and Fires in Malt Mills, Journal Franklin Institute, (1883) 200-206.

[231] D.J. Price, H.H. Brown, Dust explosions – theory and nature of, phenomena, causes and methods of prevention, Boston, 1922.

[232] R.V. Wheeler, Report on experiments into the means of preventing the spread of explosions of carbonaceous dusts, London, 1935.

[233] D. Matheson, Explosion relief on dust plants, in: Conference on Dust in Industry, Society of Chemical Industry, University of Leeds, 1948, pp. 125-127.

[234] J. Snoeys, J.E. Going, J.R. Taveau, Advances in Dust Explosion Protection Techniques: Flameless Venting, Procedia Engineering, 45 (2012) 403-413.

[235] P. Holbrow, Dust explosion venting of small vessels and flameless venting, Process Safety and Environmental Protection.

[236] J.E. Going, K. Chatrathi, Efficiency of flameless venting devices, Process Safety Progress, 22 (2003) 33-42.

[237] K.C. Brown, Dust explosions in factories: the protection of elevator casings by pressure relief vents, Safety in Mines Research Establishment, Research Report No. 22, Sheffield, (1951).

[238] S.L. Segalova, V.A. Resnik, Venting of gases through circular ducts in dust explosions, Russian, Teploenergetika, (1962) 19-22.

[239] M. Hattwig, Selected aspects of explosion venting, in: 2th Symposium on Loss Prevention and Safety Promotion in the Process Industries, 1977.

[240] M. Hattwig, Die VDI-Richtlinie 3673 “Druckentlastung von Staube plosionen” und besondere Probleme bei ihrer praktischen Anwendung, VDI-Berichte 304 (1978) 117-126.

[241] J.P. Pineau, J. Dangreaux, Efficacité des évents, Institut National de Recherche et de Sécurité, INRS Note 1005-83-76 (38-07) CDU 614.839, 191-202 (1976).

[242] J.P. Pineau, Explosions de poussières dans des enceintes a des canalisations, Sichere Handhabung brennbarer Staube, Nuremberg, (1983).

[243] J.P. Pineau, Dust explosions in vessels connected to ducts, VDI-Berichte 494 (1984) 67-80.

[244] A. Aellig, R. Gramlich, Einfluss von Ausblasrohren auf die Explosionsdruckentlastung, VDI-Berichte 494 Sichere Handhabung brennbarer Staube, (1984) 175-183.

[245] J.W. Kordvlewski, Influence of ducting on dust explosion venting, in: 3rd International Colloquium on Dust Explosions, Szczyrk, 1988.

[246] W. Kordvlewski, J. Wach, Influence of ducting on the explosion pressure, Combustion and Flame, 66 (1986) 77-79.

[247] W. Kordvlewski, J. Wach, Influence of ducting on the explosion pressure: small scale experiments, Combustion and Flame, 71 (1988) 51-61.

[248] D. Crowhurst, Small-scale dust explosions vented through ducts, in: 3rd International Colloquium on Dust Explosions, Szczyrk, 1988.

[249] M. Hey, Pressure relief of dust explosions through large diameter ducts and effects of changing the position of the ignition source, Journal of Loss Prevention in the Process Industries, 4 (1991) 217-222.

[250] G. Griesche, P. Wolf, H. Schliemann, Druckentlastung von Brandkohlenstaubexplosionen über Druckableitungsrohre, Neue Bergbautechnik, 20 (1990) 110-113.

[251] G. Griesche, Explosion venting: influence of venting devices at the end of the vent duct, in: 2nd World Seminar on the Explosion Phenomenon and on the Application of Explosion Protection Techniques in Practice, Flanders Expo, Gent, Belgium, 1996.

[252] P.S. Tonkin, C.F.J. Berlemont, Dust explosions in a large scale cyclone plant, Fire Research Note 942, Fire Research Station, (1972) pp. 41.

[253] S. Radandt, Staubexplosionen in Silos fur Nahrungsmittel, Futtermittel, Getreide und Ölsaaten, in: Symposium Heft 9, Berufsgenossenschaft Nahrungsmittel und Gaststatten, 1981, pp. 1-41.

[254] W. Bartknecht, Einfluss von Abblasrohren auf die Druckverstarkung in entlasteten kubischen und langgestreckten Behaltern mit homogener und inhomogener Staubverteilung bei spezieller Berucksichtigung von Wirbelschicht-Apparaturen, Freiburg, 1998, pp. 51.

[255] R. Siwek, Druckentlastung von Staubexplosionen beim pneumatischen Befüllen von Behältern, VDI-Berichte, 701 (1988) 529-567.

[256] R. Siwek, Einfluss von Ausblasrohren auf die Druckentlastung von Staubexplosionen, Staub Reinhaltung der Luft, 49 (1989) 327-331.

[257] R. Siwek, Dust explosion venting for dusts pneumatically conveyed into vessels, Plant & Operations Progress, 8 (1989) 129-140.

[258] R. Lautkaski, Duct venting of gas explosions, Research Report, VVT-R-02755-11, VVT Technical Research Centre of Finland, (2011) 179.

[259] R. Lautkaski, Duct venting of gas explosions: Revision of two proposed engineering correlations, Journal of Loss Prevention in the Process Industries, 25 (2012) 400-413.

[260] VDI 3673, Druckentlastung von Staubexplosionen, Verein deutscher Ingenieure, VDI Verlag GmbH, Düsseldorf, (1979).

[261] VDI 3673, Pressure Release of Explosions. Verein Deutcher Ingenieure (1994).

[262] J. Barton, Dust Explosion Prevention and Protection. A practical guide Institution of Chemical Engineers, Rugby, 2002.

[263] EN 14491, Dust explosion venting protective systems, European Standard, (2006).

[264] F. Tamanini, E.A. Ural, FMRC studies of parameters affecting the propagation of dust explosions, Powder Technology, 71 (1992) 135-151.

[265] F. Tamanini, The role of turbulence in dust explosions, Journal of Loss Prevention in the Process Industries, 11 (1998) 1-10.

[266] F. Tamanini, Scaling parameters for vented gas and dust explosions, Journal of Loss Prevention in the Process Industries, 14 (2001) 455-461.

[267] F. Tamanini, Dust explosion vent sizing - Current methods and future developments, in: 4th International symposium of hazards, prevention, and mitigation of industrial explosions, Bourges, France, 2002, pp. 31-44.

[268] F. Tamanini, Aspect Ratio Effects in Unvented and Vented Dust Explosions, in: 8th International Symposium on Hazards, Prevention and Mitigation of Industrial Explosions (ISHPMIE), Yokohama, Japan, 2010.

[269] F. Tamanini, Aspect ratio effects in unvented and vented dust explosions, Industrial and Engineering Chemistry Research, 51 (2012) 7636-7642.

[270] F. Tamanini, J.V. Valiulis, A correlation for the impulse produced by vented explosions, Journal of Loss Prevention in the Process Industries, 13 (2000) 277-289.

[271] S. Höchst, W. Leuckel, On the effect of venting large vessels with mass inert panels, Journal of Loss Prevention in the Process Industries, 11 (1998) 89-97.

[272] F. Tamanini, Aspect Ratio Effects in Unvented and Vented Dust Explosions, Industrial & Engineering Chemistry Research, 51 (2011) 7636-7642.

[273] F. Tamanini, Vent sizing in partial-volume deflagrations and its application to the case of spray dryers, Journal of Loss Prevention in the Process Industries, 9 (1996) 339-350.

[274] E.A. Ural, A simplified method for predicting the effect of ducts connected to explosion vents, Journal of Loss Prevention in the Process Industries, 6 (1993) 3-10.

[275] T. Skjold, Flame propagation in dust clouds: challenges for model validation, in: 8th International Symposium on Hazards, Prevention and Mitigation of Industrial Explosions (ISHPMIE), Yokohama, Japan, 2010.

[276] F.A. Williams, Past contributions and future problems in laminar and turbulent combustion. Lectures on applied mathematics in combustion, Physica 20 D. North-Holland, Amsterdam, (1986) 21-34.

[277] E.A. Ural, A Simplified Development of a unified dust explosion vent sizing formula, Process Safety Progress, 20 (2001) 136-144.

[278] E.A. Ural, A simplified development of a unified dust explosion vent sizing formula, in: 35th Annual Loss Prevention Symposium, Houston, USA, 2001.

[279] F. Tamanini, M. Fischer, Mixed mode venting of duct explosions, in: Fire and Explosion Hazards. 4th International Seminar, University of Ulster, Northern Ireland, United Kindom, 2004.

[280] F. Tamanini, Personal Communication (03-30-2012), 2012.

[281] B. Ponizy, J.C. Leyer, Flame dynamics in a vented vessel connected to a duct: 2. Influence of ignition site, membrane rupture, and turbulence, Combustion and Flame, 116 (1999) 272-281.

[282] R. Kasmani, G.E. Andrews, H.N. Phylaktou, S.K. Willacy, Influence of Static Burst Pressure and Ignition Position on Duct-Vented Gas Explosions, in: 5th International Seminar on Fire and Explosion Hazards, Edinburgh, UK, 2007, pp. 254-264.

[283] R. Kasmani, G.E. Andrews, H.N. Phylaktou, S.K. Willacy, Vented gas explosion in a cilindrical vessel with a vent duct, in: 3th European Combustion Meeting ECM 2007, 2007.

[284] G. Ferrara, A. Di Benedetto, E. Salzano, G. Russo, CFD analysis of gas explosions vented through relief pipes, Journal of Hazardous Materials, 137 (2006) 654-665.

[285] A. Tascón, P.J. Aguado, A. Ramírez, Dust explosion venting in silos: A comparison of standards NFPA 68 and EN 14491, Journal of Loss Prevention in the Process Industries, 22 (2009) 204-209.

[286] A. Tascón, Á. Ruiz, P.J. Aguado, Dust explosions in vented silos: Simulations and comparisons with current standards, Powder Technology, 208 (2011) 717-724.

[287] W. Kordylewski, J. Wach, Influence of ducting on explosion pressure: Small scale experiments, Combustion and Flame, 71 (1988) 51-61.

[288] V.V. Molkov, Venting of defragrations: dynamic of the process in systems with a duct and receiver, in: 4th International Symposium on Fire Safety Science, 1994, pp. 1245-1254.

[289] D.P. Clark, L.D. Smoot, Model of accelerating coal dust flames, Combustion and Flame, 62 (1985) 255-269.

[290] R. Kasmani, G.E. Andrews, H.N. Phylaktou, S.K. Willacy, Vented Explosions with a Vent Duct of Twice the Diameter of the Vent in a Vessel with an L/D of 2: Extremely Fast Turbulent Flames and High Overpressures in the Vent Duct, in: European Combustion Meeting, Vienna Austria, 2009.

[291] T. Skjold, Simulating the Effect of Release of Pressure and Dust Lifting on Coal Dust Explosions, in: Twenty-third International Colloquium on the Dynamics of Explosions and Reactive Systems (ICDERS), Poitiers, France, 2007.

[292] T. Skjold, Simplified modelling of explosion propagation by dust lifting in coal mines, in: Procedings on the 5th International Seminar on Fire and Explosion Hazards, Edinburgh, UK, 2007.

[293] K. Rudolph, Z. Przemyslaw, Experimental Investigation of Dust Lifting Delay, in: 21st ICDERS, Poitiers, France, 2007.

[294] G.O. Thomas, G. Oakley, J. Brenton, Influence of the morphology of lycopodium dust on its minimum ignition energy, Combustion and Flame, 85 (1991) 526-528.

[295] D. Winn, M.F. Doherty, Modeling crystal shapes of organic materials grown from solution, AIChE Journal, 46 (2000) 1348-1367.

[296] H. Cano, N. Gabas, J.P. Canselier, Experimental study on the ibuprofen crystal growth morphology in solution, Journal of Crystal Growth, 224 (2001) 335-341.

[297] E.M. Gonçalves, M.E. Minas da Piedade, Solubility of nicotinic acid in water, ethanol, acetone, diethyl ether, acetonitrile, and dimethyl sulfoxide, The Journal of Chemical Thermodynamics, 47 (2012) 362-371.

[298] E. Randeberg, Electric spark ignition of sensitive dust clouds in the sub 1 mJ range, University of Bergen Doctoral Thesis, Bergen, 2006.

[299] E. Randeberg, W. Olsen, R.K. Eckhoff, A new method for generation of synchronised capacitive sparks of low energy, Journal of Electrostatics, 64 (2006) 263-272.

[300] D. Crowl, J. Lovar, Chemical Process Safety. Fundamentals with Applications, Second ed., New, Prentice Hall TR, 2002.

APPENDIX A

36 L DUST EXPLOSION VESSEL DIMENSIONS

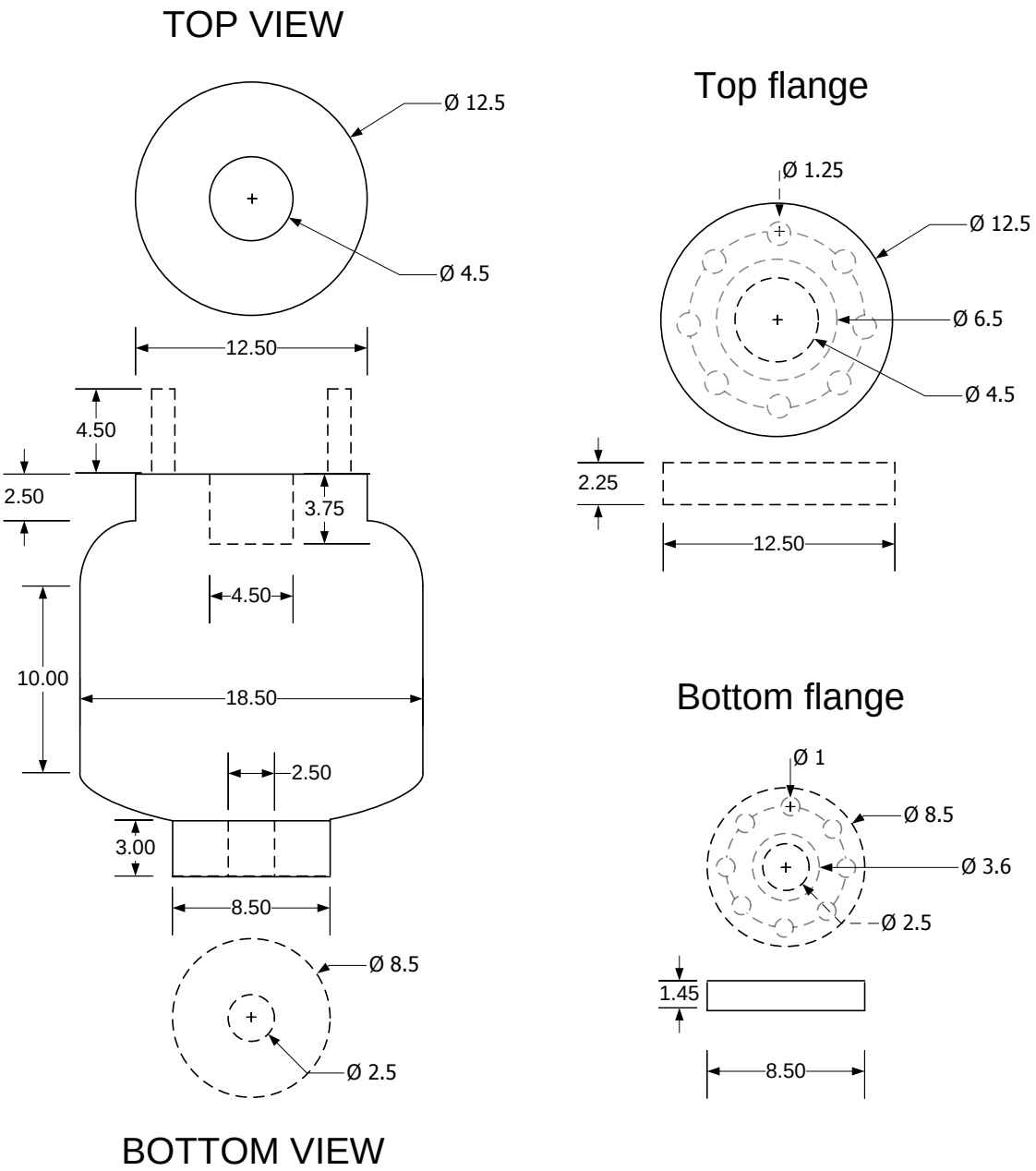

Figure A1. Dimensions of the 36 L Dust Explosion Equipment

APPENDIX B

PNEUMATIC VALVE ACTUATION DELAY TIME ANALYSIS

A pneumatic valve (Swagelok: SS-63TS12-33DCB-L1) was initially used to discharge air from the reservoir to the vessel to create the dust cloud during each test. This valve presented undesired actuation delays due to its pneumatic actuation mechanism. To evaluate V2 performance, an oscilloscope was connected to V2 signal from the control box and V2 signal from its position indicator. Table B1 provides details of the pneumatic valve actuation time. V2 actuation time resulted fairly precise but very inaccurate with respect the set point pulse. For this reason, V2 was replaced by an electric valve (ASCO: 8210G26) which does not require pressurized air to be activated. The selected electric valve has less movable parts that provide a better efficiency over time.

Table B1. Pneumatic valve actuation delay time analysis

Set point pulse (ms)	Reported by LabView (ms)	Oscilloscope		Precision error	Accuracy error	
		Control box (ms)	Position indicator (ms)			
75.0	75.1	75.2	75.8	2.0%	0.8 ms	1%
100.0	100.1	100.0	110.6	2.5%	10.6 ms	11%
200.0	200.1	200.2	222.4	1.8%	22.4 ms	11%
300.0	300.1	300.0	324.0	2.1%	24.0 ms	8.0%
400.0	400.1	400.0	424.6	2.5%	24.6 ms	6.0%

* Each reported value represents 10 trials average

APPENDIX C

SPARK GENERATOR

The electric spark generator provides around 50 mJ [298]. Due to the weak energy supplied, it should be used to ignite gas or hybrid (gas-dust) –air mixtures, rather than dust-air mixtures. Figures C1 and C2 show the electrical circuit board and the control box of the electrical spark generator, respectively. The system was built at the University of Bergen. The spark can be externally triggered using Labview, by connecting it to the chemical igniters output signal in the 36 L control box.

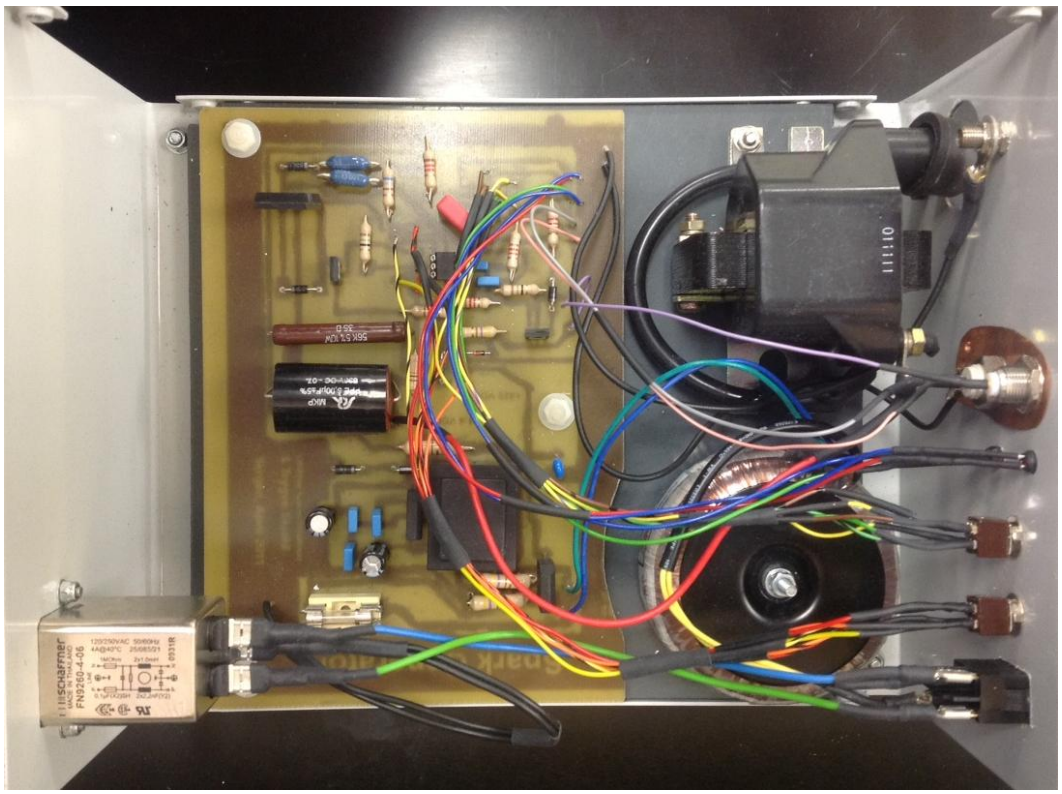

Figure C1. Control box of electric the spark generator (Based on [298, 299])

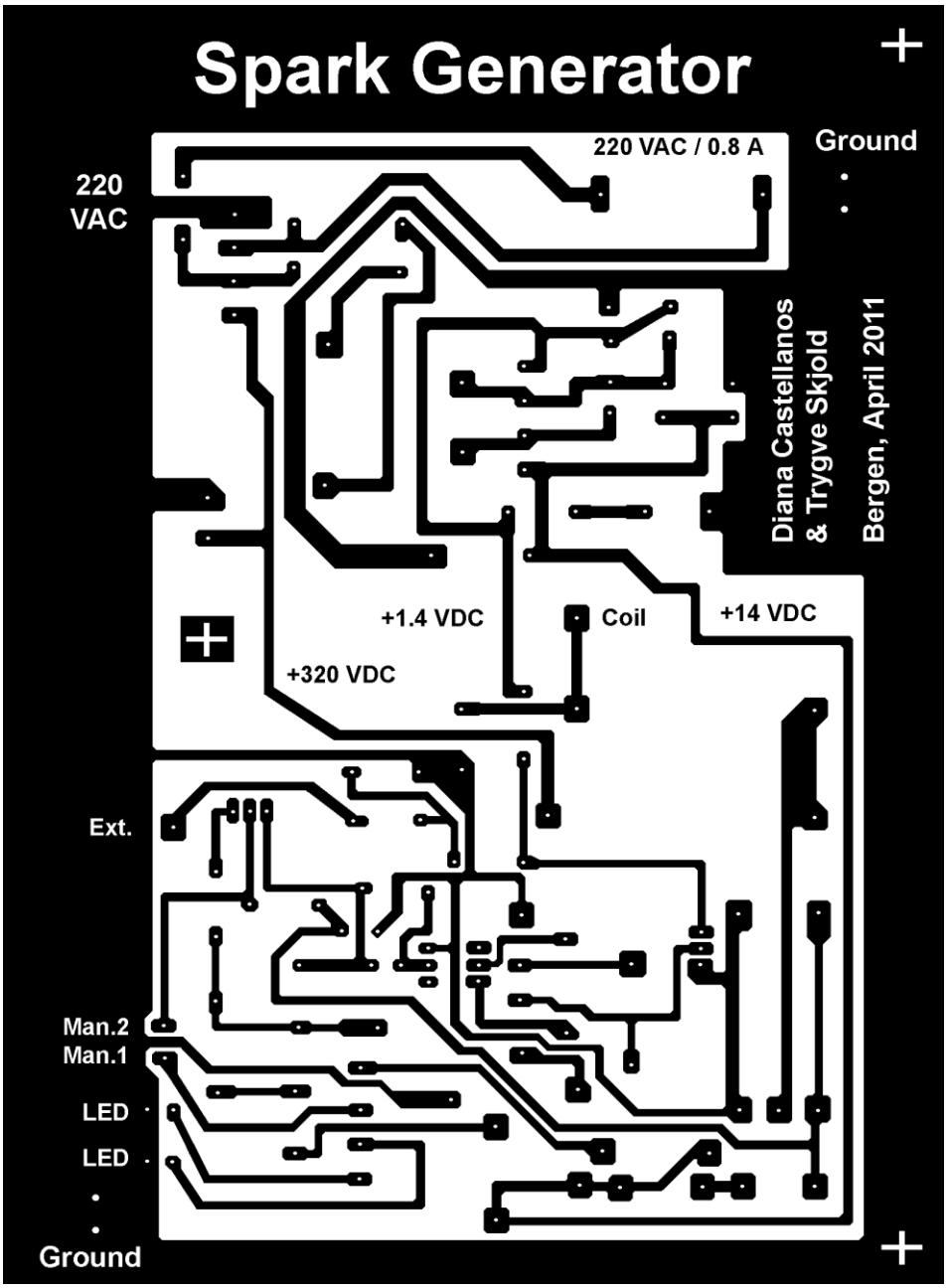

Figure C2. Electrical circuit board of the spark generator (Based on [298, 299]).

APPENDIX D

COMPONENTS OF 36 L DUST EXPLOSION EQUIPMENT

Table D1. Specifications of main components of the 36 L dust explosion equipment

Item	Name	Vendor - Part number	Specification
EV	Explosion vessel	Dow Chemical	36 L
FG1	Top flange	Texas Flange - Blind - 12.5 in	
FG2	Bottom flange	Texas Flange - Blind - 8.5 in	
R	Reservoir	Swagelok - 316L-HDF4-500	1 L
DC	Dust container	Stainless Steel cylinder	1 L
N	Rebound nozzle	KUHNER AG - Z000-310	
	Electrodes	KUHNER AG - Z000-132	
DPT	Dynamic transducer	PCB Piezotronics - CA102A04	0 - 1000 psi
SPT1	Pressure transducer	Omega- PX209-30V45G5V	-14.7 to 45 psi
SPT2	Reservoir pressure	Omega - PX309-500G5V	0 to 500 psi
SPT3	Reservoir pressure	Omega - PX309-500G5V	0 to 500 psi
SPT4	Static pressure transducer	SENSOTEC - 060-3147-01	
PI0	Analogue pressure gauge	Omega- PGC-20L-30V/30	30 inHg vac to 30 psi
PI2	Pressure indicator	Omega- PGC-20L-600	0 to 600 psi
PI3	Pressure transducer/indicator	HEISE - PM 40928	1500 psig

F	Filter	Swagelok - SS-8TF-60	
V1	Solenoid valve	Swagelok - SS-43GS6-31C	Normally closed
V2	Electrical valve	ASCO P/N: 8210G026	Normally closed
V3	Check valve	Swagelok - SS-58S12	
V4	Manual valve	Swagelok - SS-4558	
V5	Manual valve	Swagelok - SS-6JB	
V6	Solenoid valve	Swagelok - SS-45S8-33	Normally open
V7	Manual valve	Swagelok - SS-6P4T-M1	
V8	Manual valve	Swagelok - SS-42S4	
V9	Manual valve	Swagelok - SS-42S5	
V10	Manual valve	Swagelok - SS-42S6	
V10a	Bleeding valve	Swagelok - B554	
V11a	Manual valve	SS-6J8	
V11b	Manual valve	HOKE-2112F8Y	
V11c	Manual valve	HOKE-2112F8Y	
V12a	Manual valve	Swagelok-SS-4P4T-BK	
V12b	Manual valve	HOKE-2112F8Y	
V12b	Manual valve	HOKE-2112F8Y	
V12c	Manual valve	HOKE-2112F8Y	
V13a	Manual valve	VWR-Flowy	
V13b	Manual valve	HOKE-2112F8Y	
V13c	Manual valve	HOKE-2112F8Y	
V14a	Manual valve	ProStartPlatinum	
V14b	Manual valve	HOKE-2112F8Y	
V14c	Manual valve	HOKE-2112F8Y	
V15	Solenoid valve	Swagelok - SS-42GS4	Normally closed

V16	Bleeding valve	Swagelok - B-SS4-VH	
V17	Solenoid valve	Swagelok - SS-42GS4	Normally closed
V18	Manual valve	Swagelok - SS-42GS5	
PSV	Pressure relief valve	Swagelok	500 psig
RD	Rupture disk	FIKE	1000 psg
PR1	Pressure regulator	Swagelok - KCY1GPH412C90H10	O2-Air Max. 3600 psig
PR2	Pressure regulator	Victor Equip. Co. - NVTS-250D	O2-Air Max. 3000 psig
PR3	Pressure regulator	VWR-55850-277	Ar-He-N2 Max. 500 psig
PR4	Pressure regulator	ProStartPlatinum - PRS200233	Methane Max 3000 psig
P	Vacuum pump	DAYTON - 5K453C	1/2 HP-0.0017psi
DAQ	Data acquisition system	National Instruments-NI PCI-251E	1.25 MS/s
Canopy Hood	Enclosure box	Angle iron squeleton (1½ × 1/8 in). Lexan (1/4 in) and aluminun plates (1/8 in) panels	(w, l, h) 80 x 50 x 80 in
	Vacuum cleaner	Nilfisk Model GM-80 - 01790100	

APPENDIX E

ELECTRICAL SCHEMATIC FOR THE 36 L DUST EXPLOSION VESSEL

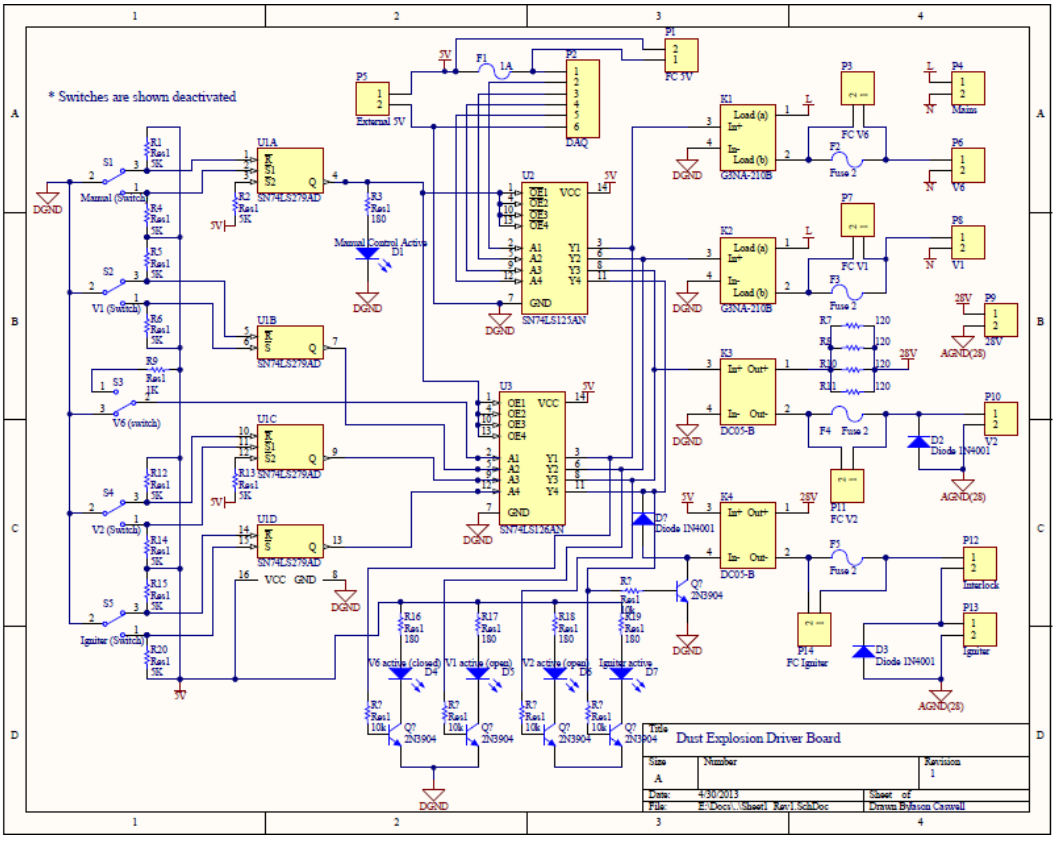

Figure E1. Electrical schematics of the 36 L dust explosion vessel

Dust explosion driver board designed by Chad Mashuga and built by Jason Caswell at Physics Department, Texas A&M University.

APPENDIX F

SIZING OF PRESSURE RELIEF SYSTEM

The relief sizing calculation is useful to determine the rate of material release through the pressure relief valve installed to protect the equipment in case of overpressure events. The following procedure was used [300]:

- **Mass flow calculation (Q_m):**

$$Q_m = C_o A P \sqrt{\frac{\gamma g_c M}{R_g T}\left(\frac{2}{\gamma+1}\right)^{\left(\frac{\gamma+1}{\gamma-1}\right)}}$$

$g_c(g\text{ravitation constant}) = 32.17 \frac{ft\ lb_m}{lb_f s^2}$

$M_{air}\ (m\text{olecular weight of air}) = 29 \frac{lb_m}{lb_{mol}}$

$\gamma_{air}\ (h\text{eat capacity ratio for the gas}) = \frac{C_p}{C_v} = 1.4$

T (absolute temperature of discharge) $=$ 536.4 R

$R_g(\text{ideal gas constant}) = 1545 \frac{ft\ lb_f}{lb_{mol}{}^\circ R}$

$A(\text{discharge area}) = \frac{\pi d^2}{4} = \frac{\pi(0.75in)^2}{4} = 0.442\ in^2$

$$B = \sqrt{\frac{\gamma g_c M}{R_g T}\left(\frac{2}{\gamma+1}\right)^{\left(\frac{\gamma+1}{\gamma-1}\right)}} = \sqrt{\frac{1.4\left(32.17 \frac{ft\ lb_m}{lb_f\ s^2}\right)\left(29 \frac{lb_m}{lb_{mol}}\right)}{1545 \frac{ft\ lb_f}{lb_{mol}{}^\circ R}\ \ 536.4\ \text{R}}} \times 0.335 = 0.023 \frac{lb_m}{lb_f\ s}$$

$$Q_m\ =\ C_o \times A \times P \times B$$

$C_o(\text{discharge coefficient}) = (0.06 - 1)$

$P(\text{maximum absolute relieving pressure}) = P_{max} + 14.7[=]\ psia$

$P_{max}(\text{for vessels exposed to fire}) = 1.2P_s$

$P_s(\text{set pressure})[=]\ psi$

Then, $$Q_m = C_o \times A \times B \times (1.2P_s)$$

- **Discharge time through the pressure relief valve (t):**

$$t = \frac{\rho_{air} \times V_{Vessel}}{Q_m} = \frac{\rho_{air} \times V_{Vessel}}{C_o \times A \times B \times (1.2P_s)}$$

$\rho_{air}(\text{air density}) = 1.2\frac{Kg}{m^3} = 0.075\frac{lb_m}{ft^3}$

$V_{Vessel}(\text{vessel volume}) = 36\ L = 0.7\ ft^3$

$$P_s = \frac{\rho_{air} \times V_{Vessel}}{C_o \times A \times B \times t}$$

$$P_s = \frac{0.075\frac{lb_m}{ft^3} \times 1.27\ ft^3}{C_o \times 0.442\ in^2 \times 0.023\frac{lb_m}{lb_f\ s} \times t}[=]\frac{lb_f}{in^2}[=]\ psi$$

$$P_s = \frac{0.075\frac{lb_m}{ft^3} \times 1.27\ ft^3}{C_o \times 0.442\ in^2 \times 0.023\frac{lb_m}{lb_f\ s} \times t} = \frac{9.37}{C_o \times t}$$

As shown in Figure F1, if the pressure relief valve is set at **500 psi**, the discharge time is lower than **0.5 seconds**. Higher rupture disc set pressure (P_s) represents a shorter discharge time until chock flow conditions are achieved.

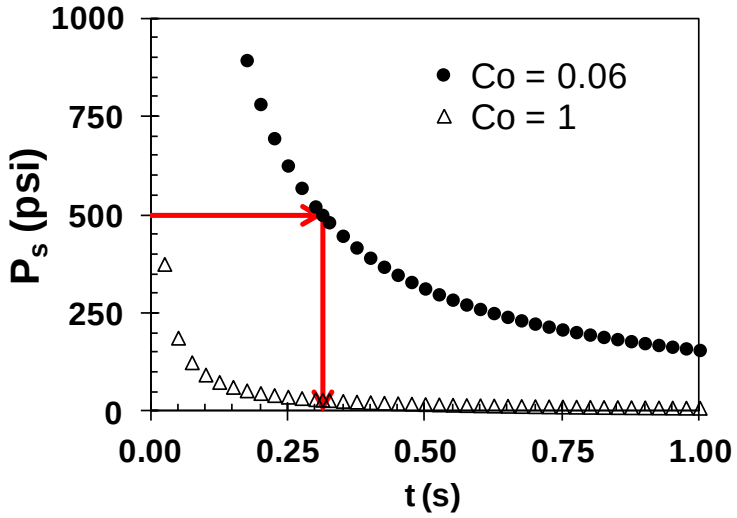

Figure F1. Discharge time obtained at different rupture disc set pressures

- **Chock flow conditions:**

Assuming that the vessel is pressurized from a tank containing air at 2000 psi ($P_o = 2000\ psi$), the maximum downstream pressure ($P_{chocked}$), resulting in maximum flow through the rupture disc is given by:

$$\boldsymbol{P_{chocked}} = P_o \left(\frac{2}{\gamma+1}\right)^{\left(\frac{\gamma}{\gamma-1}\right)} = (2000 + 14.7)\left(\frac{2}{2.4}\right)^{\left(\frac{1.4}{0.4}\right)} = 2014.7 \times 0.53$$

$$= \mathbf{1067}\ \boldsymbol{psia}$$

APPENDIX G

DETAILED EQUIPMENT OPERATION PROCEDURE

Table G1. Procedure to measure P_{max} and K_{St} values using the 36 L vessel

Step	Description
1.	Verify initial equipment lines and connections conditions
2.	Verify that instruments and test air pressure tanks are regulated to 120 and 350 psi, respectively.
3.	Check manual valves initial position: V4, V5, V10, V10, V10a, V14, V14a-c, V18 → close V7, V8, V9, V11a-c, V12, V12a-c →open
4.	Verify that vessel and reservoir pressure are equal to 1 atm
5.	Load sample into the dust container and install nozzle
6.	Install chemical igniters in the electrode rods of the top flange
7.	Close the vessel (screw top flange)
8.	* Initiate *Dust Explosion* code in Lab View program
9.	* At input data window: describe sample information and operation. Then, proceed to vacuum
10.	* At vacuum procedure window: Close V6, open V1 and pressurize air reservoir to 315 psia
11.	Turn on vacuum pump to reduce vessel pressure to 0.7 bara.
12.	Close V4 and then turn off the vacuum pump.
13.	Connect chemical igniters.
14.	Close V9 and V7 to protect pressure indicators in the vessel and vacuum line, respectively.
15.	* Proceed to "Test Dust"
16.	Close enclosure doors
17.	*On Test Dust window: click on initiate test
18.	*Check pressure profile and take notes of K_{St} and P_{max} values
19.	*Click on "Global Stop"
20.	*On "Dust Main" menu, click on "Global Stop"

* Steps to be performed in the computer

Table G2. Procedure to clean the 36 L vessel

Step	Description
1.	Open the canopy hood (it unable igniters activation)
2.	Unwire igniters on top of the vessel
3.	Open top flange (Place extraction line near vessel opening)
4.	Remove burned igniters and clean electrode rods.
5.	Release pressure on air reservoir. Open manually V2
6.	Vacuum clean the vessel
7.	Clean the dust storage container using air blasts from air reservoir
8.	Remove rebound nozzle and clean it
9.	Clean the dust storage container using vacuum cleaner
10.	Clean the filter on the vacuum pump line

APPENDIX H

PHYSICAL TERMINALS AND VIRTUAL CHANNELS IN LABVIEW

Table H2. Physical terminals and corresponding virtual channels used in LabView

Channel Number	Device	Description	Analog (+) terminal	Analog (-) terminal
ai0	AC Trigger	AC transformer	68	34
ai1	V2	Fast acting valve	33	66
ai2	IG	Igniter SSR	65	31
ai3	SPT4	Strain gauge transducer	30	63
ai4	SPT3	Static pressure transducer	28	61
ai5	DPT2	Dynamic pressure transducer	60	26
ai6	SPT2	Reservoir pressure transducer	25	58
ai7	SPT1	Vacuum pressure transducer	57	23

APPENDIX I

AIR DISPERSION SYSTEM CALIBRATION

No.	Pre-injection Pressure				Dispersion time	After injection	
	Reservoir (P_{ri})		Vessel (P_{vi})		t_{FAV}	Reservoir (P_{vf})	
	(bara)	(psia)	(bara)	(psia)	(ms)	(bara)	(psia)
1	15.2	221.0	0.5	7.6	400	1.0	14.7
2	15.2	221.0	0.5	7.6	300	1.0	14.7
3	15.2	221.0	0.5	8.1	200	1.0	14.7
4	15.2	221.0	0.7	10.0	100	1.0	14.7
5	15.2	221.0	0.8	11.5	75	1.0	14.7
6	18.2	264.0	0.4	6.0	400	1.0	14.7
7	18.2	264.0	0.4	6.0	300	1.0	14.7
8	18.2	264.0	0.5	7.5	200	1.0	14.7
9	18.2	264.0	0.6	9.5	100	1.0	14.7
10	18.2	264.0	0.7	11.0	75	1.0	14.7
11	21.7	314.7	0.3	4.0	300	1.0	14.7
12	21.7	314.7	0.6	8.8	100	1.0	14.7
13	21.7	314.7	0.7	10.3	75	1.0	14.7
14	21.7	314.7	0.5	10.3	50	1.0	14.7

APPENDIX J

REPEATABILITY ANALYSIS USING NIACIN DUST

Dust explosions conducted with niacin dust at a nominal dust concentration of 500g/m^3 using two chemical igniters of 5 kJ as ignition source.

Table J1. Dust explosion tests conducted using niacin dust from calibration Round Robin 2001

Test No.	t_{FAV} **(ms)**	$p_{r,i}$ **(barg)**	$p_{r,f}$ **(barg)**	$p_{v,i}$ **(bara)**	$p_{v,f}$ **(bara)**	p_{ip} **(barg)**	t_{ip} **(ms)**	t_m **(ms)**	P_{ex} **(barg)**	P_m **(barg)**	$(dP/dt)_{max}$ **(bar/s)**	K_{St} **(bar-m/s)**
1008231258.36L	75.10	20.75	9.83	0.71	1.01	4.35	19.75	32.70	8.0	8.5	729	241
1204111520.36L	75.20	20.63	10.25	0.71	1.00	4.28	20.30	33.80	8.0	8.4	730	241
1204181525.36L	75.00	20.72	11.31	0.67	0.93	4.10	19.70	31.60	7.6	7.9	694	229
1204181527.36L	75.20	20.70	10.31	0.69	0.98	4.24	17.50	28.00	7.9	8.4	767	253
1204181529.36L	74.80	20.70	10.16	0.70	0.99	4.22	19.50	35.20	7.8	8.2	646	213

1204191530.36L	74.80	20.69	10.43	0.72	1.01	4.46	20.50	31.60	8.1	8.6	747	246
1204191531.36L	75.00	20.70	10.43	0.70	0.99	4.20	17.90	28.80	7.8	8.3	737	243
1204191532.36L	75.20	20.67	10.46	0.69	0.97	4.22	19.30	30.00	7.7	8.2	716	236
1204191533.36L	74.80	20.72	10.37	0.70	0.99	4.53	18.70	28.40	7.8	8.2	719	237
1204191534.36L	75.00	20.68	10.51	0.67	0.96	4.28	25.30	35.80	7.7	8.1	671	222
1204191535.36L	75.00	20.67	10.40	0.68	0.96	4.33	18.30	29.80	7.9	8.3	759	250
1204191536.36L	75.00	20.70	10.51	0.69	0.98	4.12	17.70	27.00	7.7	8.1	753	248
$\bar{x} = \frac{1}{k}\sum_{i=1}^{k} x_i$	75.0	20.7	10.4	0.7	1.0	4.3	19.5	31.1	7.8	8.3	722	238
$StDev = \sqrt{\frac{\sum_{i=1}^{k}(x_i - \bar{x})^2}{k-1}}$	0.2	0.0	0.3	0.0	0.0	0.1	2.1	2.9	0.2	0.2	36	12

where, ($\bar{x}$), StDev and *k* correspond to the mean value, standard deviation and total number of tests.